Low-Cost Beam Steerable Antennas Using Parasitic Elements

Reza Movahedinia

A Thesis
In the Department
of
Electrical and Computer Engineering

Presented in Partial Fulfillment of the Requirements
For the Degree of
Doctor of Philosophy (Electrical and Computer Engineering) at
Concordia University
Montreal, Quebec, Canada

August 2018

Concordia University
School of Graduate Studies

This is to certify that the thesis prepared

By: **Reza Movahedinia**

Entitled: **Low-Cost Beam Steerable Antennas Using Parasitic Elements**

and submitted in partial fulfillment of the requirements for the degree of

Doctor of Philosophy (Electrical & Computer Engineering)

complies with the regulations of the University and meets the accepted standards with respect to originality and quality.

Signed by the final examining commitee:

____________________ Chair
Dr. Andrea Schiffauerova

____________________ External Examiner
Dr. Jean-Jacques Laurin

____________________ External to Program
Dr. Marco Bertola

____________________ Examiner
Dr. Ahmed A. Kishk

____________________ Examiner
Dr. Robert Paknys

____________________ Thesis Co-Supervisor
Dr. Abdel Sebak

____________________ Thesis Co-Supervisor
Dr. Reza Chaharmir

Approved by ____________________
Dr. Mustafa K. Mehmet Ali, Graduate Program Director

Friday, November 2, 2018 ____________________
Dr. Amir Asif, Dean
Gina Cody School of Engineering and Computer Science

Abstract

Low-Cost Beam Steerable Antennas Using Parasitic Elements

Reza Movahedinia, Ph.D.

Concordia University, 2018

Beam steerable antennas are considered as a possible solution for meeting challenges in military and civilian systems such as satellite communication networks, automotive collision avoidance radar, base stations and biomedical applications. Phased array antennas are a natural choice as the foundation for many steerable antenna platform due to its flexibility and gain scalability. The implementation of a phased array requires a large number of electronic components, tending to drive the cost of phased arrays and limit their usage to military applications. The electrically steerable parasitic array radiator (ESPAR) has been introduced as an antenna which is capable of adaptively controlling its beam pattern using parasitic elements loaded with varactors. ESPAR has attracted the attention of researchers from the desire for electrically scanned beams with inexpensive fabrication and has found as a suitable candidate for communication systems applications, including advanced radars, cellular base stations and space communications.

The ultimate goal of this research is to design and propose state of the art designs in the field of ESPAR that can satisfy the requirements of today's advanced communication systems, which should be cost-effective and can compete with other rival technologies. Considering the potentials of ESPAR, it can be proved that it is a good candidate for modern wireless communications. The thesis presents several contributions related to the design and analysis of ESPAR technology using dielectric resonator antenna (DRA) as the main radiator element. First, the thesis presents solutions to alleviate the problems associated in implementing a large ESPAR. The large array is useful in many applications since some required reconfigurable radiation characteristics may not be achievable with a single ESPAR element. The proposed structure consists of 240 perforated DRAs, which

are uniformly excited by a parallel-series feeding network. By employing the perforation technique, the need for aligning and bonding individual DRA is eliminated. The subarrays are placed in an interleaved arrangement to suppress the grating lobes. The proposed large ESPAR can incredibly reduce the number of phase shifter by 80% in comparison with the conventional phased array, which makes it inexpensive.

Second, the thesis investigates potentials of ESPAR for massive multi-input multiple-output (MIMO) communication. Massive MIMO technology has attracted tremendous interest due to its capabilities in enhancing the data transmission capacity, increasing the reliability, and reducing the multipath fading. However, in this technology for feeding each individual antenna, one radio frequency chain is required that can increase the power consumption and complexity of the structure. Moreover, to obtain decorrelated channels and to reduce mutual coupling, the antenna should be spaced sufficiently far from each other that imposes increased physical dimensions. In contrast to the conventional MIMO structures, in ESPAR only one RF chain is needed and the small size constraint turns to be an advantage as the mutual coupling is exploited to form the desired signals. Furthermore, by controlling the tunable loads at each parasitic antenna element, different radiation patterns can be formed which can significantly improve the performance of a MIMO antenna system operating in a changing environment. Thus, by using the advantages of ESPAR, a design approach to address the size and cost issues is proposed through this work. The proposed design is validated by simulation and measurement of a prototype, and results include the antenna and MIMO figure of merits such as radiation patterns, efficiency, S-parameters, signal correlations, total active reflection coefficient (TARC), and channel capacity. These results have demonstrated that the proposed ESPAR design can be successfully implemented for a massive MIMO structure.

Finally, the thesis presents an effective method to design a ESPAR with a circularly polarized (CP) beam-scanning feature. Circular polarization is an ideal polarization due to its advantages in signal propagation properties, which can address the difficulties associated with mobility, inclement weather conditions, and immunity to multi path distortion. In this work, the CP beam steering is achieved by adopting a sequential rotation approach for placing the parasitic antennas that are loaded with tunable varactors. The proposed

CP-ESPAR technique eliminates the need of expensive phase shifters, which significantly reduces cost and fabrication complexity. For performance evaluation, a prototype of the proposed antenna is designed, fabricated, and measured. It is observed that the proposed antenna has a monotonic CP beam scanning from – 22° to 22° operating at 10.5 GHz.

Acknowledgments

My most sincere thanks go to my supervisors Dr. Abdel R. Sebak and Dr. Reza Chaharmir for their continuous support, patience and insightful guidance during different stages of my Ph.D studies and writing of this thesis.

I would like to express my gratitude to my committee members for their precious time evaluating this thesis.

I wish to thank my friends and colleagues at Concordia University: Mohammad Ranjbar Nikkhah, Hamed Abdzadeh, Mohammad Hasheminasab, Touraj Laleh, Elham Baghernia, Tahseen Mustafa, Vincent Mooney-Chopin, Hossein Kourkchi, Omid Taagholi and Sina Saberi for their limitless support during the compilation of this work.

Finally, I would like to express my eternal appreciation to my family for their everlasting support and love. My special thanks go to my wife Maryam without whose help and support this thesis could have not come into existence.

To my loving wife, Maryam!

Contents

List of Figures

List of Tables

List of Abbreviations

ESPAR	Electrically Steerable Parasitic Array Radiator
2D	Two Dimensional
3D	Three Dimensional
AUT	Antenna Under Test
DRA	Dielectric Resonator Antenna
CST MWS	Computer Simulation Technology Microwave Studio
HFSS	High Frequency Structure Simulator
MIMO	Multiple-Input and Multiple-Output
DOA	Direction of Arrival
AOA	Angle of Arrival
CP	Circularly Polarized
AR	Axial Ratio
T/R	Transmit/receive
RF	Radio Frequency
SPA	Switched Parasitic Array
TARC	Total Active Reflection Coefficient

Chapter 1

Introduction

1.1 Introduction

Many communications systems make use of directional antennas such as satellite communication systems, radars, cellular base stations and wireless local area networks. However, a major downside for having a directive antenna is that the antenna should properly oriented to point in the direction of arrival (DOA). It means that if the incoming signal is arriving in another part of space rather than that covered by the antenna, it cannot be received. Utilizing omnidirectional antennas in a wireless link might seem the solution to this problem, as they have a uniform gain in all directions. However, the omnidirectional antenna has low gain and can only receive limited power signals.

One way to face with these issues is that the antenna can dynamically steer its main directive beam to always point at the DOA of the strongest signal. Therefore, it could potentially increase the probability of obtaining a respectable level of receiving SNR. These antennas are referred to as "beam steerable antennas." The very first approach for beam steerable antennas involves mechanically turning a directive antenna to face the direction of interest. However, mechanical steering becomes undesirable and difficult when we consider factors such as antenna size, weight, fast beam scanning, and weather conditions. In addition, it also is prone to mechanical failure due to fatigue and wearing of moving

‘

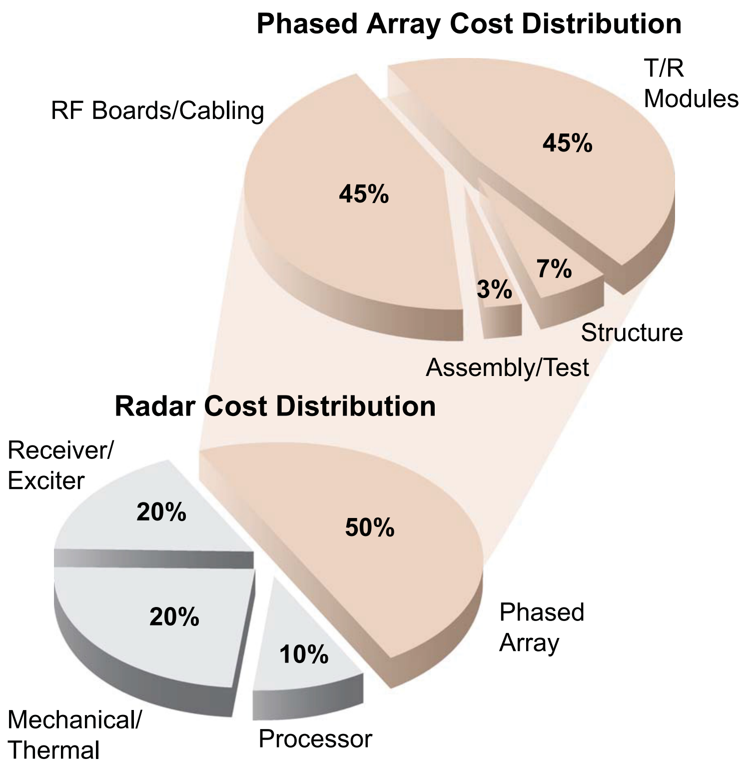

Figure 1: Typical cost distribution for phased array radar as in [1] ©2016 IEEE.

parts. The other approach to obtain a beam steerable antenna, is phased array antennas that consist of a number of antenna elements that can electronically steer its main beam to a point in different directions, without moving the antennas. In a phased array, each element is equipped with a phase shifter that is controlled by a computer system that can provide the required phase shift for beam scanning in the desired direction. Phased array has significant operational advantages such as spatial filtering, gain boosting in transmitting and sensitivity improvement in receiving signals. However, the implementation of a phased array requires a large number of electronic components that drive the cost of phased arrays and limit their usage to military applications. Fig. 1 shows a typical cost distribution for a military phased array radar. As observed, the phased array occupies half of the total cost of the system. In the phased array portion of the radar, there are two major parts that represent 90% of its cost: Transmit/receive (T/R) modules Module and radio frequency (RF) boards/cabling. The T/R module consists of RF phase shifters and amplitude controllers, amplifier chains, RF switches, and other microwave components. Therefore, a reduction in number or these components is of the greatest importance and can significantly reduce the cost of phased array. It should be noted that the other important shortcoming of phased arrays is the complexity of their feeding network because each element in array need to be actively fed by an RF signal. These aforementioned issues become more severe when we consider the losses of the feeding network at high frequencies. These issues must be adequately addressed to widen the use of phased array technology in modern communication system.

1.2 Motivation

The Electrically Steerable Parasitic Array Radiator (ESPAR) has been introduced as an array antenna which is capable of adaptively controlling its beam pattern using parasitic elements loaded with varactors. ESPAR has attracted the attention of researchers from the desire for electrically scanned beams with inexpensive fabrication and has been found as a good candidate for radar and communication systems applications, including advanced radar systems, cellular base stations and space communications. The ESPAR consists of one driven radiator coupled to the nearby parasitic radiators. Therefore, parasitic elements can obtain their energies from a driven radiator through mutual coupling. The necessary phase shift for beam scanning in the desired direction is created by placing tunable reactive loads such as varactors at the terminals of the parasitic radiator. The value of the varactors can vary with the biasing voltage, giving the antenna a vast tuning ability to achieve inexpensive beam steering. However, with all the above capabilities, there are some functional restraints associated with the ESPAR technique. The desired beam scanning with varactors should not be achieved at the expense of directivity or efficiency. The operation frequency must be maintained for different beam scanning directions as well the low side lobe level. Moreover, there is a possibility of adverse effects because of excitation of undesired mode at the operation frequency which must be prohibited. Lastly, great care must be taken of the magnitude of parasitic current by optimizing the spacing between adjacent elements since it will affect the aperture efficiency. To sum up, it is believed that the ESPAR could become a promising approach for reducing the cost of a scanning antenna array.

1.3 Objective

The investigation and development of the ESPAR technology is the focus of this thesis. The goal of the thesis is to expand the state-of-the-art in the area of ESPAR, and to reveal the hidden potential of parasitic antenna arrays for wireless communication systems. Specifically, for this thesis, the investigation aims to make contributions in three areas:

(1) Realization of Large ESPAR.

In the first stage, we attempt to highlight those practical issues that are critical in implementing a large ESPAR. The large array is useful in many applications since some required reconfigurable radiation characteristics may not be achievable with a single ESPAR element. The crucial issues related to large ESPAR have been addressed in this stage, including the design of a feeding network, difficulties in aligning and bonding the individual elements of the DRA and the grating lobe problem.

(2) Large ESPAR for Massive MIMO Systems.

The second stage's focus is on the employment of ESPAR to make it suitable for MIMO communication systems. The ESPAR can successfully meet the criteria of MIMO application requirements such as small size and low-cost requirements since it allows for closely spaced radiating elements and requires only a single RF chain to drive the single active antenna of the array. Moreover, due to high beamforming capabilities of ESPAR, it can be considered for multiplexing and MIMO systems.

(3) Circularly Polarized ESPAR.

The circularly polarized (CP) beamforming capability using parasitic elements is investigated in the third stage of this research. Circularly polarized antennas are ideal for many applications in modern wireless communications since they have advantages of eliminating the difficulties associated with mobility, inclement weather conditions, immunity to multipath distortion, polarization mismatch losses and non-line-of- sight applications. The design of a CP ESPAR with continuous beam scanning ability is very challenging, and there is little work in the reported literature on the beam control of a circularly polarized wave.

1.4 Organization of the Thesis

The structure of the thesis is as follows. Chapter 2 presents a literature review and an introduction to the parasitic reconfigurable antenna designs. The reconfigurable techniques such as switched parasitic array, ESPAR and parasitic pixel surface are discussed. Furthermore, the advantages and disadvantages of each technique are also presented.

The theoretical background and methodology required for designing the parasitic array radiators are presented in Chapter 3. It describes the mutual coupling phenomenon which is the most fundamental concept to define the nature of ESPARs. An introduction to the methodology for designing the ESPAR antenna and finding the proper reactive loads for desired directions is also presented. In addition, two common shapes of DRA and their coupling methods are discussed briefly. Finally, an overview of the simulation software packages and the numerical techniques they adopt is presented.

Chapter 4 discusses solutions to alleviate the practical problems that are critical in implementing a large ESPAR. These problems include the design of a feeding network for a large ESPAR, difficulties in aligning and bonding the individual elements of the DRA and grating lobe issue. Using the methods introduced in this chapter can help ESPAR antenna implementation in large arrays with improved performance. To best explore the differences and advantages of our approach, the proposed ESPAR is compared to a conventional phased array antenna and steerable reflectarray (RA). Experimental results for the prototype of the large ESPAR for broadside are also presented.

Chapter 5 investigates the performance of the DRA-ESPAR in MIMO and massive MIMO systems. To this end, we have proposed a 4-port MIMO configuration that the mutual coupling of its adjacent ports are reduced by orthogonal placement of subarrays. This structure is well examined in terms of MIMO figure of merits such as isolation, correlation, mean effective gain and branch power ratio. The performance of the proposed DR-ESPAR is also studied in a massive MIMO configuration which is realized by extending the elements of the proposed MIMO structure. Finally, this study has been accomplished by fabricating and measuring a prototype of the 4-port MIMO configuration.

In Chapter 6, an effective method to design an ESPAR with a circularly polarized (CP) beam-scanning feature is presented. The idea of using a sequential rotation technique in placing the parasitic elements is discussed and experimental results are presented. A brief overview of polarization followed by DRA designs for achieving circular polarization are also outlined. Finally, in Chapter 7, major conclusions of the thesis are summarized and the future contributions into the use of ESPAR for antenna applications are addressed.

Chapter 2

Literature Review

2.1 Introduction

In this chapter, a review of parasitic reconfigurable antenna designs is presented. It begins with the introduction of the primary parasitic arrays such as Yagi-Uda antenna. Then the other reconfigurable techniques such as switched parasitic array, ESPAR and parasitic pixel surface are discussed. Furthermore, the advantages and disadvantages of each technique are reviewed.

2.2 The Emerge of Switched Parasitic Arrays

Mutual coupling has been traditionally considered as a curse in antenna array mainly due to the fact that it can severely affect the antenna radiation properties. Furthermore, mutual coupling is difficult to predict analytically, and it complicates the antenna analysis and design. However, in the history of antenna development, there are some cases that mutual coupling has been used as a design tool to meet certain antenna requirements. The most famous example is the Yagi-Uda antenna which named after the inventors Prof. S.Uda and Prof. H.Yagi in 1926 [3]. the Yagi-Uda antenna, as shown in Fig. 2, consists of one driven element that is connected to the transmitter or receiver with a transmission line

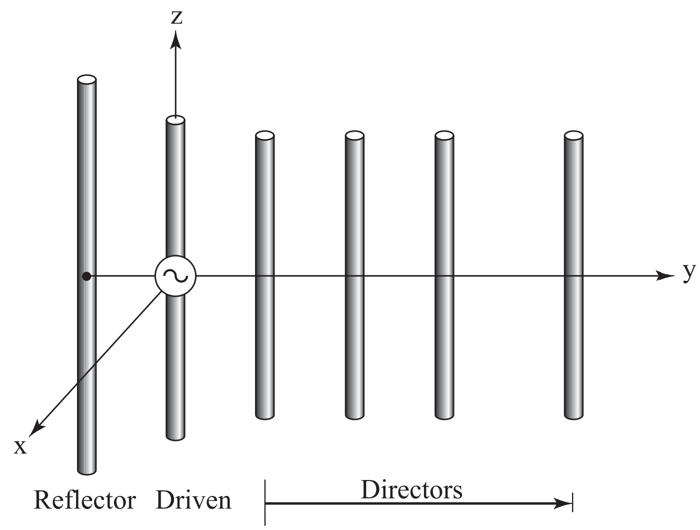

Figure 2: Yagi-Uda antenna configuration.

and parasitic elements that are placed parallel and close to the driven antenna. Parasitic elements have no transmission line connection to the transmitter or receiver and can obtain their energy from the driven antenna through the mutual coupling. These elements can be sorted according to their size compared to the driven antenna into two types of director and reflectors. Directors are the parasitic elements that are slightly shorter than the driven antenna, placed in front of the driven antenna. The reflectors placed at the back of driven element and their lengths are slightly longer than that of driven element. By proper adjustment of the inter-element spacing between the elements, a highly directional beam can be formed toward the directors, and almost none behind the reflector. The properties of the director and reflector, have been widely used to create simple smart antennas, referred to as “switched parasitic arrays” (SPAs). In these antennas, a simple switching mechanism is used that can alter the electrical length of the parasitic elements, resulting in classical “reflector” or “director” behavior that leads to steered or tilted beams.

The first occurance of this idea was reported in a patent by Gueguen in 1974 where several Yagi-Uda dipole arrays shared an active element [4]. By placing a diode at the center of each reflector, the electrical length can be controlled. Therefore, when the diode is on, the parasitic element resonates, and allows radiation scattering. In contrast, when

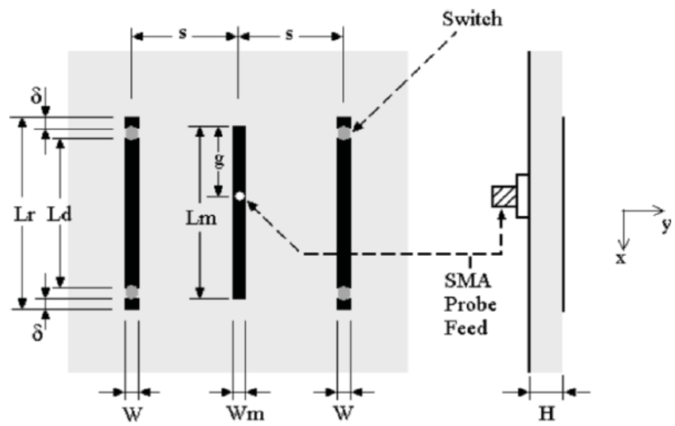

(a)

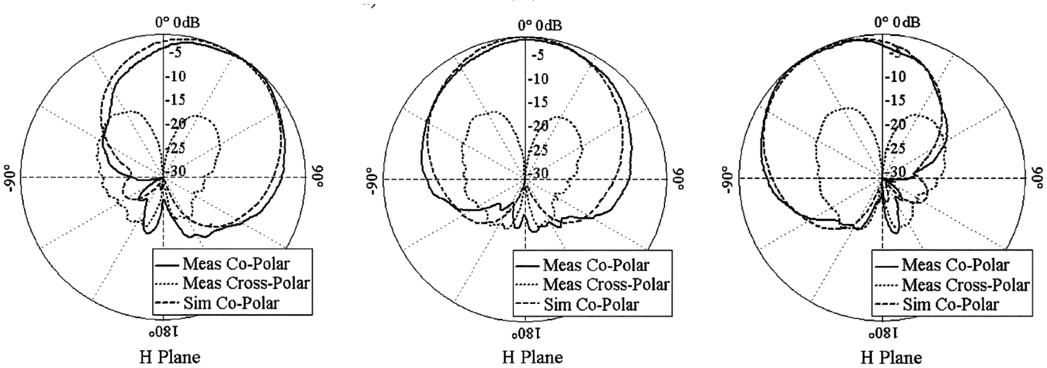

(b) (c) (d)

Figure 3: Physical structure and radiation properties of the reconfigurable microstrip parasitic array. (a) Physical structure. (b) reflector director (RD) beam pattern. (c) director-director (DD) beam pattern. (d) director-reflector (DR) beam pattern. (Zhang et al. [2], ©IEEE 2004.)

the diode is off, it leaves the dipole non-resonant and lets radiation pass. This idea has been widely extended in different wire and microstrip-based reconfigurable antenna structures [2, 5–11]. One example is that presented by Zhang et al. [2] as shown in Fig. 2. The antenna consists of a probe-fed center strip with parasitic strips on both sides which are printed on a dielectric substrate. At the center of each parasitic strips a switch is placed. Therefore, the parasitic strips can be lengthened or shortened with respect to the center strip by simply open-circuiting and close-circuiting the parasitic elements' switch. The lengthened left parasitic element works as a reflector (R) and the shortened right parasitic element works as a director (D). This antenna has three different radiation

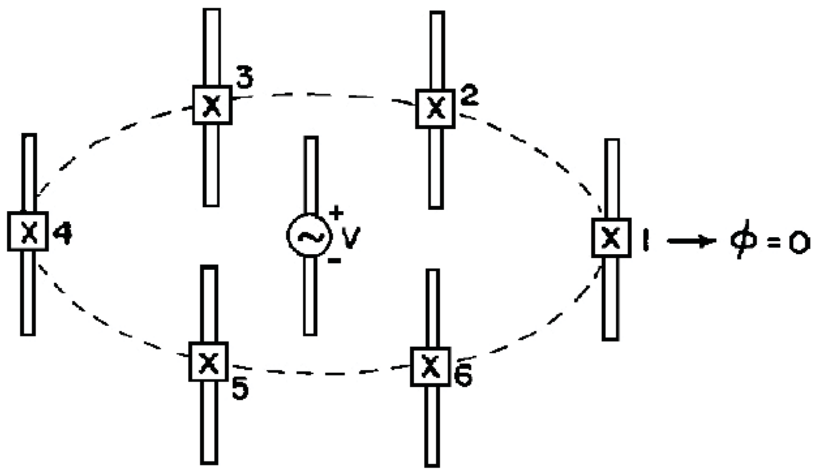

Figure 4: A seven-element circular array of reactively loaded parasitic dipoles for reconfigurable beam steering and beamforming (R. F. Harrington [12], ©IEEE 1975)

pattern states (RD, DR and DD) as shown in Fig. 2(b), (c), and (d). SPAs were a significant finding in the antenna design field due to their advantages such as low cost and simple structure. Many commercial wireless communication systems used SPAs in their wireless devices (e.g., Ericsson, HTC smartphones). Despite of these advantages, there is one main problem associated with SPAs. The scan resolution in SPAs is low due to the binary nature of switches, so the number of beam scanning direction is limited to finite discrete numbers. Thus, it does not fit the requirement for some processing algorithms that need infinite combinations of signals at the ports of the array elements (e.g. space-time processing algorithm).

2.3 Electrically Steerable Parasitic Array Radiator (ESPAR)

In 1975, Harrington presented a theory that suggested the radiation characteristics of an N-port antenna system can be controlled by impedance loading the ports and feeding only one or several of the ports [12]. In fact, he extended the idea of SPAs by replacing the switching states of diode with a wide range of tunable reactive loads that can be as simple

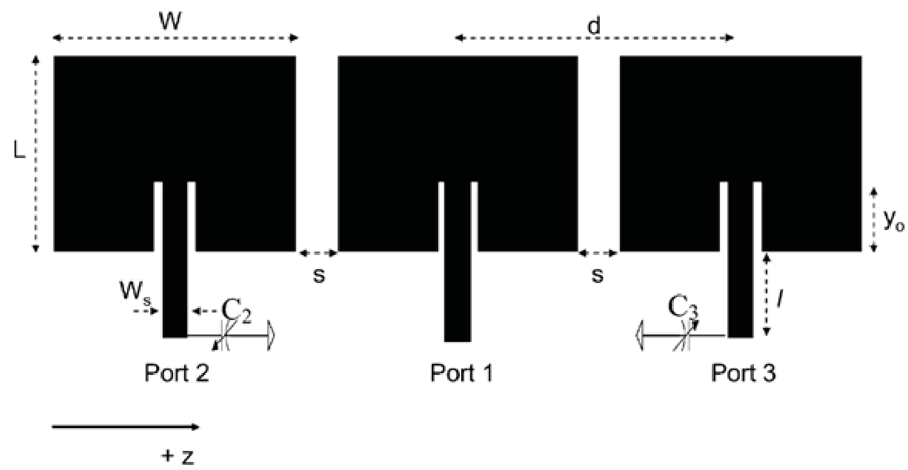

Figure 5: Geometry of a three-element ESPAR patch antenna phased array (Yusuf et al. [13], ©IEEE 2008)

as a single varactor. Therefore, the form of currents induced on the parasitic elements is different for each set of reactive loads, leading to more accurate control of the antenna radiation characteristics. As an example of the numerical analysis, he used a reactively loaded array as shown in Fig. 4 which consists of six reactively loaded dipoles at an equal angular separation and a centered driven dipole. The reactive loads can control the phases of the parasitic element currents in order to have an azimuthal beam scanning in a certain direction. However, there is a large back-lobe due to lack of ground plane and the elevation scanning is not possible with this array. This basic idea was revised by Gyoda's group in 2000 [14]. They reduced the profile of the Harrington's array by replacing the dipole antenna with the monopole antenna above a ground plane. They termed this design as "Electronically Steerable Passive Array Radiator," or ESPAR. In [3] by embedding the ESPAR antenna array in a homogeneous dielectric material, an overall volume reduction of 80% and footprint reduction of 50% were achieved [15].

Due to the introduction of N-port network theory for any types of element in [12], the ESPAR research significantly increased afterward with different type of antennas and it has been an active area of research especially for the past 15 years. Among the different antenna element candidate for ESPAR, the microstrip patch antenna has attracted many

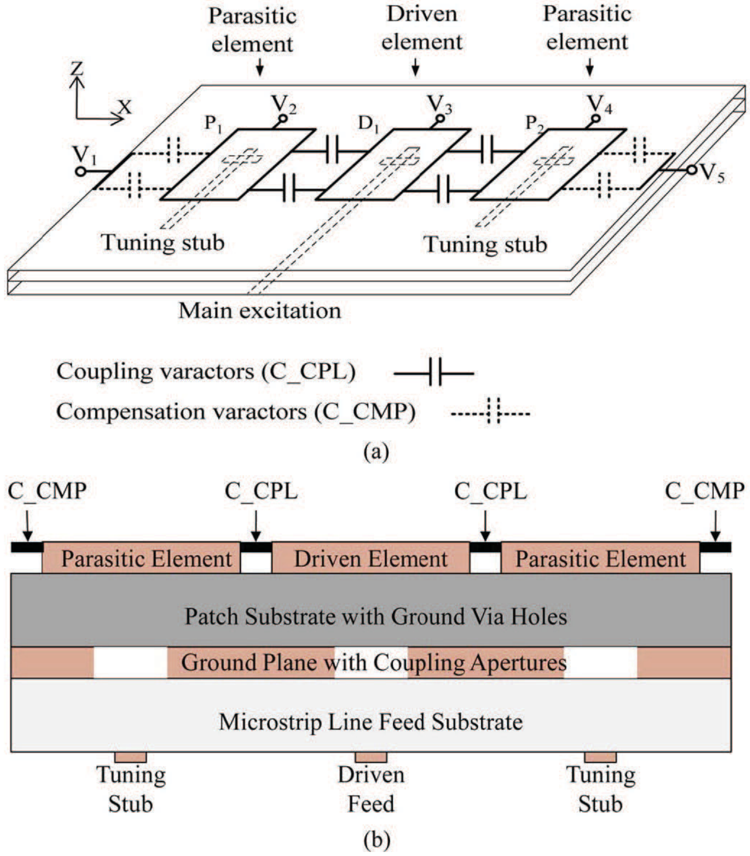

Figure 6: Geometry of the proposed configuration for a patch ESPAR (a) schematic. (b) stacked layer view. as (Luther et al. [16], ©IEEE 2012)

researchers' interest due to their low profile and their simple PCB fabrication process. The development of the microstrip-antenna as an ESPAR element was first presented by Yousef in 2008 [13]. The proposed ESPAR as shown in Fig. 5 consists of one driven patch antenna, coupled in its H-plane to two other parasitic patch antennas. The beam steering angles from 20 to -20 degrees was achieved by changing the reactive loads of the parasitic antenna without using multiple passive radiators. However, at some scanning beam the side-lobes increase considerably due to the low level of current magnitude induced on the parasitic patch. The next attempt considered the parasitic coupled patches in both E and H Planes [17] which successfully demonstrated a steering radiation pattern with 30 degrees of tunability. In this paper more attention was paid to the signal-to-noise ratio; but still the return loss was much neglected. Furthermore, the mutual coupling was not

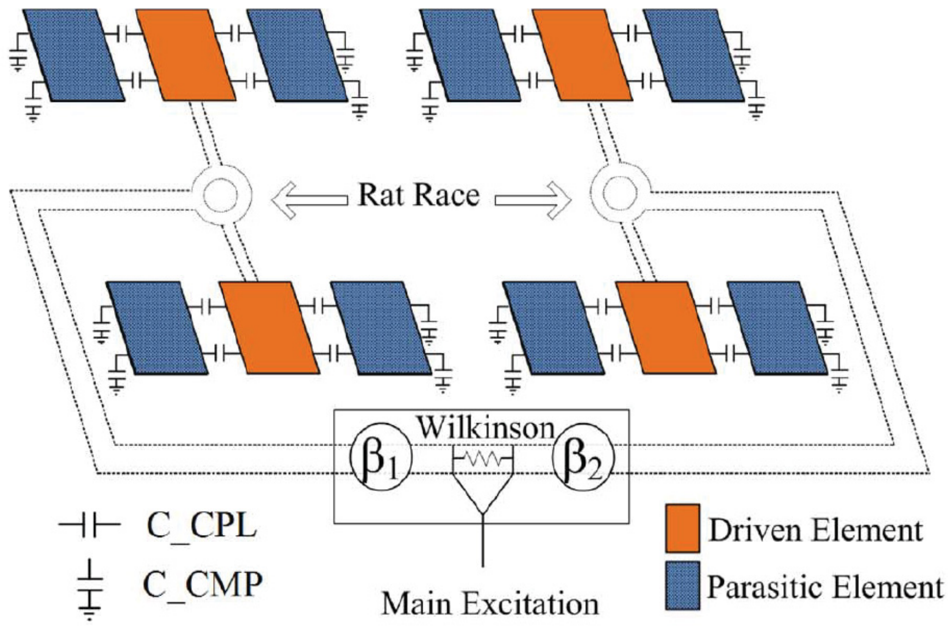

Figure 7: Geometry of the proposed configuration for a patch ESPAR (a) schematic. (b) stacked layer view. as (Luther et al. [16], ©IEEE 2012)

controlled, and the resulting radiation patterns were generally broad with low gain. These aforementioned shortcomings are further improved in the technology introduced in [16]. The configuration is shown in Fig. 7 where coupling capacitors were placed between the three driven and parasitic patches. In addition, compensation varactors, were placed on the parasitic patches to preserve resonance at the operating frequency. The parasitic ports were left open circuit and the lengths of which are optimized to improve the radiation characteristics. A continuous electronic scanning from -15° to 15° was achieved while the impedance matching maintained with the peak gain of 7.4 dBi. The DC biasing was achieved by using RF ground stubs on the feed layer, which provided simultaneously RF grounding and independent DC voltage for the varactors, while introducing design complexity and increasing cost. However, this multi-layered configuration complicates the fabrication process which increases the probability of misalignment. Furthermore, some applications such as on wafer arrays does not support multi-layered structures. These

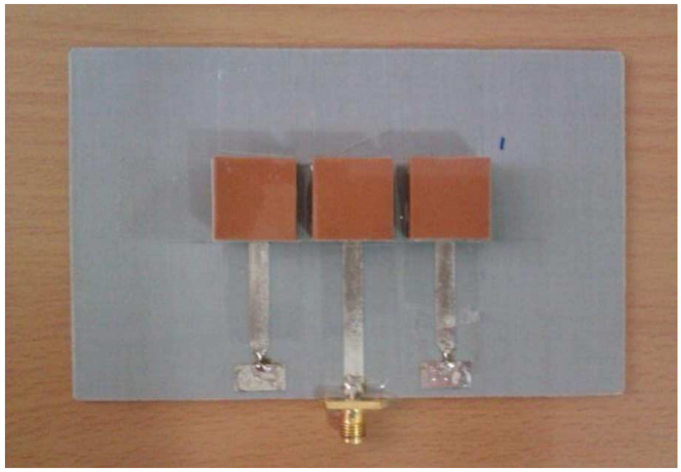

(a)

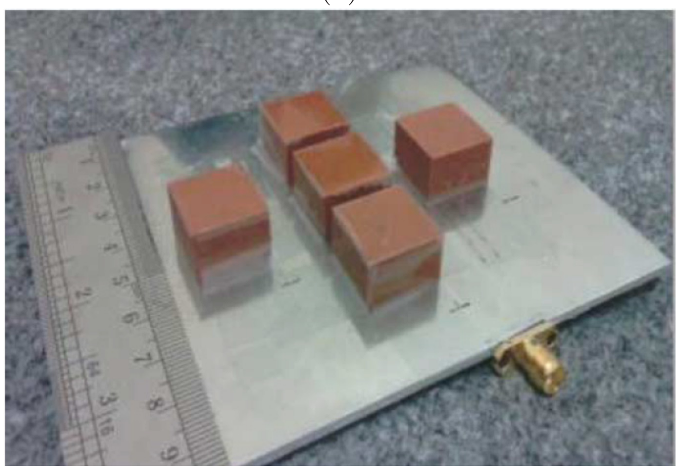

(b)

Figure 8: Geometries of different ESPAR configuration using DRA as the main element (a) Three elements subarray (Ranjbar et al. [19], ©IEEE 2013) (b) Five elements subarray (Ranjbar et al. [20], ©IEEE 2014)

shortcomings were improved by the same authors, using the single-layer microstrip ESPAR [18]. By employing a Y-groove cut on the ground plane the sufficient independent DC nodes to uniquely control varactors was achieved. This enhancement simplified the structure and negated the need for a floating RF grounds which was previously used.

Integration of a three-element microstrip subarray in a small ESPAR array has been presented in [18]. This array consists of 4-subarrays with a total of 12 radiating aperture coupled microstrip antenna elements. In this research ESPAR was compared with traditional phased array antenna, showing that ESPAR can reduce the number of used phase shifters, lowering the total cost of fabrication. In addition, comparing with a thinned phased array antenna, ESPAR has better gain and side lobe level. However, the scanning is limited to the H-plane.

In comparison with microstrip patch antennas, dielectric resonator antennas (DRA) have several interesting advantages such as small size, high radiation efficiency, wider impedance bandwidth, low loss and no surface wave excitation [21]. A subarray of the H-plane DRA-ESPAR mounted on a dielectric substrate and directly excited by microstrip lines has been reported in [19] as shown in Fig. 8(a). It shows scanning capabilities of +30° to -30° while it is matched for all the beam scanning directions. This research confirmed that DRA could be an attractive alternative to the traditional ESPAR dipole and microstrip patch elements. This research is further improved by the same authors in [20] as shown in Fig. 8(b). The proposed subarray consists of a 4-crossed element which parasitically coupled to the centered-driven DRA. This arrangement enables the ESPAR to scan the beam in both the E- and H-planes.

2.4 Parasitic Pixel Surface

Another approach based on parasitic coupling was recently introduced as a promising reconfigurable technique [22–31] referred to as pixel antenna. By dividing the aperture into small pixels that can be interconnected by RF switches, beam pattern can be adaptively controlled. Pixel antennas have been demonstrated in different architectures which are shown in Fig. 9.

The basic architecture for a parasitic pixel antenna was first presented by Pringle et al. in 2004 [22], based on their previous studies in Georgia Tech Research Institute (GTRI) [33–36]. The proposed antenna consists of a thin dielectric substrate that supports an array of square, metallic patches as shown in Fig. 9(a). The patches are electrically small where their side length is much less than the free space wavelength at the operating frequency. One feed point is at the center of the antenna. Each small patch is connected

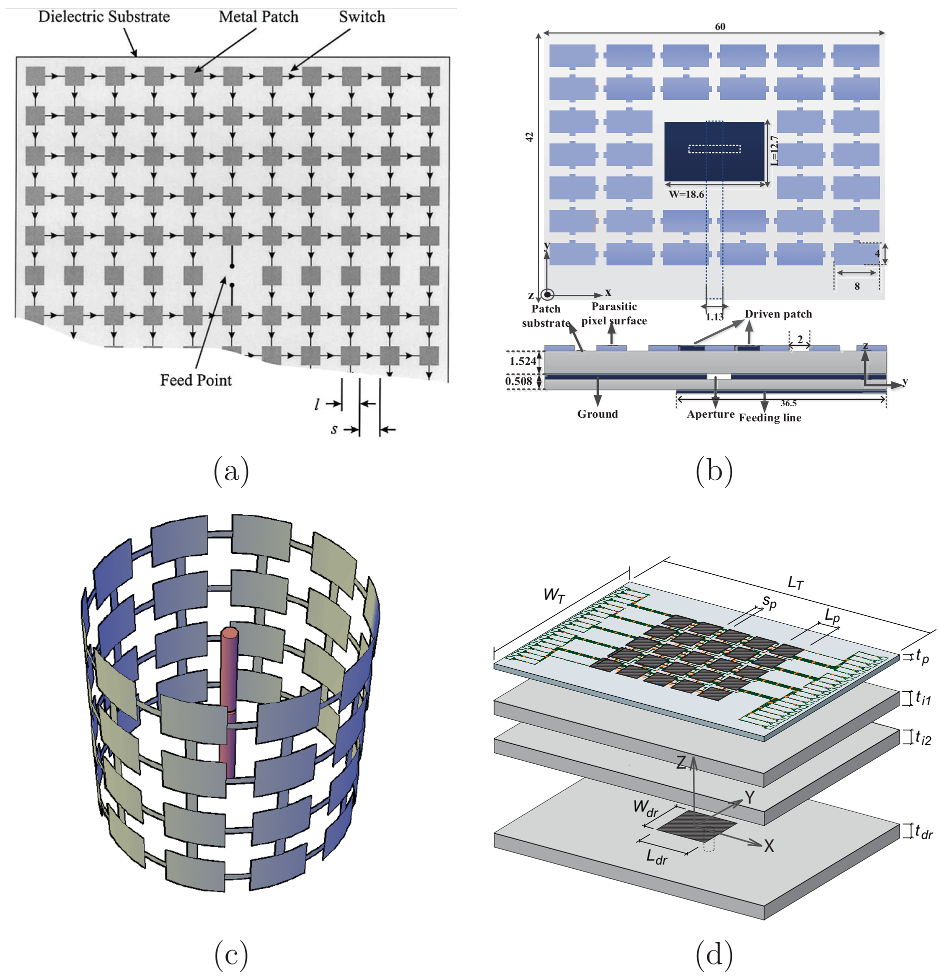

Figure 9: Different examples of parasitic pixel surface suited for conventional radiation structures. (a) Conceptual drawing of a reconfigurable antenna based on switched links between pixel patches (Pringle et al. [22], ©IEEE 2004). (b) Plan and elevation view of the proposed antenna as in [28] ©IEEE 2016. (c) Conformal parasitic surface suited for an omni-directional antenna (Rodrigo et al. [32], ©IEEE 2011). (d) Patch reconfigurable antenna using a parasitic pixel layer (Rodrigo et al. [32], ©IEEE 2011).

to its neighboring patches by a switch which is indicated by the arrows in Fig. 9(a). The switch configurations for different performance goals are determined through the genetic algorithm optimization. A prototype of this antenna was designed showing that electronic reconfiguration can be used to change the bandwidth of operation or steer the pattern of the antenna.

The parasitic pixel surface can be implemented by other approaches. One example is shown in Fig. 9(b). This architecture consists of a driven patch antenna which is surrounded by a rectangular grid of parasitic pixels. Parasitic pixels are connected to their neighboring elements by a switching mechanism. The driven antenna is mutually coupled to the parasitic pixels, and when these parasitic elements are connected by appropriate connection, they can steer the beam toward desired direction. This antenna can steer the beam over $\pm 40°$ in both the azimuth and elevation planes without using phase shifters.

Other examples of a parasitic pixel surface use the same conceptual approach as that in [22] but implemented it in a different structures as shown in Fig. 9(c) and (d). In these structures the reconfigurability of antenna properties is achieved by coupling the electromagnetic (EM) energy from the driven antenna to a reconfigurable parasitic layer. To enhance the coupling, the parasitic surface should be located in regions where the driven element generates strong fields. Therefore, the pixel surface arrangement is dependent to the radiation pattern of the driven antenna. For instance, for omni-directional antennas, a conformal cylindrical pixel surface can be used as shown in Fig. 9(c), while for a directional antenna a superstrate is located in the direction of maximum radiation as shown in Fig. 9(d).

These structures show their exceptional performance due to the possibility of creating a rich variety of antenna shapes by activating switch configurations. However, a number of shortfalls are associated with these structures. These structures have a massive biasing circuit due to the considerable number of RF switches which severely affects the antenna cost and efficiency. Moreover, to find the proper connections between pixels for a desired beam direction, an efficient optimization method is needed which will introduce more complexity in the antenna design.

Chapter 3

Theoretical Background and Methodology

3.1 Introduction

This chapter presents the theoretical background and methodology required for designing the parasitic array radiators. Mutual coupling phenomena which is the most fundamental concept to define the nature of ESPARs is discussed in Section 3.2. We also try to introduce a methodology for designing the ESPAR antenna and finding the proper reactive loads for steering the beam toward the desired direction. Dielectric resonator antennas are introduced in Section 3.3. We make use of this antenna as the main elements for the designed ESPAR due to its advantages over the traditional antennas such as patch, monopole and dipoles. Two common shapes of DRA and the various coupling methods are discussed briefly in this section.

3.2 Mutual Coupling

The electromagnetic interaction between the antenna elements in a multielement antenna is called mutual coupling. Mutual coupling is a fundamental concept that can define the

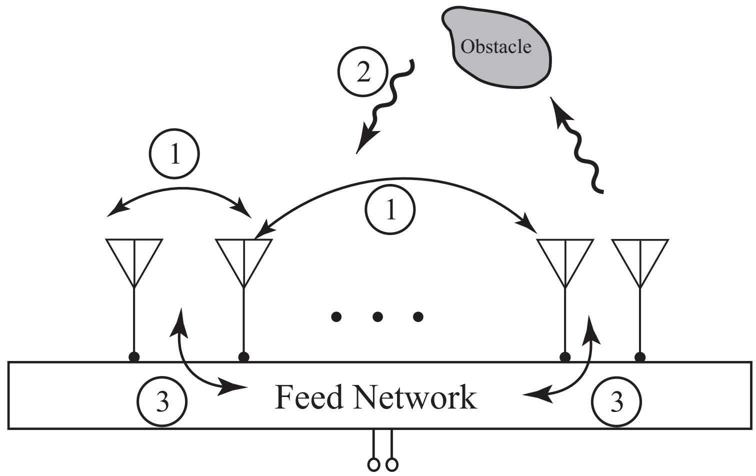

Figure 10: Mechanisms for coupling between elements of a multi-element antenna. (1) Direct space coupling between elements. (2) Indirect coupling that can occur by scattering from nearby objects such as a support tower. (3) Feeding network that provides a path for coupling.

nature of parasitic arrays. Therefore, it should be discussed in detail to give a better understanding of how the parasitic array works. This phenomenon alters the current distribution of the elements which affects their field radiated and the input impedance [37]. This topic is comprehensively studied in many antenna texts [37–39]. In this section we will have a brief overview on mutual coupling phenomena.

3.2.1 Mutual Coupling Between Active Elements

As shown in Fig. 10, three mechanisms responsible for mutual coupling in a multi-element antenna [38]:

(1) Direct space coupling between elements.

(2) Indirect coupling that can occur by scattering from nearby objects such as a support tower.

(3) Feeding network that provides a path for coupling.

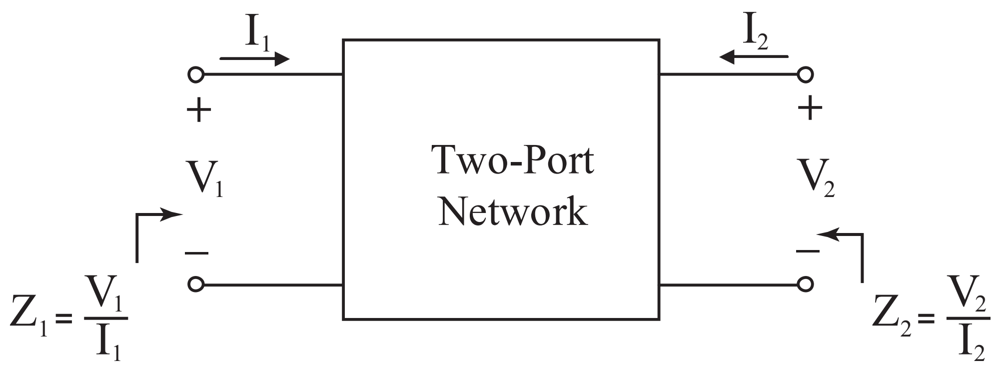

Figure 11: Two-port network equivalent of a simplified multi-element antenna consists of two elements.

It is worth noting that in practice, by providing proper impedance matching at each element, the feed network coupling can be minimized. To simplify the analysis, it is assumed that multielement antenna consists of two elements and the feeding network which are fully decoupled. Therefore, the system can be represented by a two-port (four-terminal) network, as shown in Fig. 11, where V_i and I_i show, respectively, the voltage and current seen at the terminal of the i_{th} ports (port 1 and 2). Furthermore, Z_i is the equivalent impedance seen at the i_{th} terminal in the presence of other elements or obstacles which is referred to as "the driving-point impedance" [37]. Z_i depends on the self-impedance (input impedance in the absence of any obstacle or other element) and the mutual impedance between the driven element and the other obstacles or elements [37]. Therefore, the voltage-current relations can be designed by:

$$\begin{aligned} V_1 &= Z_{11}I_1 + Z_{12}I2 \\ V_2 &= Z_{21}I_1 + Z_{22}I2 \end{aligned} \tag{1}$$

where

$$Z_{11} = \left.\frac{V_1}{I_1}\right|_{I_2=0} \tag{2}$$

relates the voltage produced at terminal 1 due to the current at 1 when port #2 open-circuited and

$$Z_{12} = \frac{V_1}{I_2}\bigg|_{I_1=0} \tag{3}$$

relates the voltage produced at terminal 2 due to the current at 1 when port #1 open-circuited. The parameters

$$Z_{21} = \frac{V_2}{I_1}\bigg|_{I_2=0} \tag{4}$$

and

$$Z_{22} = \frac{V_2}{I_2}\bigg|_{I_1=0} \tag{5}$$

denotes the mutual impedance between ports which for a reciprocal network are equal to each other ($Z_{11} = Z_{22}$)

Now the driving-point impedance of antennas can be found by using (1) as:

$$\begin{aligned} Z_{1d} &= \frac{V_1}{I_1} = Z_{11} + Z_{12}(\frac{I_2}{I_1}) \\ Z_{2d} &= \frac{V_2}{I_2} = Z_{22} + Z_{21}(\frac{I_1}{I_2}) \end{aligned} \tag{6}$$

As it can be observed, the driving-point impedance depends on the I_1, I_2, the mutual impedances, and the self-input impedances. Therefore, to match any antenna, it is the driving-point impedance that must be matched.

Now by using network theory we can extend (1) to an N port array [39]:

$$\begin{aligned} V_1 &= Z_{11}I_1 + Z_{12}I_2 + \cdots + Z_{1N}I_N \\ V_2 &= Z_{21}I_1 + Z_{22}I_2 + \cdots + Z_{2N}I_N \\ \vdots &= \qquad\qquad\qquad\qquad \vdots \\ V_N &= Z_{N1}I_1 + Z_{N2}I_2 + \cdots + Z_{NN}I_N \end{aligned} \tag{7}$$

which can be rewritten in matrix form:

$$\begin{bmatrix} V_1 \\ V_2 \\ V_3 \\ \vdots \\ V_N \end{bmatrix} = \begin{bmatrix} Z_{11} & Z_{12} & Z_{13} & \dots & Z_{1N} \\ Z_{21} & Z_{22} & Z_{23} & \dots & Z_{2N} \\ Z_{31} & Z_{32} & Z_{33} & \dots & Z_{3N} \\ \vdots & \vdots & \vdots & \ddots & \vdots \\ Z_{N1} & Z_{N2} & Z_{N3} & \dots & Z_{NN} \end{bmatrix} \begin{bmatrix} I_1 \\ I_2 \\ I_3 \\ \vdots \\ I_N \end{bmatrix} \tag{8}$$

and can be simplified to

$$\mathbf{V} = \mathbf{ZI}. \tag{9}$$

The driving-point impedance at n_{th} port can be found at:

$$Z_n = \frac{V_n}{I_n} \tag{10}$$

which by using (7) becomes:

$$Z_n = Z_{n1}\frac{I_1}{I_n} + Z_{n2}\frac{I_2}{I_n} + Z_{n3}\frac{I_3}{I_n} + ... + Z_{nN}\frac{I_N}{I_n}. \tag{11}$$

It is worth noting that the currents in (9) can be solved through the inversion of impedance matrix as:

$$\mathbf{I} = \mathbf{Z^{-1}V} \tag{12}$$

In this case, the currents I_n contain all information regarding the mutual coupling and can be used in finding the total radiation pattern of the array. It has been previously shown in [40], that the far-field radiation patterns can be derived through superposition. To this end, the total electric field can be written as :

$$E_{total} = \sum_{n=1}^{N} I_n E_n^{oc} \tag{13}$$

where, E_{total} represents the total electric field and E_n^{oc} is the field radiated when a unit current exists at n_{th} port while all other ports are left open circuited. Thus, summation

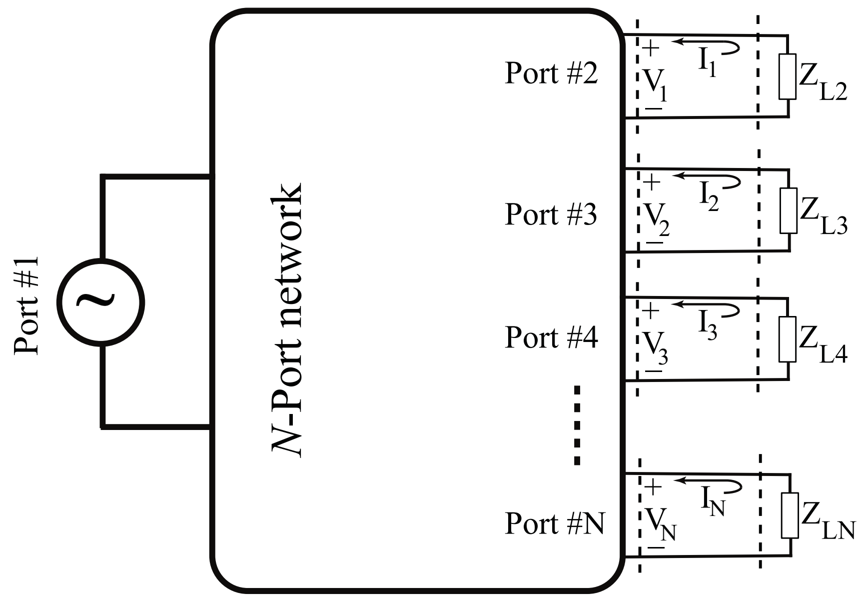

Figure 12: Multi-port network representing the mutual coupling between active and loaded parasitic elements

of all element contributions realizes the total field.

3.2.2 Mutual Coupling Between Active and Loaded Parasitic Elements

In parasitic arrays, there are elements that have no current excitation of their own. These elements have a substantial current induced by radiation from nearby elements. These are known as parasitic elements and play an important role in the overall performance of the entire parasitic antenna system.

Let suppose a parasitic array consisting of one active and $N-1$ passive elements (a total of N elements). This array can be represented by a N-port network, as shown in Fig. 12. The voltages and currents at each element's feeding point can be defined by (7). In parasitic arrays, the parasitic elements usually are terminated by reactive loads, short circuit (S.C.), or open circuit (O.C.). Therefore in a general form, we can consider them loaded with complex impedances of Z_L (for S.C. $Z_L = 0$ and for O.C. $Z_L = \infty$). Then the voltage of parasitic ports is equal to:

$$V_n = -I_n Z_{Ln} \tag{14}$$

where Z_{Ln} denotes the impedance load of the n_{th} element. Substituting (14) into (7) it follows that:

$$\begin{aligned} V_1 &= Z_{11}I_1 + Z_{12}I_2 + \cdots + Z_{1N}I_N \\ -I_1 Z_{L1} &= Z_{21}I_1 + Z_{22}I_2 + \cdots + Z_{2N}I_N \\ \vdots \ &= \qquad\qquad\qquad\qquad \vdots \\ -I_n Z_{Ln} &= Z_{N1}I_1 + Z_{N2}I_2 + \cdots + Z_{NN}I_N \end{aligned} \tag{15}$$

or

$$\begin{aligned} V_1 &= Z_{11}I_1 + Z_{12}I_2 + \cdots + Z_{1N}I_N \\ 0 &= Z_{21}I_1 + (Z_{22} + I_2 Z_{L2})I_2 + \cdots + Z_{2N}I_N \\ \vdots \ &= \qquad\qquad\qquad\qquad \vdots \\ 0 &= Z_{N1}I_1 + Z_{N2}I_2 + \cdots + (Z_{NN} + I_N Z_{LN})I_N \end{aligned} \tag{16}$$

which can be rewritten in matrix form:

$$\begin{bmatrix} V_1 \\ 0 \\ 0 \\ \vdots \\ 0 \end{bmatrix} = \begin{bmatrix} Z_{11} & Z_{12} & Z_{13} & \dots & Z_{1N} \\ Z_{21} & Z_{22} + I_2 Z_{L2} & Z_{23} & \dots & Z_{2N} \\ Z_{31} & Z_{32} & Z_{33} + I_3 Z_{L3} & \dots & Z_{3N} \\ \vdots & \vdots & \vdots & \ddots & \vdots \\ Z_{N1} & Z_{N2} & Z_{N3} & \dots & Z_{NN} + I_N Z_{LN} \end{bmatrix} \begin{bmatrix} I_1 \\ I_2 \\ I_3 \\ \vdots \\ I_N \end{bmatrix} \tag{17}$$

or simply :

$$\mathbf{V} = [\mathbf{Z} + \mathbf{Z_L}]\mathbf{I} \tag{18}$$

where the diagonal matrix

$$\mathbf{Z_L} = \begin{bmatrix} 0 & 0 & 0 & \dots & 0 \\ 0 & Z_{L2} & 0 & \dots & 0 \\ 0 & 0 & Z_{33} & \dots & 0 \\ \vdots & \vdots & \vdots & \ddots & \vdots \\ 0 & 0 & 0 & \dots & Z_{LN} \end{bmatrix} \tag{19}$$

The ratios between currents on the passive elements and the current on the driven antenna can be obtained as:

$$\begin{bmatrix} \frac{I_1}{I_0} \\ \frac{I_2}{I_0} \\ \vdots \\ \frac{I_n}{I_0} \end{bmatrix} = \begin{bmatrix} Z_{11} + Z_{L1} & Z_{12} & \dots & Z_{n1} \\ Z_{21} & Z_{22} + Z_{L2} & \dots & Z_{n2} \\ \vdots & \vdots & \ddots & \vdots \\ Z_{n1} & Z_{n2} & \dots & Z_{nn} + Z_{Ln} \end{bmatrix}^{-1} \begin{bmatrix} -Z_{10} \\ -Z_{20} \\ \vdots \\ -Z_{n0} \end{bmatrix} \tag{20}$$

the currents I_n contain all the information of mutual coupling between the elements and can be used in finding the total radiation pattern of the array.

3.3 Dielectric Resonator Antenna

In this thesis, the main element of the designed ESPAR is dielectric resonator antenna (DRA). Thus, in this section a brief review of the fundamental operation and various aspects of DRA technology are discussed.

Dielectric Resonator Antennas (DRAs) consists of a block of ceramic material of various shapes that can radiate energy into space when excited appropriately [21]. These ceramic resonators have primarily been used in microwave circuits in areas such as oscillators and filters. In these applications, dielectric resonators are fabricated of low-loss materials with high relative permittivity which are often enclosed in metal cavities to prevent radiation

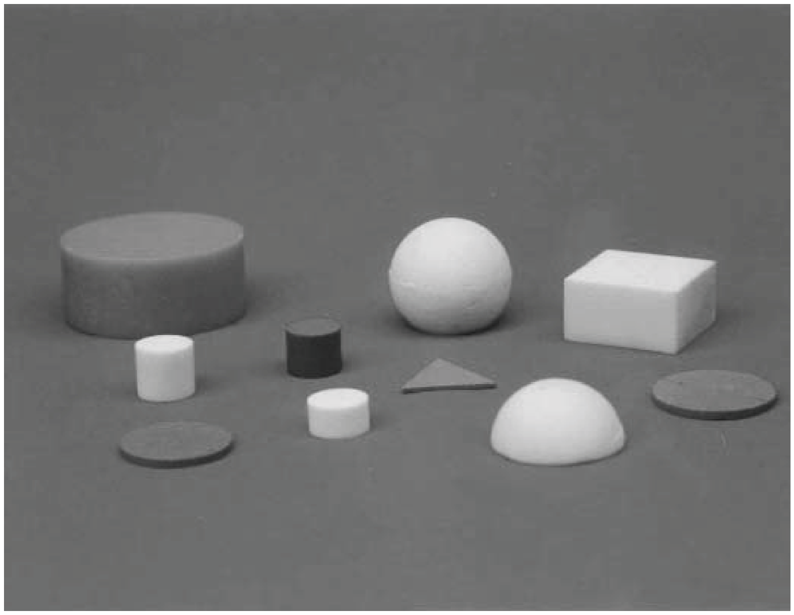

Figure 13: DRAs of various shapes. The photo shows cylindrical, rectangular, hemispherical, low-profile circular-disk, low-profile triangular, and spherical-cap DRAs (Petosa [21], © 2007 ARTECH HOUSE, INC.).

and to maintain a high Q factor. It was found in 1987 by Richtmyer [41], that by removing the shielding and proper feeding, dielectric resonators can become efficient radiators. This research has further improved by McA llister and Shen [42–44], who investigated the characteristics of DRAs in various shapes such as hemispherical, cylindrical, and rectangular shapes. These researchers created the foundation for future investigations of the DRAs. Nowadays, DRAs have enjoyed a strong following among antenna engineers due to their attractive features which are summarized below:

- The dimensions of a DRA are inversely proportional to λ_0/ϵ_r, where λ_0 is free space wavelength at the resonant frequency and ϵ_r is the dielectric constant of the resonator material. Therefore, the size of DRA can be reduced significantly by increasing the ϵ_r.

- DRA has a high radiation efficiency due to the lack of conductor loss and surface waves. This feature is especially attractive for millimeter (mm) wave frequencies, where the loss in metal antennas can be high [45]. It is noted that the only loss for a DRA is that due to the imperfect dielectric material, which can be very small in practice [46].

- Several coupling schemes can be used for a DRA, employing the common transmission lines at microwave frequencies such as probes, slots, microstrip lines and coplanar waveguide lines. This makes DRAs suitable for integration into different technologies.

- DRAs can operate over a wide range of frequencies by suitably choosing resonator parameters.

- Each shape of a DRA has several modes that can be excited by the proper feeding mechanism. Therefore, different radiation characteristics can be obtained to provide different coverage requirements.

According to these features, DRAs take their place among common antennas, such as wire, microstrip, horn, and reflector antennas [46]. DRAs can be fabricated in various shapes as shown in Fig. 13. The rectangular and cylindrical DRAs that are used in this thesis, are briefly described in the following sections.

3.3.1 Cylindrical DRA

The cylindrical DRA is characterized by a height h, a radius a, and a dielectric constant ϵ_r, as shown in Fig. 14(a). The modes of a cylindrical resonator can be categorized into three distinct types: TE, TM, and hybrid. The hybrid modes can be further subdivided into two groups of HE and EH [45]. By adding subscripts of n, m and δ to each mode as $TE_{0mp+\delta}$, $TM_{0mp+\delta}$, $HE_{nmp+\delta}$ and $EH_{nmp+\delta}$, the variation of fields along the azimuthal, radial, and z-direction inside the resonator can be shown, respectively. It is shown in [47] that the $TM_{01\delta}$ and $HE_{11\delta}$ modes can be supported by a cylindrical DRA which is placed above a perfectly conducting plane. The fields for these two modes are sketched in Fig.

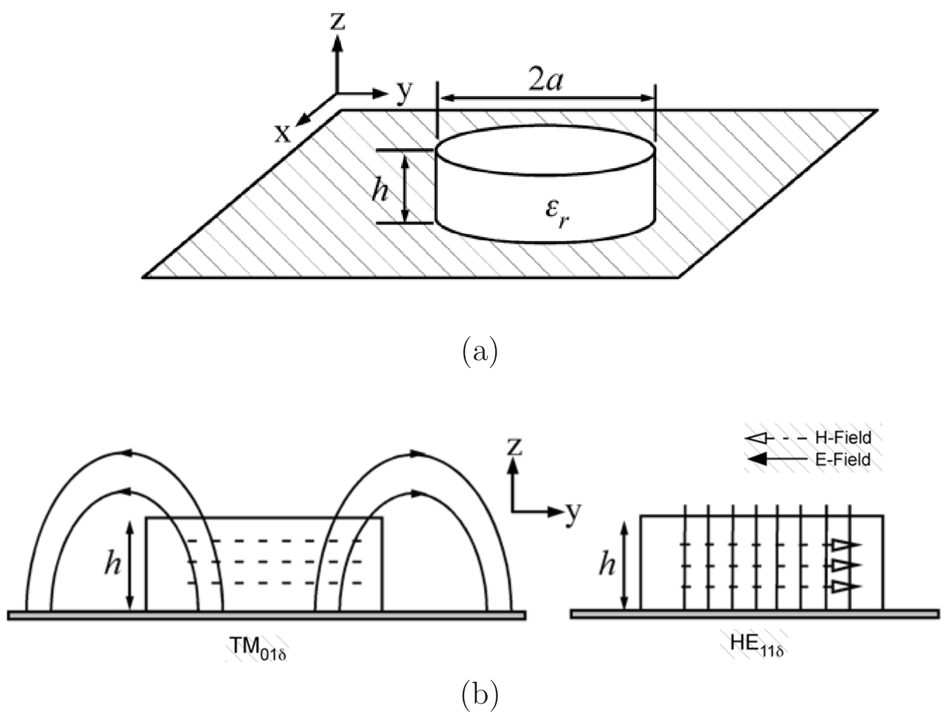

Figure 14: (a) Geometry of the cylindrical RA. (b) Sketch of the cylindrical DRA field configurations (Petosa [21], © 2007 ARTECH HOUSE, INC.).

14(b). The far-field radiation pattern of the TM_{01} mode looks like a quarter wavelength monopole above ground plane. The radiation pattern of the HE_{11} looks like the radiation pattern of a half wavelength narrow slot on a ground plane or a half wavelength electric dipole parallel to the ground plane [48].

3.3.2 Rectangular DRA

The rectangular DRA is characterized by a height h, a width w, a depth d, and a dielectric constant ϵ_r as shown in Fig. 15 . Therefore, it has one more degree of freedom for tuning the resonant frequency comparing to cylindrical DRA. Furthermore, the rectangular DRA does not support degenerate modes and resonant frequencies of the different modes can be chosen to be different from each other by properly choosing the three dimensions of the resonator [45]. The modes of an isolated rectangular DRA can be categorized into two major types: TE and TM. However, the presence of the lowest order TM modes has not

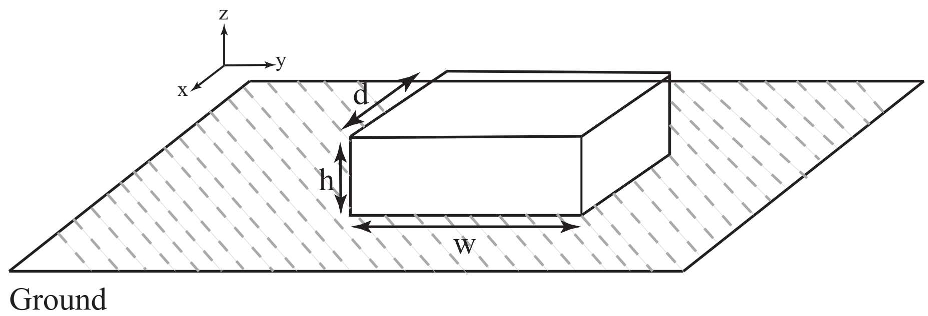

(a)

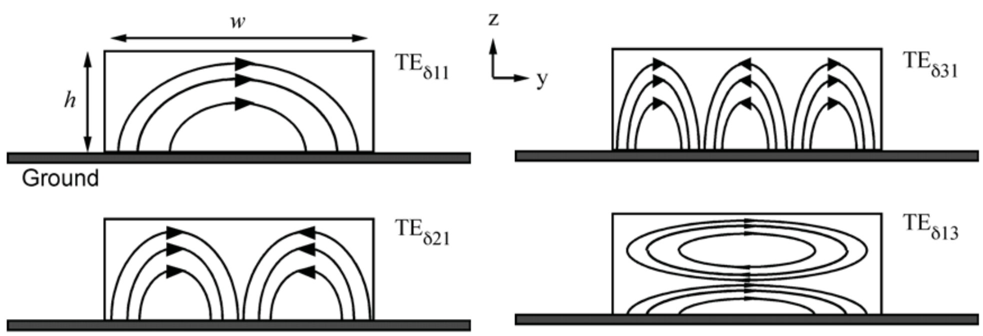

(b)

Figure 15: (a) Geometry of the rectangular DRA. (b) Sketches of the E-fields for selected higher-order modes within the rectangular DRA (Petosa [21], © 2007 ARTECH HOUSE, INC.).

been confirmed experimentally. The structure which is shown in Fig. 15(a) can support TE_z, TE_x and TE_y. According to [45], if the smallest dimensions of the DRA lies in the z-direction, the lowest order mode will be TE. This mode radiates like a magnetic dipole oriented along the z-direction and is located at the center of the resonator. Some possible resonant modes of a rectangular DRA is shown in Fig. 15(b).

3.3.3 Coupling Methods

For most practical applications, power must be coupled into or out of the DRA through one or more ports [47]. As mentioned earlier, DRAs have simple coupling schemes that are common transmission lines at microwave frequencies such as probes, slots, microstrip lines and coplanar waveguide lines. The amount of coupling, the excited mode and the

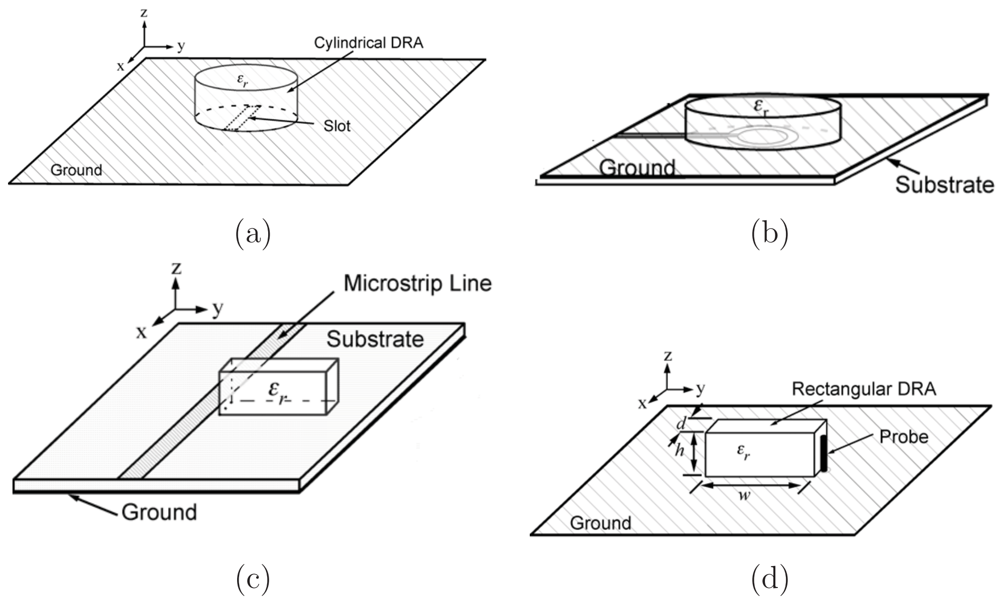

Figure 16: Various coupling feeding mechanisms for DRA. (a) Aperture coupled slot. (b) Coplanar loop coupling. (c) Microstrip line coupling. (d) Probe coupling (Petosa [21], © 2007 ARTECH HOUSE, INC.).

frequency response are determined by the type and the location of the port with respect to the DRA. A knowledge of the internal field configuration for different modes can assist in determining what type of feed is best suited and where the feed should be located to optimize the DRA excitation [48]. The most common coupling methods for DRA are shown in Fig. 16.

3.4 Summary

In this chapter, the methodology and theoretical background required for designing beam-reconfigurable antennas using parasitic elements are presented. Mutual coupling phenomenon and dielectric resonator antennas are discussed. In addition, a brief discussion about commercial software packages used in this work and their associated numerical techniques is presented.

Chapter 4

Realization of Large ESPAR

4.1 Introduction

In Chapter 2, we have reviewed recent publications on ESPAR. In these designs the ESPAR is considered specifically as an individual three/five-elements. However, many applications require reconfigurable radiation characteristics that may not be achievable with the three/five-elements ESPAR. In this chapter, we have attempted to highlight those practical problems that are critical in implementing a large ESPAR. These issues include the design of an appropriate feeding network for large ESPAR and using the perforation technique to facilitate the fabrication requirements for the embedded DRAs. Moreover, to overcome the grating lobe problem the interleaved subarrays is utilized, which supress the grating lobes with better scanning capabilities in all azimuthal directions. The designed feeding network is of parallel-series combination, which minimizes the feeding insertion loss due to the reduction of the overall length of the transmission lines [49]. In addition, the space usage of the given aperture is significantly improved in a parallel-series-fed architecture. The perforation technique is used to fabricate an array of DRAs from a single dielectric sheet to alleviate the problems associated with aligning and bonding the individual elements of the DRA [47]. This technique showed good agreement between the perforated DRAs and their equivalent structures. To best explore the differences and advantages of our approach, the proposed ESPAR is compared with the conventional phased array antenna and steerable reflectarray antenna (RA). We also propose a prototype of the large ESPAR antenna for broadside, proving the exceptional performance of the large ESPAR.

This chapter commences with the antenna design of the proposed subarray. Techniques for designing a large ESPAR are discussed in section 4.4. The designed large ESPAR with traditional phased array antennas and beam reconfigurable RA are compared in Section 4.5. Finally, the fabrication techniques and the measurements are shown Section 4.6.

4.2 Design of Single DRA

The single DRA design will be investigated in this chapter. A rectangular DRA was chosen as the main element which is excited in its fundamental mode. For the fundamental mode of TE^x_{111}, a sketch of the field configuration is shown in Fig. 17. As observed, the H_x component of the magnetic field is strong at the center of the DRA which is similar to those produced by a short magnetic dipoles. This knowledge of the internal field configuration is essential for choosing the right coupling method to excite the desired mode.

In this design, the DRA is fed by a 50 Ohm aperture coupled microstrip line with slot lengths ($Slot_l$) and the feed line position relative to the slots (L_s). The aperture-coupled feeding is chosen due to its advantages such as increased substrate space for antenna elements and feed lines and its convenient integration for active arrays [50]. Moreover, in an ESPAR, this feeding technique prevents the placing of all the biasing lines of the varactors in the same plane of the radiating elements, which will minimize their effect on the antenna radiation characteristics.

The electric fields within a rectangular slot are sketched in Fig. 18. As it can be observed, the slot is considered as an equivalent magnetic current whose direction is parallel to the slot length [21]. To excite the desired mode, the slot should be located in a region

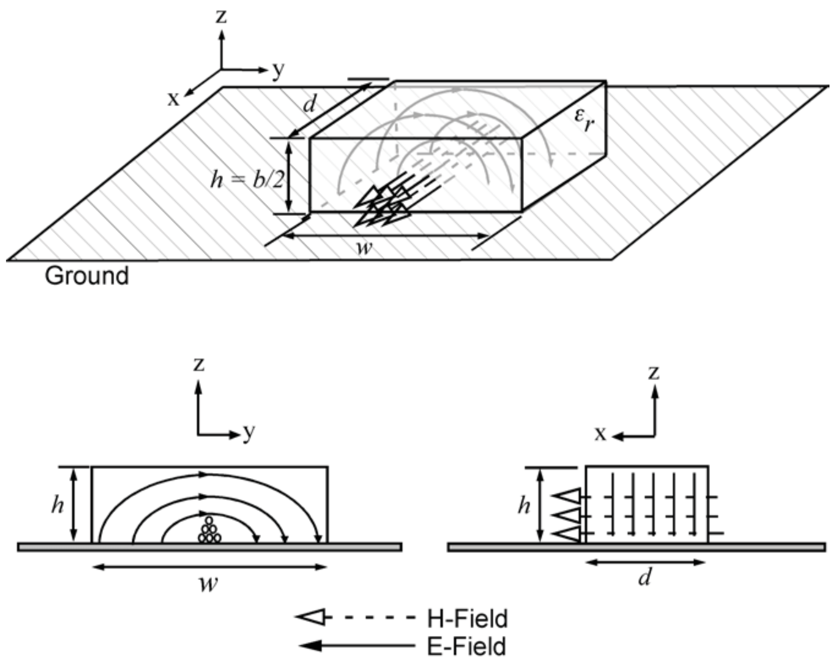

Figure 17: Sketch of the fields for the TE^{x}_{111} mode of the rectangular DRA (Petosa [21], ©2007 ARTECH HOUSE, INC.).

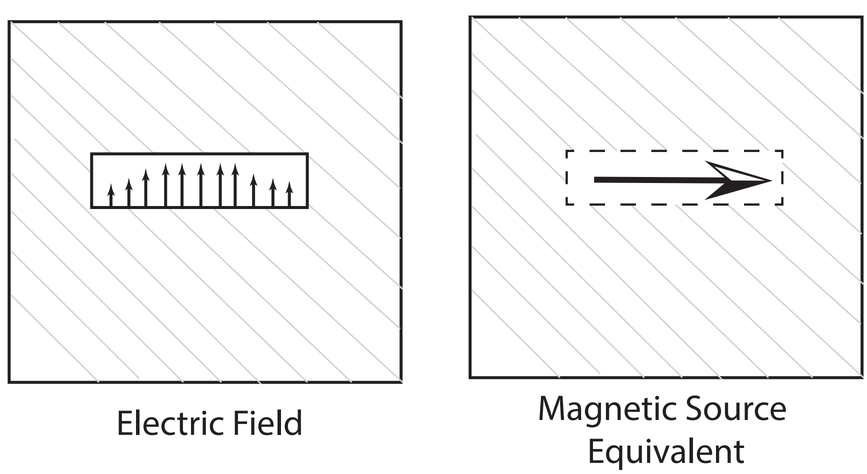

Figure 18: Equivalent magnetic current for slot apertures (Petosa [21], ©2007 ARTECH HOUSE, INC.).

of strong magnetic fields. Thus, by considering Fig. 17, the slot should be placed at the center of DRA, ensuring the strong coupling to the internal magnetic fields of TE^{y}_{111}.

4.3 Design of DRA-ESPAR Subarray

The proposed subarray consists of one driven DRA, coupled to two parasitic DRAs in both E- and H-plane. The distance between the elements in the E-plane differs from those in the H-plane, due to the different mutual coupling levels in the E- and H-planes. It is essential to note that the H-plane coupling does not change the phase of the DRA modes while the E-plane coupling changes the polarities of the parasitic elements opposite to the driven element when the elements are much closer to each other with a distance less than a half wavelength. Since the E-plane coupling is necessary for beam scanning in the elevation plane, we increase the separation between the elements in the E-plane. To have a better explanation, the E-field distribution of a driven DRA, which is coupled to two parasitic DRA in E-plane is simulated and shown in Fig. 19(a). It can be found from this figure that for the coupling gap of 0.2 mm, the E-field on the parasitic DRAs is out of phase to the driven DRA. The phase difference of the electrical field of specific points in the driven DRA and one parasitic DRA is plotted for various space coupling in Fig. 19(b). It can be seen that by increasing the coupling gap, the phase difference can be reduced. However, there should be a trade off for increasing the space coupling since it can reduce the mutual coupling level, which is necessary for exciting the parasitic DRAs.

Since the goal is to fabricate an array of DRAs from a single dielectric sheet, the DRAs have been formed by perforating the substrate material with a lattice of holes. This technique eliminates the need to align and bond the individual DRA elements, which are somehow impractical for the large array fabrication. The effective dielectric constant can be approximated by the diameter and spacing of the holes, which is defined as [51]:

$$\epsilon_{eff} = \epsilon_r\big((1 - \frac{\pi}{2}(\frac{d}{d+g})^2\big) + \frac{\pi}{2}(\frac{d}{d+g})^2 \tag{21}$$

where d is hole diameter and g is the is the edge to edge distance between the holes as shown in the insert of Fig. 20. The effective permittivity versus via-hole diameter is shown

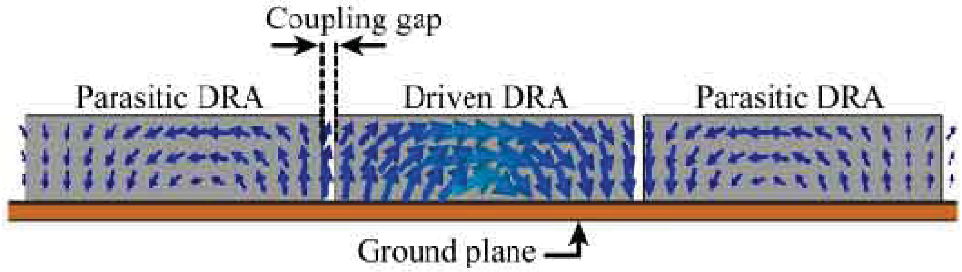

(a)

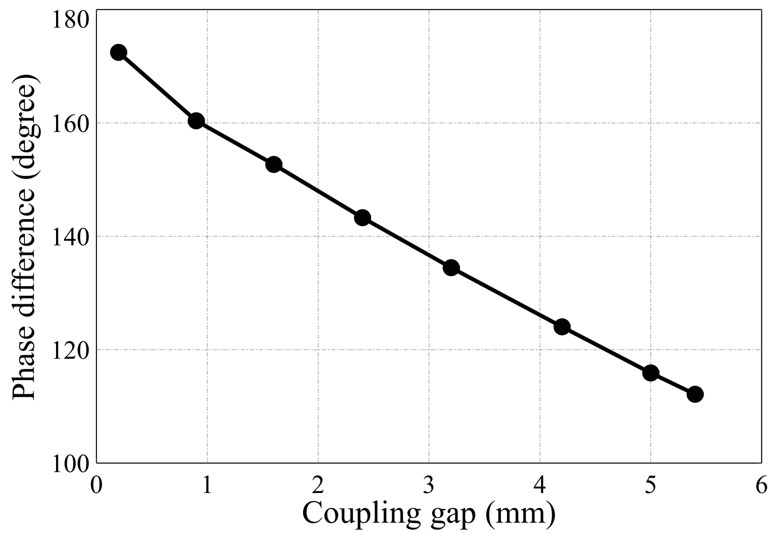

(b)

Figure 19: (a) Field distribution of an E-plane planar subarray. (b) Phase difference of E-filed for edge to edge point in driven and parasitic DRA according to different coupling gaps.

in Fig. 20. From this figure, the dielectric constant of surrounding areas of the embedded DRAs can be reduced from 10.2 to 3.1 by perforating lattice of via-holes of diameter 2.1 mm with a spacing of 0.25 mm.

Fig. 21 shows the basic geometry of the proposed DRA subarray. The antenna dielectric layer consists of Rogers Duroid 6010 substrate with $\epsilon_r = 10.2$, $tan\delta = 0.0009$, and a thickness of 2.54, placed above the feed substrate of Rogers RO5870 substrate with $\epsilon_r = 2.33$, $tan\delta = 0.0027$, and a thickness of 0.508 mm. The DRA width (a) is 9.6 mm, and its height (h) is 2.5 mm. Therefore, the TE^y_{111} is the excited fundamental mode [45].

The parasitic dielectric resonator antennas in the E- and H-plane of the main DRA are

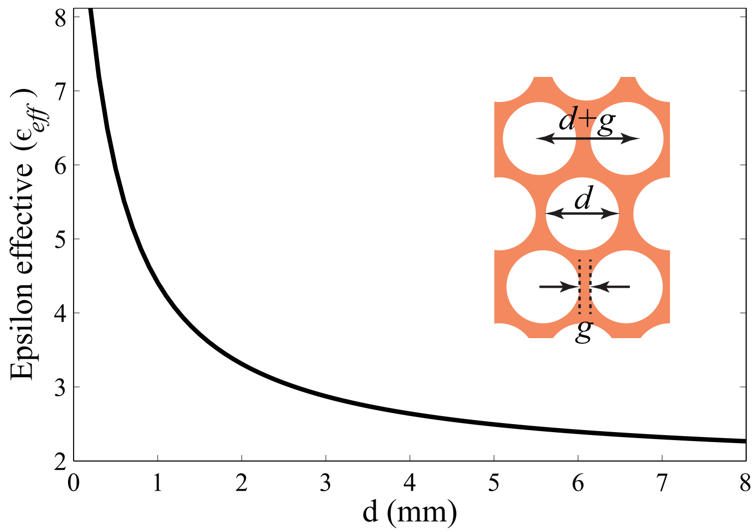

Figure 20: Variation of epsilon effective with different via diameters for the fixed coupling gap of .25mm.

excited by the mutual electromagnetic coupling while the phase shift necessary between the DRA elements is provided by loading the terminals of the parasitic elements with the proper reactive loads. The subarray is modeled at 10.5 GHz, using CST MWS. The varactors values for broadside direction are calculated based on the approach which will be introduced in the following section, and the results for return loss and radiation patterns are shown in Fig. 22. It is observed that the return loss and radiation patterns of the perforated DRA subarray are similar to those of the DRA surrounded by free space.

It is worth noting that in this subarray design, to achieve a better impedance matching the dimensions of the aperture coupled to the feed line of the parasitic DRAs are slightly changed with respect to the driven DRA. Mutual coupling affects strongly the matching of the elements as well as the induced voltages at the antenna terminals that in turn changes the current and consequently the effective input impedance. As shown in Fig. 22(a), the impedance matching with this tuning can be considerably improved compared to the subarray without tuning the coupling dimension, which was ignored in the previous studies.

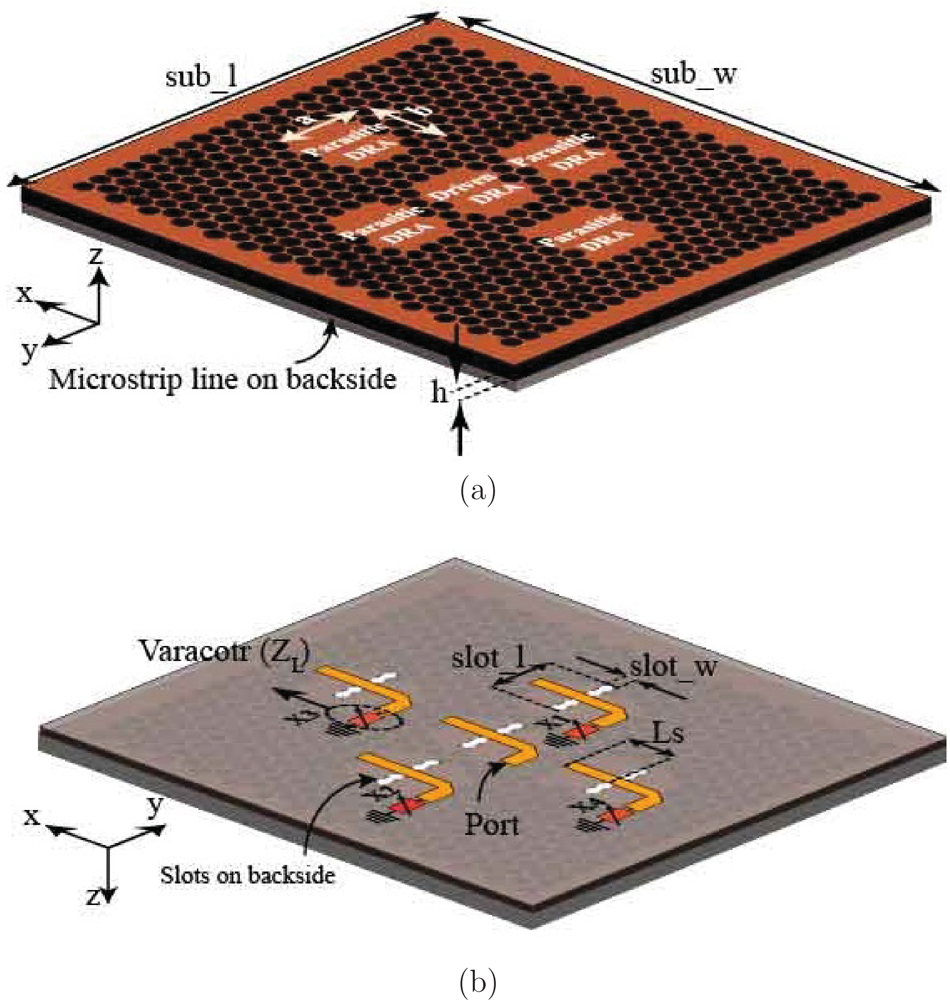

Figure 21: Proposed ESPAR subarray structure fed by aperture coupled lines at the back of the structure. (a) Perspective view from the top of subarray. (b) Perspective view from the bottom of subarray. ($sub_l = 51$ mm, $sub_w = 55$ mm, $slot_l = 5.2$ mm, $slot_w = 0.5$ mm, $Ls = 5.5$ mm, $a = b = 9.6$ mm and $h = 2.54$ mm).

4.3.1 Beam scanning and AF Considerations

The amplitude and phase of the induced parasitic currents control the scanning ability of the parasitic phased array. The magnitude of the parasitic currents can be determined by the gap distance between the driven antenna and the parasitic elements while the reactance of the loading elements controls the excitation phases. It should be noted that the reactance of the loading elements also affects the magnitude of the parasitic currents [52]. To find the proper reactive loads for the desired beam scanning direction,

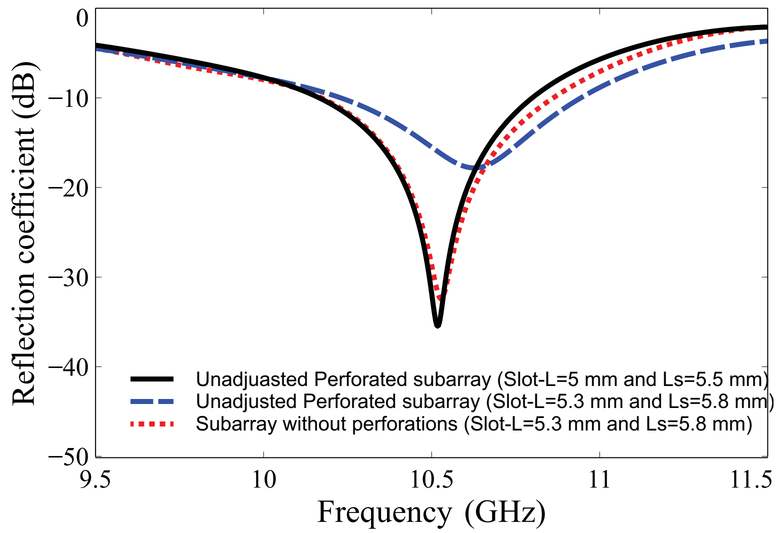

(a)

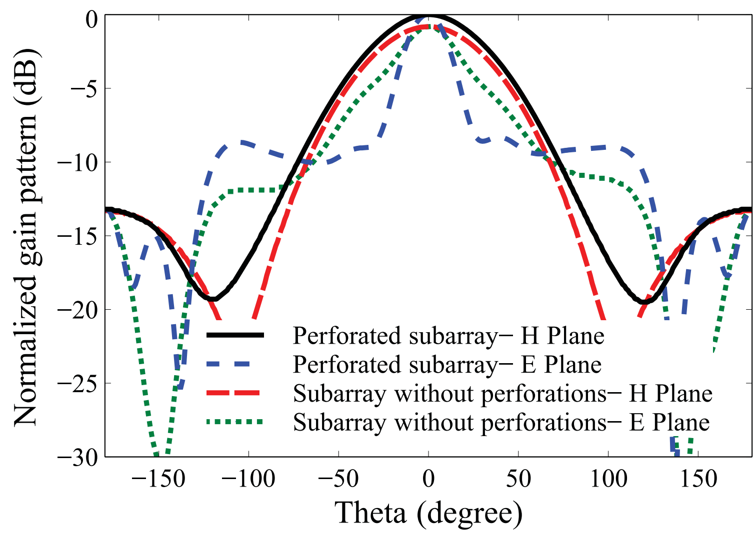

(b)

Figure 22: Simulated performance of the array of ESPAR subcell a) Reflection coefficient versus frequency b) Normalized radiation pattern in E-plane and H-plane.

the simple approach described in [13] can be used. The 5-element ESPAR can be assumed like a 5-port network as was shown in Chapter 2. Therefore, the voltage and the currents are related by the following impedance matrix:

$$\begin{bmatrix} V_1 \\ -I_2 Z_{L2} \\ -I_3 Z_{L3} \\ -I_4 Z_{L4} \\ -I_5 Z_{L5} \end{bmatrix} = \begin{bmatrix} Z_{11} & Z_{12} & Z_{13} & Z_{14} & Z_{15} \\ Z_{21} & Z_{22} & Z_{23} & Z_{24} & Z_{25} \\ Z_{31} & Z_{32} & Z_{33} & Z_{34} & Z_{35} \\ Z_{41} & Z_{42} & Z_{43} & Z_{44} & Z_{45} \\ Z_{51} & Z_{52} & Z_{53} & Z_{54} & Z_{55} \end{bmatrix} \begin{bmatrix} I_1 \\ I_2 \\ I_3 \\ I_4 \\ I_5 \end{bmatrix} \tag{22}$$

This matrix yields the following expressions for the ratios between the currents on four passive DRAs and the current on the driven DRA as expressed in (23):

$$\begin{bmatrix} \frac{I_2}{I_1} \\ \frac{I_3}{I_1} \\ \frac{I_4}{I_1} \\ \frac{I_5}{I_1} \end{bmatrix} = \begin{bmatrix} Z_{22} + Z_{L2} & Z_{23} & Z_{24} & Z_{25} \\ Z_{32} + Z_{L3} & Z_{33} & Z_{34} & Z_{35} \\ Z_{42} + Z_{L4} & Z_{43} & Z_{44} & Z_{45} \\ Z_{52} + Z_{L5} & Z_{53} & Z_{54} & Z_{55} \end{bmatrix}^{-1} \begin{bmatrix} -Z_{21} \\ -Z_{31} \\ -Z_{41} \\ -Z_{51} \end{bmatrix} \tag{23}$$

the normalized array factor of the subarray to the current on the driven DRA (I_1), which ultimately results in the beam scanning direction of θ_0 and ϕ_0 is found to be:

$$AF = \sum_{i=1}^{5} \left| \frac{I_{i1}}{I_0} \right| e^{j((k_0(\rho_i - a) + k_{x,z}\rho_i)\sin(\theta_0)\cos(\rho_0 - \rho_i)) + \mathrm{ang}\frac{I_i}{I_1})} \tag{24}$$

where ρ_i and ϕ_i are, respectively, the radial and azimuthal positions of the i_{th} element in the x-y plane. A corrective term suggested in [53] is also considered, which takes into account two different electric distance portion between the phase centers of the antennas: the distance in free-space with the free space wavenumber k_0, and the distance which is within the DRA with the relative resonant mode wavenumber $k_{x,z}$. Once the AF is known, the overall radiation pattern can be obtained by multiplying it with the element factor. According to (23) and (24), the proper values for the parasitic loads can be found for a specific beam direction.

Three different scanning cases are presented in Table 2. It is worth noting that in

Table 2: Scanning Schemes and Simulated Antenna Performances (All Values Given at 10.5 GHz)

	Z_{L1}	Z_{L2}	Z_{L3}	Z_{L4}	$\phi-$plane	Scan Angle (θ)
Case I	1 nH	1 nH	0.2 pF	0.2 pF	0°	0°
Case II	2 nH	0.2 pF	2 pF	0.1 pF	10°	–23°
Case III	0.5 pF	2.5 nH	1 nH	0.6 pF	18°	22°

practice and for real-time performance, simple and low-cost varactors and their bias networks can be used to change the reactive elements from a positive to a negative value. For instance, in [54] illustrates a simple design consisting of a varactor, which is combined with an open stub that generates both positive and negative reactances and is controllable by the biasing voltage. Fig. 23 shows the reflection coefficients and the simulated radiation patterns of the ESPAR phased array for different scanning cases described in Table 2. As shown in Fig. 23(a), the reflection coefficients are maintained below –25 dB at the operating frequency of all cases. Furthermore, it is clear that the scanning is achieved without degrading the radiation pattern characteristics as shown in Fig. 23(b).

4.4 Large ESPAR Concept

4.4.1 Design Techniques

As mentioned earlier, the primary subarray is intended to provide the required beam scanning capability. Utilizing subarrays to larger arrays can greatly simplify the feeding network design and reduces losses. In this section, the above subarray has been used for designing a large ESPAR. Layouts of the antenna array and feeding network for the full array are shown in Fig. 24. The array consists of 48 overlapped subarrays, which are placed next to each other using an interleaved arrangement. This technique reduces the projected distance between the subarrays, which results in eliminating the grating lobes for the scanning in any azimuthal plane. However, interleaved array requires complicated

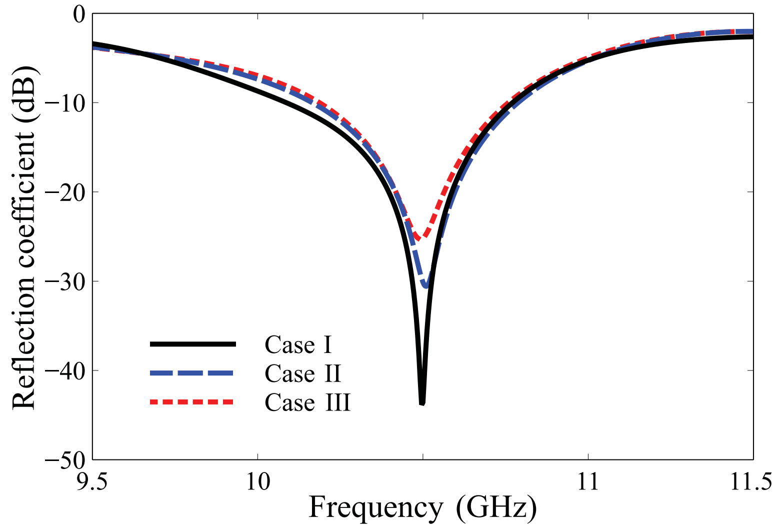

(a)

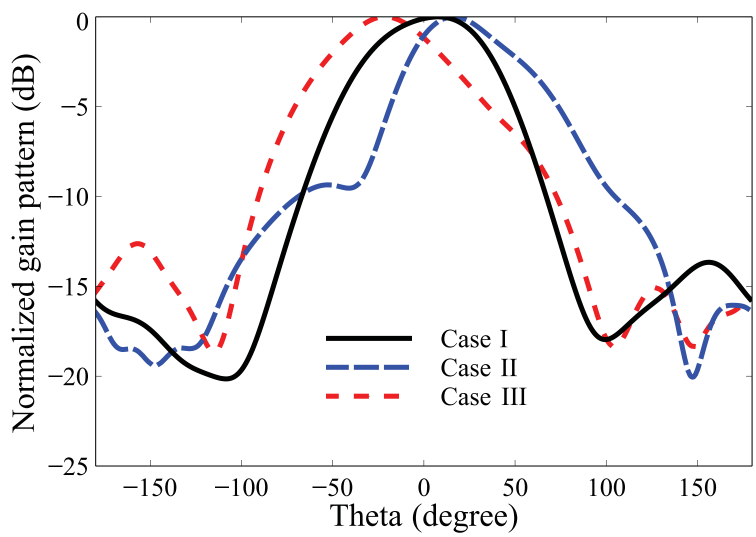

(b)

Figure 23: Simulation results of three different cases in Table 2, a) Input impedance matching, b) Normalized radiation pattern (The pattern is normalized to the maximum gain of the beam at 0 deg).

feeding network architectures that cannot be easily implemented using a conventional feeding network. This design utilizes a combination of series and parallel feeding schemes to achieve the desired feeding network shown in Fig. 24(b). This feeding network consists of a 1-16 parallel power divider along each row; three series-fed elements are connected. In addition, in each row, three phase shifters next to the driven elements can be considered

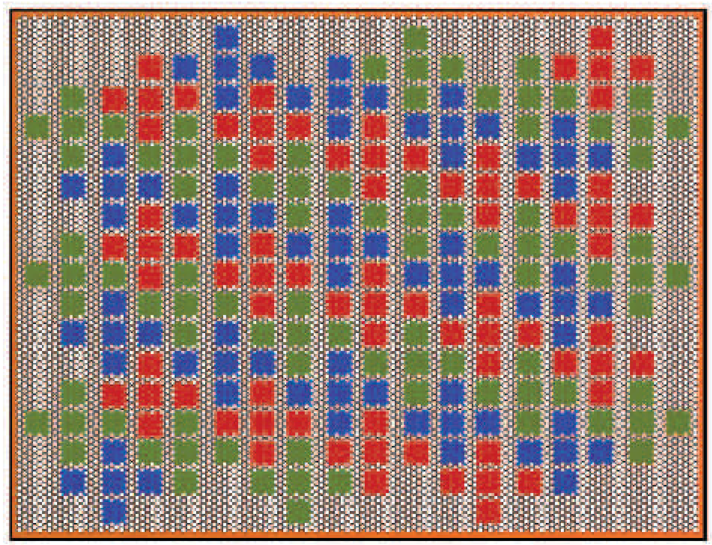

(a)

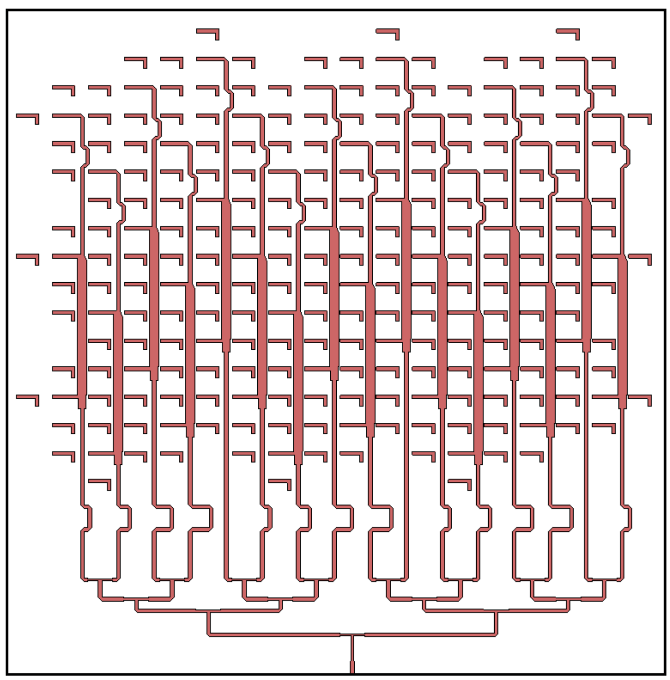

(b)

Figure 24: Layout of the proposed large ESPAR with subarrays in an interleaved arrangement, b) Power-splitter junctions of the proposed feeding network.

due to the beam scanning capability of the large ESPAR.

By implementing the proposed feeding network, the insertion loss of the transmission

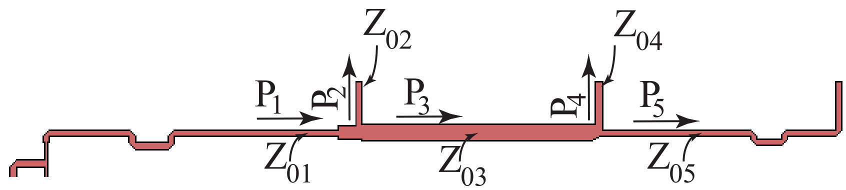

Figure 25: Power-splitter junctions of the proposed feeding network.

line can be minimized. Moreover, the space usage of the given aperture is significantly improved in a parallel-series-fed array architecture. It is worth noting that this feeding network should excite all the driven elements with equal amplitude and phase at the center frequency. The equal amplitude excitation for each element can be achieved by a proper design of the feed network junctions. To obtain the appropriate power split at each junction, the impedances of the transmission lines must be designed to transfer the required power ratio. Fig. 25 shows the power-splitter junctions of the proposed feeding network. The input power $P1$ enters the junction and is split into powers $P2$ and $P3$ with $P2 = P1/3$ and $P3 = 2P1/3$. By properly choosing the ratio of the characteristic impedances (Z_{02} and Z_{03}) of the transmission lines, the ratio of the output powers can be controlled by $P2/P3 = Z_{03}/Z_{02}$. The same methodology can be employed for the $P4$ and $P5$ which with the same characteristic impedance for Z_{04} and Z_{05}, the power $P3$ can be divided equally to the $P4 = P5 = P1/3$.

4.4.2 Simulation Results

The large ESPAR illustrated in Fig. 24 has been modeled in CST. Simulations of the large ESPAR are carried out in two steps. The first step is to optimize the feeding network accurately at center frequency to obtain a uniform power distribution for all driven elements. In the full wave simulation, the feeding network is considered without the antenna in which discrete 50-Ohm ports replace all the driven antennas. Therefore, the designed feed network can easily be optimized individually and successfully to set the desired excitation characteristics of the driven elements. The next step is to add the

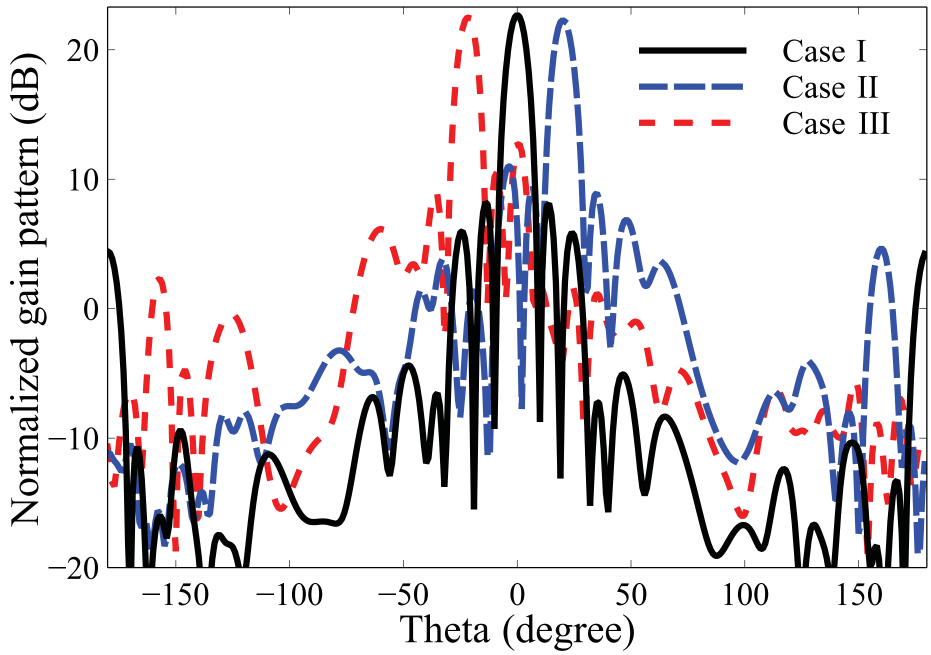

Figure 26: Radiation pattern for different beam scanning cases of Table 2.

antenna elements consisting of subarrays, varactors, and phase shifters to the optimized feeding network. The varactors are simulated precisely using the non-ideal equivalent circuit while the phase shifters can be easily considered by adding specific lengths to the delay-line segments on each row of the power divider. Three different scanning cases are presented in Table 2 and the results of radiation patterns are shown in Fig. 26. The radiation patterns peak gain is 22.8 dBi at broadside while its main beam direction can change with the applied reactance change as anticipated. Clearly, the grating lobes that appear in the conventional array patterns have disappeared by applying the interleaved arrangement. The main beam for other scanning angles is pointed in the desired directions, and side lobe maintains 13 dB below the main beam. The lower SLL can be achieved by changing the power distributions of the driven elements through the feeding network. Moreover, to reduce the high back radiation, a solid conducting reflector can be placed at the back of the antenna below the ground plane. The simulation results show that the scanning performance of the ESPAR is continuous as we scan around the broadside direction without degrading the pattern integrity.

4.5 Comparison to Conventional Beam Steerable Antenna Arrays

Phased array antennas and beam steerable reflectarray antennas are the conventional solutions for applications requiring highly directive and steerable radiation patterns. In this section, the proposed antenna will be compared to these conventional beam steerable antenna arrays. This thorough and detailed comparison will provide enhanced insight to the ESPAR and the advantages of our approach.

4.5.1 Comparison with Conventional Phased Array Antenna

The ESPAR performance compared to conventional array, offers the following potential advantages:

(1) The number of phase shifters is considerably reduced by a factor equal to the number of the subarrays comparing to the conventional array that requires a phase shifter for each element. For example, the presented array requires 48 phase shifters as compared to a conventional array of a similar number of radiating elements, which requires 240 phase shifters. The number of phase shifters is reduced by 80%.

2) These arrays also have a better aperture efficiency over the conventional arrays due to two factors. First, parasitic DRAs in a subarray arrangement reduces the interconnecting lines, which results in less ohmic heat loss as well as less unwanted radiation. Second, scan loss of the conventional array can be reduced significantly in the ESPAR. The element radiation pattern often has its maximum peak in the boresight direction while its gain decreases off the broadside. For the conventional phased array, the shape of the element pattern remains unchanged as the array is scanning, which is controlled by the array factor. Therefore, a scan loss due to the array factor as well as the element pattern is introduced. However, in ESPAR, the element pattern (ESPAR sub-array) is not constant during the beam scanning, and it can be rotated towards the desired main beam direction, which

Table 3: Comparison of the proposed ESPAR with beam steerable reflectarrays.

	Proposed ESPAR	Ref [55]	Ref [56]	Ref [57]	Ref [58]
Tuning Technology	Varactor diode	Mechanical	PIN diode	Varactor diode	MEMS switch
Structure type	Planar	Bulky	Bulky	Bulky	Bulky
Centre Frequency	10.5 GHz	3.1 GHz	10.4 GHz	5.4 GHz	26.5 GHz
Aperture Size	$7\lambda \times 9.4\lambda$	$3.8\lambda \times 3.8\lambda$	$9.9\lambda \times 9.9\lambda$	$3.2\lambda \times 3.9\lambda$	$5.9\lambda \times 5.6\lambda$
Gain	22.4 dBi	18 dBi	25.6 dBi	12.5 dBi	11.42 dBi
Gain FBW	5.7 %	Not Given	10 %	3.6 %	3.77 %
Efficiency	56 %	69 %	66 %	14%	7.85 %
Aperture Efficiency	20.4%	34.34%	29.1%	11.1%	3.4 %
Beam steering range	$\pm 25°$	Up to 10.5°	0° or $\pm 5°$	Up to 40°	0 or +40°
Beam steering type	Continuous	Continuous	Discrete	Continuous	Discrete

eliminates the scan loss introduced in the conventional phased array.

4.5.2 Comparison to Beam Steerable Reflectarray

A reflectarray consists of a planar array of elements laid into a lattice configuration that directs the incident electromagnetic field radiated from a feed antenna to the desired direction. In the literature, there are several configurations proposed for the dynamic control of electromagnetic waves in RAs such as employing mechanical structures [55], PIN diodes [56], varactor diodes [57], and MEMS switches [58]. These configurations differ in many terms such as maturity, availability, performance, biasing complexity, and the suitability for a given frequency range [59]. A photograph of one reflectarray prototype is illustrated in Fig. 27. A detailed review of reconfiguration technologies is beyond the scope of this section, and therefore it is important to select the notable beam steerable reflectarrays that can serve as benchmarks to compare with the proposed large ESPAR.

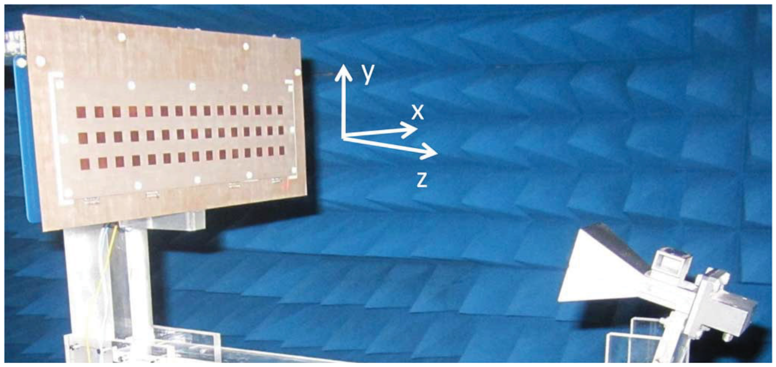

Figure 27: Photograph of one reflectarray protoype. (Venneri et al. [62], © IEEE 2013)

Table 3 is a comparison of the key performance parameters of these steerable beam arrays.

The ESPAR and RA both suffer from the main shortcoming of their narrow gain bandwidth. The feeding network and narrow bandwidth of varactors diode limit the ESPAR gain bandwidth while the element bandwidth and spatial phase error constrain the RA gain bandwidth. As it can be seen in Table 3, the range of fractional gain bandwidth of the beam steerable RA and proposed ESPAR are relatively similar. However, it is important to note that the bandwidth of RA can be significantly increased with different techniques up to 30% [60] and the ESPAR bandwidth can be improved by techniques like non-foster parasitic loads [61].

The radiation efficiency of ESPAR due to the losses of the feeding network, phase shifters, varactors and DC biasing lines is in the reasonable range of 56%. On the other side, in the RA, the feeding mechanism eliminates the losses of the feeding network used in ESPAR. However, for the beam steerable RA, the DC biasing of the control elements becomes a sever issue. In contrast to the ESPAR that one DC biasing line can be used for all the subarrays, in RA each cell of the array must be controlled independently which introduces higher losses in the structure [59]. It is important to note that this issue is not seen in beam steerable RA employing mechanical technology, resulting in a 69% radiation efficiency. However, the mechanical steering is slow and requires a large space to allow for the physical rotation of the antenna. Aperture efficiency (ϵ_{ap}) is another important factor to compare the ESPAR with RAs. Here we calculated the aperture efficenies of the reported references based on this equation:

$$\epsilon_{ap} = \frac{\lambda^2}{4\pi A_p} G \tag{25}$$

where G is the antenna gain and A_p is the physical antenna size. The aperture efficiency of the proposed ESPAR is about 20.4%, which is higher than [57] and [58], and it is lower than [58] and [56]. It is important to note that the aperture efficiency of ESPAR can also be improved with the more precise design of a feeding network and using different element types such as coupled slot cavity-backed slot which will allow high-magnitude coupling and high aperture efficiency [56]. The reported range of the beam steering angle of the RAs is about 10.5° to 40° for continuous and 5° to 40° for the discrete beam scanning type. In ESPAR the continuous beam steering range is about ±25° which is comparable to an RA with a distinct advantage of a 2-D beam scanning. For example, the RA reported in [55] is capable of beam steering in only the H-plane, while in the proposed ESPAR beam scanning can be achieved in at least two main planes (E and H-plane). It is noted that due to the magnitude tapering across the ESPAR, the beam scanning is obtained with an inherently low sidelobe level. One significant advantage of the ESPAR over the RA is its planar structure. In a reflectarray antenna, the feeds destroy the planar nature of the RA antenna while an ESPAR keeps its planar configuration. Therefore, the ESPAR concept will be much cheaper, simpler and planar as compared to the reflectarray that requires the feed to be in front of the array which makes it bulky.

4.6 Fabrication and Measurements

To verify the large ESPAR concept, a prototype was fabricated and measured experimentally with the aperture size of 201 mm × 270 mm. In this fabrication, we specifically consider radiation in the boresight direction for the large ESPAR. A photo of the fabricated antenna prototype is shown in Fig. 28. Two layers of the array including the radiation

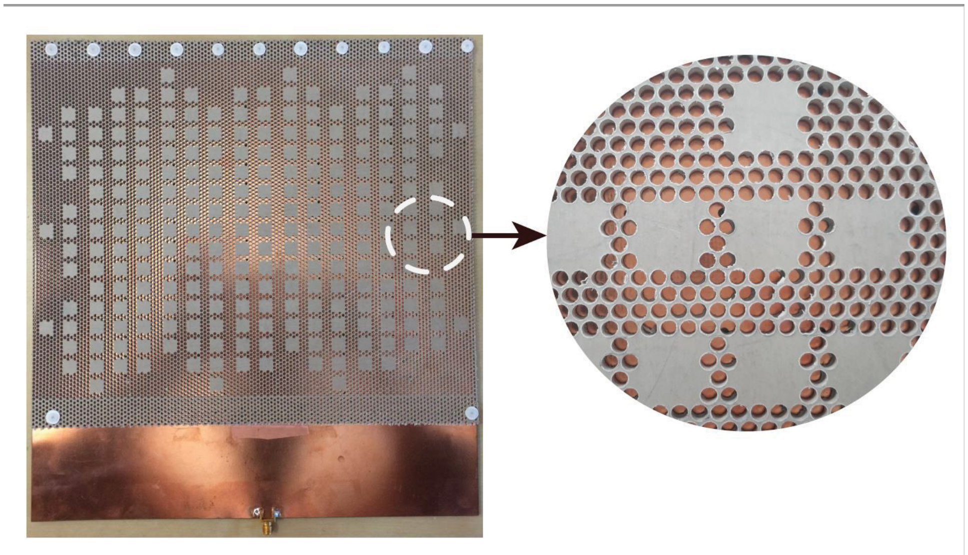

(a)

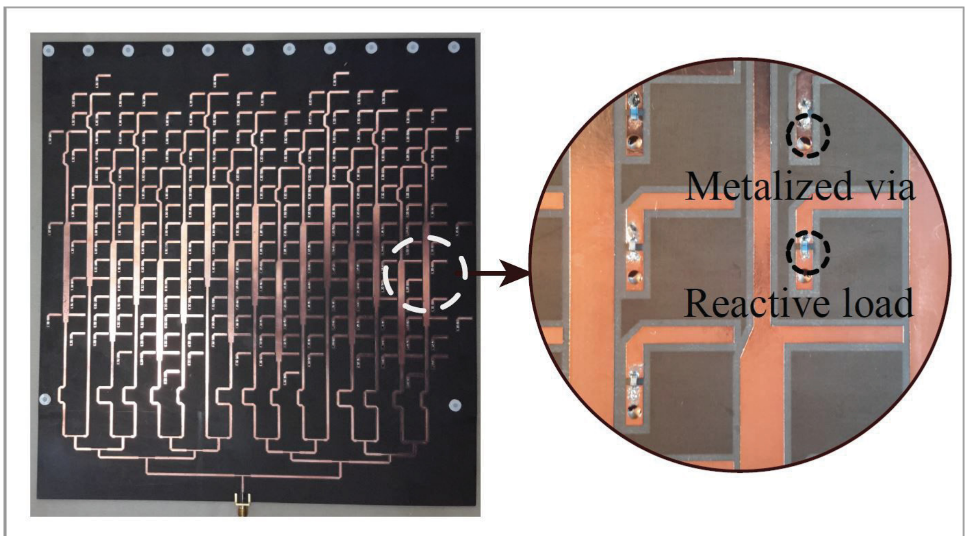

(b)

Figure 28: Photographs of the fabricated prototype and its radiation pattern measurement setup. (a) Top view. (b) Bottom view.

and feeding layer are fabricated, screwing together to build the designed structure. The radiation layer is first constructed from a single dielectric Rogers Duroid 6010 sheet by perforating lattice of holes using a conventional computer-controlled milling machine. The lumped elements are Coilcraft 0402HP-1N0XJLW and Mouser 581-600L0R2AT, which are manually mounted and soldered. To terminate the lumped element to the ground plane, metalized vias are placed in the feeding layer as shown in Fig. 28(b).

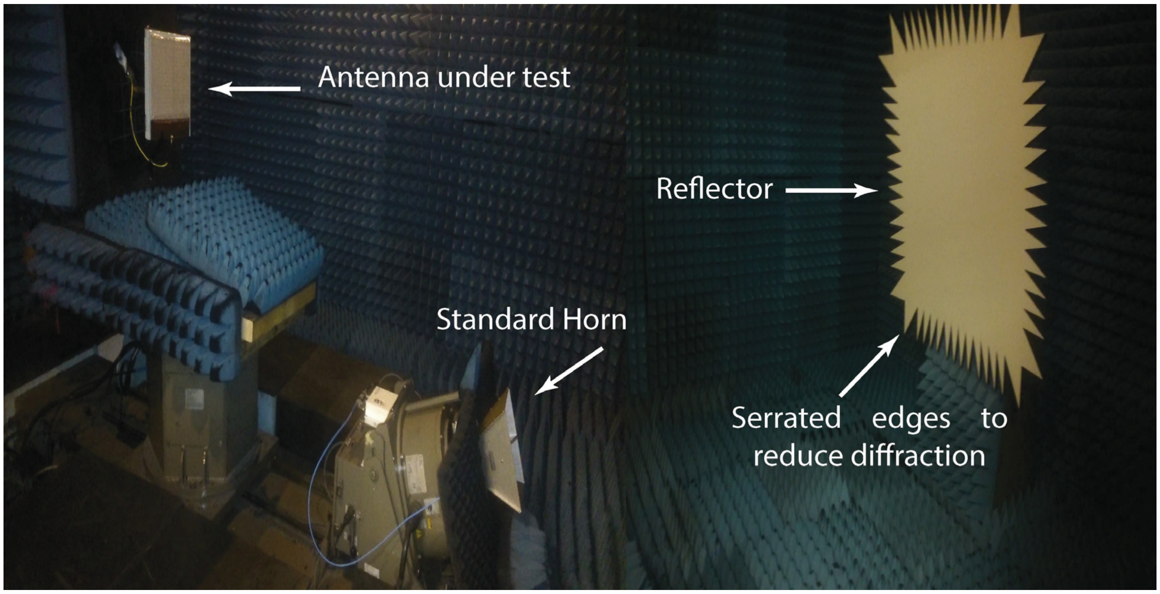

Figure 29: Photograph of radiation pattern measurement setup in a compact antenna test room (CATR).

An Agilent N5227A PNA network analyzer was employed to perform the amplitude and phase measurements of the reflection coefficient, S11. The simulated and measured results for the reflection coefficient of the proposed antenna are shown in Fig. 30(a). It is observed that the measured reflection coefficient is below –10 dB from 9.6 to 11 GHz, which is close to the simulated result. The measured realized gain is shown in Fig. 30(a) with a 3-dB bandwidth of 5.76% (10.1 GHz to 10.7 GHz). Far field characteristics of the fabricated antennas are also measured using the compact antenna test range (CATR) facilities at the Poly-Grames Research Center, Ecole Polytechnique de Montreal, Canada. The CATR can produce a nearly uniform plane wave in a compact range by using a horn antenna and a reflector as shown in Fig 29. It is worth mentioning that to reduce the diffraction, the edges of the reflector are serrated. The simulated and measured radiation patterns at 10.5 GHz for both E- and H-plane are shown in Fig. 30(b) and (c), respectively. The measured and simulated radiation patterns are in good agreement and showing broadside radiation and symmetric radiation patterns. Moreover, the cross-polarization of the antenna in the principal planes is better than -26 dB. The realized gain is 22.4 dBi at 10.5 GHz. The slight discrepancy between the simulation and measurement are due to the possible

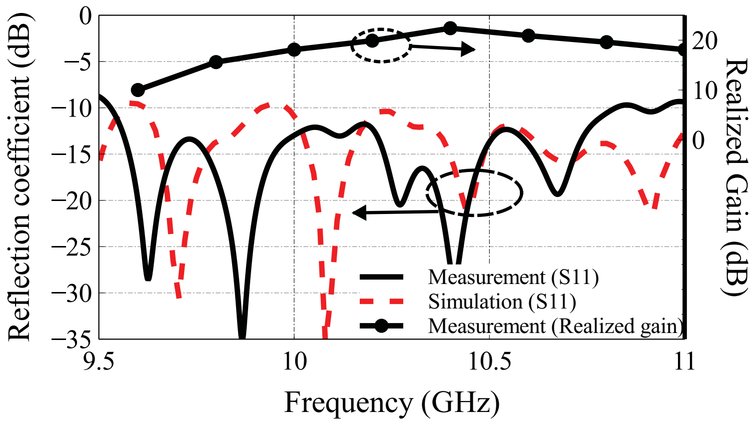

(a)

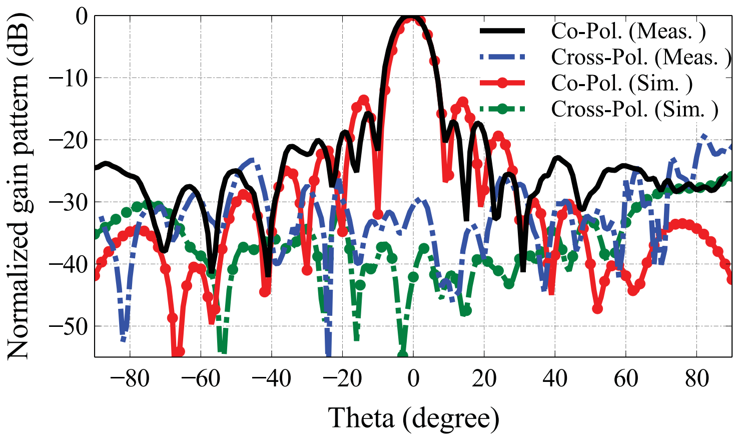

(b)

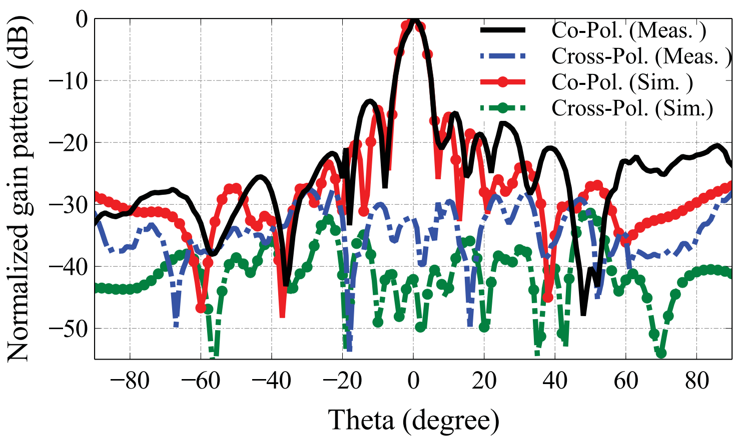

(c)

Figure 30: Simulated and measured scattering parameter, realized gain, and radiation patterns of the proposed ESPAR. (a) Reflection coefficient and realized gain. (b) H-plane radiation pattern at 10.5 GHz. (c) E-plane radiation pattern at 10.5 GHz.

presence of air gap between the radiating dielectric slab and the ground plane as well as possible misalignment of the slots with the DR elements.

4.7 Summary

A large electrically-steerable passive array radiator (ESPAR) incorporating dielectric resonator antenna elements was designed, fabricated and tested. Several practical issues that are critical in implementing the large ESPAR have been presented. The designed parallel-series feeding network, allows the biasing network to use more space within the allocated area while it reduces the feeding insertion loss. To facilitate the fabrication requirement for the DRA subarrays, a perforation technique has been used, which eliminates the need for aligning and bonding individual DRAs. In addition, to suppress the grating lobes, the subarrays were placed in an interleaved arrangement. The obtained measured results of the fabricated prototype have demonstrated that the proposed design can be successfully implemented to a large ESPAR.

Chapter 5

ESPAR for MIMO and Massive MIMO Applications

5.1 Introduction

Multiple-input multiple-output (MIMO) antenna technology has attracted tremendous interest due to its capabilities in enhancing the data transmission capacity, increasing the reliability, and reducing the multipath fading. Driven by modern generation of wireless devices, new challenges are arising in wireless industries to support the exponential increase of the data traffic and the corresponding network loads [63]. Recently, Massive MIMO has been proposed as one of the key technologies to address these challenges. The basic idea of massive MIMO is to use large excess of base station antennas to simultaneously serve many terminals in the same time-frequency resource [64].

In this chapter, the performance of the DRA-ESPAR is investigated in MIMO and massive MIMO systems. To this end, we have proposed a 4-port MIMO configuration that the mutual coupling of its adjacent ports is reduced by orthogonal placement of subarrays. This structure is well examined in terms of the MIMO figure of merits such as isolation, correlation, mean effective gain and branch power ratio. The performance of the proposed DR-ESPAR is also studied in a massive MIMO configuration which is realized by extending the elements of the proposed MIMO structure. Finally, our study has been accomplished by fabricating and measuring a prototype of the 4-port MIMO configuration.

The chapter is organized as follows. A brief overview of MIMO systems and their important figure of merits are presented in Section 5.2 and Section 5.3, respectively. A literature review on the methods to overcome the issues related to the massive MIMO structures is presented in Section 5.4. The design of proposed antenna as well as the simulation results, are described in Section 5.5. The fabrication details of the proposed antenna and the experimental results are outlined in Section 5.6. Finally, Section 5.7 summarizes the chapter.

5.2 Wireless Communications and MIMO

In order to understand MIMO, some fundamental concepts of wireless communication systems as well as different types of diversity schemes and wireless systems are reviewed in this section.

5.2.1 Diversity

The quality of a signal in wireless communication link might degrade due to fading, co-channel interference, dispersion effects in time and frequency, user mobilities, and path loss effect. Diversity is a common technique to make a communication system robust and reliable even over varying channel conditions. This technique is aimed at providing multiple copies of the same transmitted information at the receiver front end. If these signal replicas are uncorrelated, the fading will have a small probability of occurring simultaneously on all the signal copies. Therefore, the multiple versions of signals can be combined at the receiver to make an adequate signal to noise ratio (SNR). Diversity schemes can be categorized as follows [65].

Time Diversity

In this scheme, multiple copies of signal are transmitted on different time slots. To provide an uncorrelated channel over those time slots, the delay between signal copies should be greater than the coherent time. By spreading the information on different time, we can minimize the fading effect. This technique requires extra transmission time.

Frequency diversity

In this technique, the signal copies are transmitted across different frequency spectra. To provide an uncorrelated channel for the transmission, frequency bands of the signal copies should be greater than the coherent bandwidth. This technique increases the possibility of having at least one frequency bands that experiences the lowest level of fading. This technique requires extra bandwidth.

Multiuser diversity

Multiuser diversity is obtained by employing adaptive modulation and user scheduling techniques to improve the performance of the wireless communication link. In such system, the transmitter selects best user channel according to the qualities of each channel between the transmitter and each receiver.

Spatial diversity

This technique is aimed at using multiple antenna at transmitted and receiver to improve the quality and reliability of a wireless link. The antennas are sufficiently separated from each which gives rise to a low correlation between the signals at the antennas [65]. Thus, if one antenna is experiencing a deep fade, it is likely that another has a sufficient signal to noise ratio.

Polarization diversity

In this scheme, multiple copies of the same signal are transmitter and received by antennas of different polarization. Since the diffraction and reflection depend on the signal polarization, the different polarized multipath components (horizontal or vertical), propagate differently in a wireless channel. Therefore, the fading of different polarizations is statistically independent [66]. This technique can significantly reduce the size of the antenna structure since the antennas have low correlation. However, in this technique only two diversity branches horizontally and vertically polarized (or any other two orthogonal polarizations) are possible to generate [66].

Pattern diversity

This technique makes use of antennas having different radiation patterns to generate signal copies. In this technique, each antenna picks up different amplitudes and phases of transmitted or received signal due to the difference in their radiation patterns. Therefore, uncorrelated copies of signal will be generated. Several types of antennas with different radiation patterns can be used for the sake of pattern diversity, such as beam reconfigurable antennas and antenna arrays.

5.2.2 From SISO to MIMO system

The most basic communication system which is referred to as single-input single-output (SISO) system, consists of one single antenna at both transmitter and receiver. Fig. 31(a) illustrates a SISO wireless system. The wireless channel (h_{11}), which is the transfer function between the output of the transmitter, to the input at the receiver is shown as a dashed line. Building a SISO system is affordable due to the few components and lack of complex coding schemes. However, this system is not reliable. As mentioned, a signal that is transmitted over a wireless communication link might be degraded with severe fluctuations in signal level, co-channel interference, distortion in time and frequency, and path loss effect. Therefore, when the only antenna in the receiver experiences the degraded signal, the system is not able to reliably determine the information it has received.

Using multiple antennas at the transmitter or receiver can increase the possibility that at least one of the antennas has a reasonable SNR to be correctly processed [67]. If the multiple antennas are used at the transmitter, the system is referred to as multiple-input

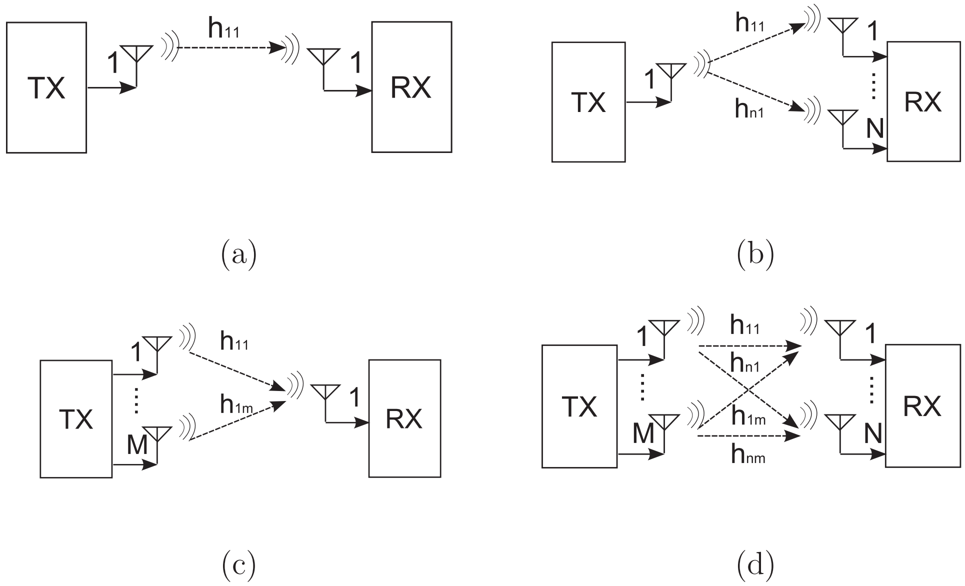

Figure 31: wireless communication systems. (a) A SISO system. (b) A SIMO system. (c) A MISO system. (d) A MIMO system

single-output (MISO), and if they are used at the receiver, the system referred to as single-input multiple-output (SIMO). The MISO and SIMO systems are shown in Fig. 31(b) and Fig. 31(c), respectively.

To collect all the advantages offered by SIMO and MISO systems, we can use multiple antennas at both transmitter and receiver which is referred to as multiple-input multiple-output (MIMO) system. Fig. 31(d) depicts a MIMO system. Recent studies have shown that using MIMO systems could substantially increase the data rate without increasing the transmission power and bandwidth [66]. In a MIMO system with M antennas at transmitter and N antennas at the receiver, the channel can be represented by a $M \times N$

matrix:

$$\begin{bmatrix} h_{11} & h_{12} & h_{13} & \dots & h_{1n} \\ h_{21} & h_{22} & h_{23} & \dots & h_{2n} \\ h_{31} & h_{32} & h_{33} & \dots & h_{3n} \\ \vdots & \vdots & \vdots & \ddots & \vdots \\ h_{n1} & h_{n2} & h_{n3} & \dots & h_{nn} \end{bmatrix} \tag{26}$$

5.3 MIMO antenna Parameters

In the previous section we gave an overview of fundamental concepts of MIMO systems. When we consider a MIMO system, there are parameters that are necessary for evaluating the performance of a MIMO system. In this section we will review the important figure of merits for a MIMO system such as channel capacity, total active reflection coefficient (TARC), isolation, correlation coefficient, mean effective gain (MEG), and branch power ratio.

5.3.1 Channel Capacity

The channel of a communication system can support a diverse spectral efficiency which is dependent on the chosen encoding/decoding scheme [68]. The largest obtainable spectral efficiency which is determined by channel capacity, plays an important role in designing communication systems. Channel capacity concept was first defined by Shannon in 2001 [69]. The channel capacity for a SISO scenario in an additive white Gaussian noise (AWGN) environment can be found from:

$$C = W log_2(1 + \frac{\bar{P}}{N_0 W}) \tag{27}$$

where W is the bandwidth in Hertz, $\bar{P}$ is the average received power in Watts, N_0 is the noise power spectral density in W/Hz, and P/N_0W represents the received SNR [67]. Note that the channel capacity is determined in unit of bits/s.

This equation can be further improved by using the channel matrix (h_{SISO}) as:

$$C = \log_2(|\frac{1 + h_{SISO}^2 P}{N_0}|) \tag{28}$$

Similarly, for MIMO scenario with M antenna at transmitter and N antenna at receiver, the channel capacity can be determined by:

$$C = \log_2(\det(\frac{I + P(HRH^H)}{N_0})) \tag{29}$$

Where, P here is the average transmitted power per antenna in Watts, I is the identity matrix, R is the covariance matrix, and the $\{.\}^H$ is the Hermitian operator. It is worth mentioning that the channel capacity of MIMO is $M \times N$ times larger than the SISO capacity.

5.3.2 TARC

The scattering matrix is an important figure of merits which describes the bandwidth of an antenna. However, to study the efficiency and bandwidth of a multiport antenna system like MIMO, a parameter referred to as total active reflection coefficient (TARC) need to be considered. If we assume the summation of the available power at all excitation ports as incident power (P_{in}), radiated power as transferred power (P_{rad}), and the difference between these two as reflected power (P_{refl}), then the TARC is determined by [70]:

$$\Gamma_a^t = \sqrt{(\frac{P_{in} - P_{rad}}{P_{in}})} \tag{30}$$

For a lossless N-port antenna system, the TARC can be calculated as:

$$\Gamma_a^t = \frac{\sum\limits_{i=1}^{N}|b_i^2|}{\sum\limits_{i=1}^{N}|a_i^2|} \tag{31}$$

where b_i and a_i are the incident and reflected signal vectors with randomly phased elements, respectively. Thus, TARC is determined by applying different combinations of incident signals to each port.

For a 2×2 MIMO system, the TARC can be determined by [71]:

$$\Gamma_a^t = \frac{\sqrt{\left(|(s_{11} + s_{12}e^{j\theta})|^2 + |(s_{21} + s_{22}e^{j\theta})|^2\right)}}{\sqrt{2}} \tag{32}$$

where θ is the excitation phase difference between ports.

It is worth noting that the scattering matrix of an N port antenna has $N \times N$ elements and tracking all these curves for a multi-port antenna is difficult. By using TARC we can compress all these curves into one curve that has all the information of the S-parameters [72]. Moreover, TARC includes the effects of feeding phase to the antenna ports. TARC has a value between 0 and 1 and is a real number, since the phase reference plane does not have any physical meaning for a multiport antenna [70]. It is noted that TARC meaning for an array is like return loss meaning for a single antenna. For instance, for a lossless antenna, if 90% of the incident power radiates and the rest is reflected back to the antenna, TARC is equal to –10 dB [70].

5.3.3 Isolation

Isolation is a measure of the power that is coupled between the adjacent radiators within the multi-antenna systems [73]. In isolation analysis, the multi antenna system is considered as a multi-port network, and the isolation between the ith and jth antenna is defined as 10 log$(1/|S_{ij}|^2)$ [74]. In most of the antenna applications, the lowest value of isolation is desired. If the isolation between two antennas has a low value, it means that the two antennas are strongly coupled and most of the transmitted signal of the antenna will not be radiated, but rather received by the other antenna. Therefore, a reduction will be appeared in the radiation efficiency due to the dissipation of power in the coupled antenna [65]. The amount of isolation between two antennas depends primarily on the [37]:

(1) radiation characteristics of each

(2) relative separation between them

(3) relative orientation of each

There are numerous techniques in the literature for isolation enhancement that will be discussed in Section 5.4.

5.3.4 Correlation Coefficient

Correlation coefficient is a typical quality used to evaluate the isolation or correlation of communication channels. It considered the far field radiation of the antennas and determines how much their patterns are correlated to each other. The square of the correlation coefficient is known as envelope correlation coefficient which in a uniform multipath environment can be calculated as [72]:

$$\rho_e = \frac{\left| \iint_{4\pi} \left[\vec{F_1}(\theta,\phi) * \vec{F_2}(\theta,\phi)\right] d\Omega\right|^2}{\iint_{4\pi} \left|\vec{F_1}(\theta,\phi)\right|^2 d\Omega \iint_{4\pi} \left|\vec{F_2}(\theta,\phi)\right|^2 d\Omega} \tag{33}$$

Where $\vec{F_i}(\theta,\phi)$ is the far field radiation pattern of the antennas. In [75] a simple derivation is suggested to find the envelope correlation coefficient (ECC) based on the scattering parameter as:

$$\rho_{eij} = \left| \frac{|s_{ii}^* sij + s_{ji}^* s_{jj}}{\left|\left(1-|s_{ii}^2|-|s_{ji}^2|\right)\left(1-|s_{jj}|^2-|s_{ij}|^2\right)\right|^{1/2}} \right|^2 \tag{34}$$

This equation is applicable for antennas with high efficiencies. The ECC ranges form zero (no correlation, best MIMO gain) to one (identical pattern, no MIMO gain). Based on [76], the acceptable range of ECC for a 4G wireless system is 0.3 and the upper value is 0.5.

It is also worth noting that correlation coefficient is not just an antenna related parameter and it also depends on local channel. In other word some antenna may have high correlation in one environment and low correlation in another.

5.3.5 Mean Effective Gain

The stand-alone gain of the antenna that is measured inside an anechoic chamber cannot effectively describe the antenna performance in an environment which consist random multipaths due to the scattering, reflection and diffraction of electromagnetic fields. The mean effective gain (MEG) is an important measure of a mobile antenna that considers the effect of environment. The concept of MEG was introduced by Taga [77], who defined it as a comparison of the mean power received by a mobile antenna under test along a route in the propagation channel of interest by the sum of the average powers received by reference antennas in the same environment and the same route. Therefore, the measured MEG contains the mutual relation between the antenna pattern and the propagation characteristics along the route, and varies depending on the measuring route [77]. A theoretical method for analyzing the MEG which is proposed in [77], is based on the measured 3-D radiation pattern of the antennas which is difficult in practice. Therefore, to simplify the calculation of MEG, a two-dimensional model was proposed in [78] which the incoming radio wave distributions are concentrated in the horizontal plane:

$$G_e = \int_0^{2\pi} [\frac{XPR}{1+XPR} G_\theta(\frac{\pi}{2},\varphi) P_\theta(\frac{\pi}{2},\varphi) + \frac{1+XPR}{XPR} G_\varphi(\frac{\pi}{2},\varphi) P_\varphi(\frac{\pi}{2},\varphi)] d\varphi \qquad (35)$$

where $G_\theta(\frac{\pi}{2})$ and $G_\varphi(\frac{\pi}{2})$ are the θ and ϕ components of the antenna power gain pattern, respectively, and $P_\theta(\frac{\pi}{2},\varphi)$ and $P_\varphi(\frac{\pi}{2},\varphi)$ are the θ and ϕ components of the angular density functions of incoming radio waves, respectively.

5.4 Massive MIMO

The basic idea of massive MIMO is to use a large excess of base station antennas to simultaneously serve many terminals in the same time-frequency resource [64]. The massive MIMO technology offers more advantages as the number of antennas increases. However, for feeding each individual antenna, one radio frequency chain is required that can increase the power consumption, complexity and the total cost of the structure. Moreover, to obtain decorrelated channels and to reduce mutual coupling, the antennas should be spaced sufficiently far from each other and that imposes increased physical dimensions. Therefore, to make massive MIMO a reality, the size and cost issues should be addressed and studied.

5.4.1 The Search for a Good Massive MIMO Antenna

Many studies on the compactness methods for MIMO systems such as multimode antennas [79], decoupling networks [80,81] and asymmetrical or orthogonal antenna placement [82–85], can similarly be used in massive MIMO applications. For instance, based on the multimode antenna elements, a compact massive MIMO is proposed in [86] as shown in Fig. 32. In this design, by exciting different characteristic modes, a four-port antenna element is obtained and developed in an 11×11 element array with 484 antenna ports. Therefore, a size reduction of 54% compared to a generic multi element antenna based on crossed dipoles is obtained without using additional matching and decoupling networks. The authors in [87] have presented a compact massive MIMO antenna using the orthogonal placement of two stacked patch antennas. The proposed array is composed of 144 ports with a low mutual coupling within the operating bandwidth of 3.65 GHz to 3.81 GHz. The photograph of the antenna prototype is shown in Fig. 33.

Extensive research have been conducted on the signal processing techniques to reduce the number of RF chain such as antenna selection [88], analog antenna combining [89],

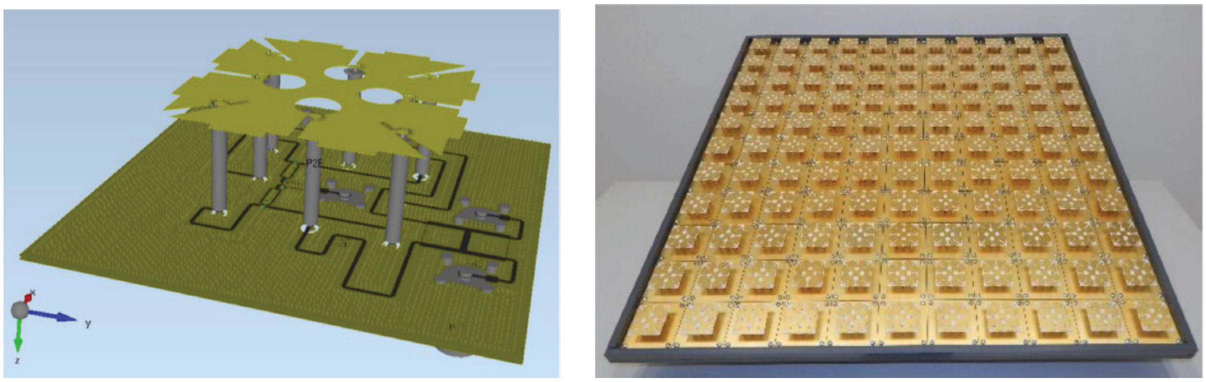

(a) (b)

Figure 32: A compact ultra-wideband multielement antenna (MEA) for massive MIMO indoor base stations. (a) Multimode antenna element and its feed network. (b) realized Prototype of an 11 array of multimode elements having 484 antenna ports (Manteuffel et al. [86], ©IEEE 2016).

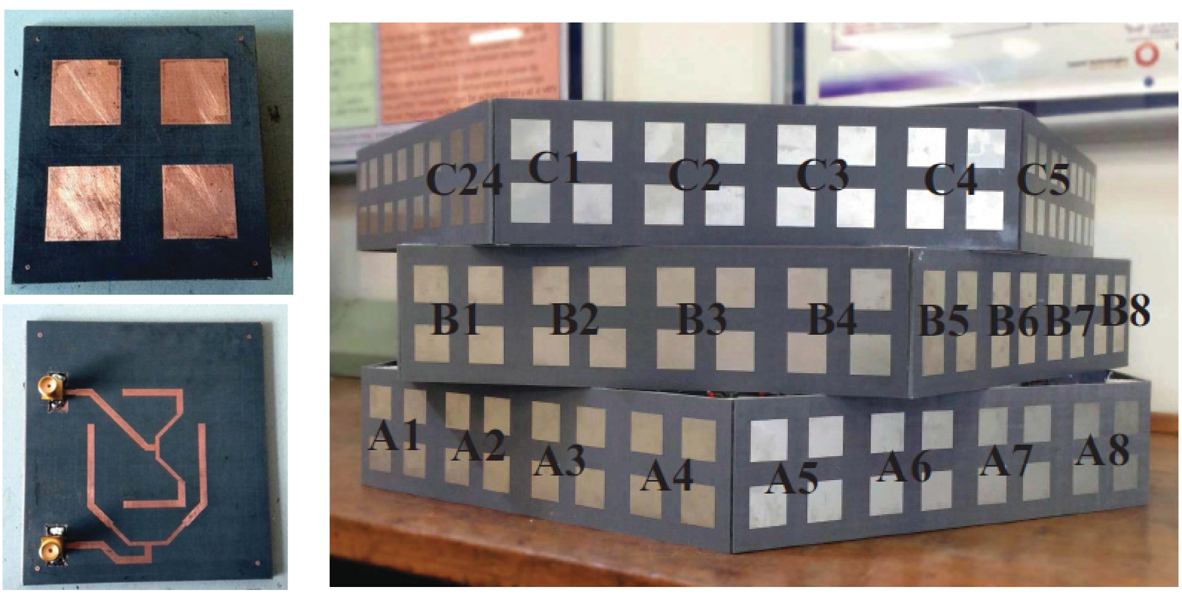

(a) (b)

Figure 33: Stacked patch antenna with dual-polarization and low mutual coupling for massive MIMO applications. (a) The front and back view of th prototype of the single antenna unit. (b) The configuration of three level Turning Torso antenna array (Gao et al. [87], ©IEEE 2016).

time-division multiplexing [90], code-modulated path-sharing [91], and code division multiplexing [92]. However, there has been less attention in the literature toward the antenna solution for reducing the number of RF chains in massive MIMO applications.

Recently, the electrical steerable parasitic array radiator (ESPAR) has been proposed as an effective method to simultaneously reduce the number of RF chains and size of the MIMO systems [93–95]. It consists of one driven antenna which is surrounded by parasitic elements loaded with tunable reactive loads. The parasitic radiators can obtain their energy from the driven antenna through the mutual coupling, and the tunable reactive loads create the necessary phase shift for beam scanning. Therefore, different from conventional MIMO that each antenna need to be fed by an independent voltage source, in ESPAR, only the driven elements are fed which can significantly reduce the number of RF chains as well as the complexity of the feeding networks [96]. Also, in ESPAR, mutual coupling constraint turns to be an advantage as it is used as a design tool to form the desired signals, resulting in a more compact size. Furthermore, by controlling the tunable loads at each parasitic antenna element, different radiation patterns can be formed which can significantly improve the performance of a MIMO antenna system operating in a changing environment.

5.5 Design Procedure

Our study on the performance of the DRA-ESPAR in MIMO and massive MIMO applications can be explained in three steps as shown in Fig. 34. As a first step, a DRA-ESPAR subarray is designed which consist of one driven antenna, surrounded by parasitic elements that are loaded with tunable reactive loads. The parasitic elements obtain their energy from the driven antenna through the mutual coupling, and the tunable reactive loads create the necessary phase shift for beam scanning. The details of the subarray design with the simulated results will be discussed in Section 5.6.

The second step aims at designing a 4-port MIMO antenna by orthogonal placement of the proposed DRA-ESPAR subarrays. In this arrangement, each port has orthogonal polarization with its adjacent port which results in a high isolation with a compact configuration. It is noted that the high isolation between ports leads to a low antenna correlation characteristic which is an important figure of merit in MIMO antennas [73]. Section 5.5 will discuss the performance of the proposed MIMO antenna.

The last step is to build a massive MIMO structure by expanding the 4-port MIMO antenna. This can be done by adding similar polarized subarrays to each port of the MIMO antenna structure. These subarrays are placed in an interleaved arrangement which can surpass the grating lobes with better scanning capabilities in all azimuthal directions. The proposed massive MIMO structure will be discussed in Section 5.8.

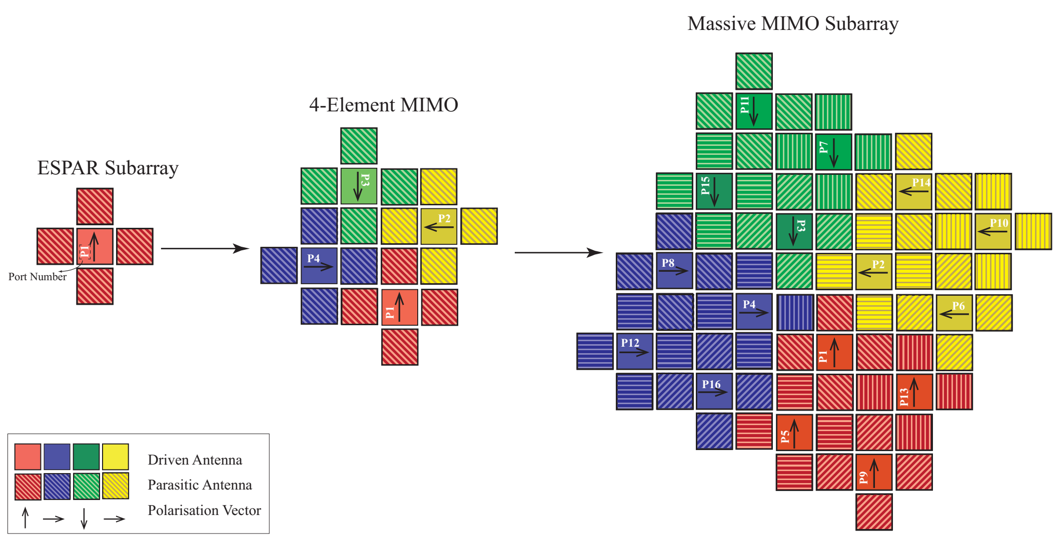

Figure 34: The steps of our studies on the performance of DRA-ESPAR in MIMO and massive MIMO applications. First a DRA-ESPAR subarray is designed which consist of one driven antenna, surrounded by parasitic elements that are loaded with tunable reactive loads. Then, by orthogonal placement of this subarray, a 4-port MIMO structure can be formed. Finally, by expanding the MIMO structure, the massive MIMO structure can be designed.

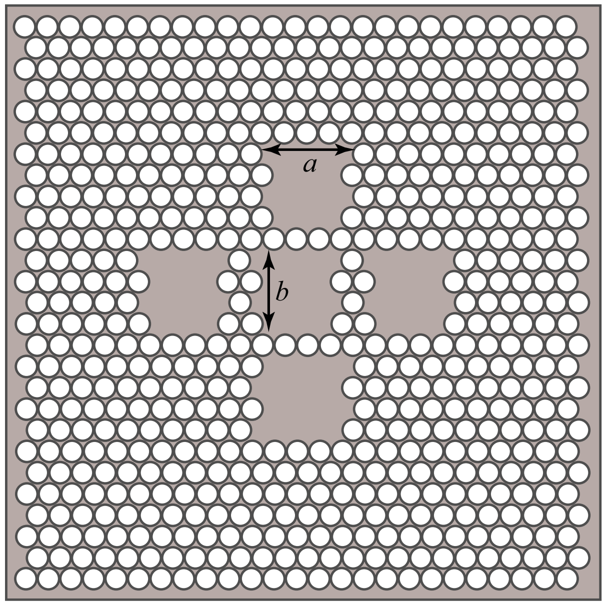

(a)

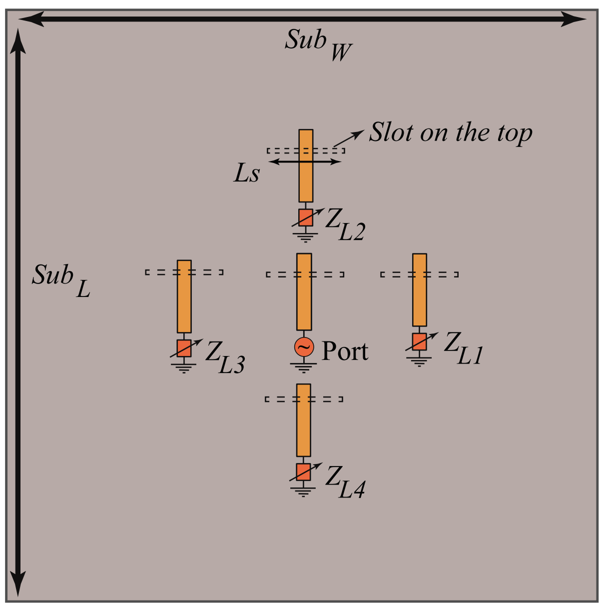

(b)

Figure 35: Proposed ESPAR subarray fed by aperture coupled lines at the back of the structure. (a) Top view of the subarray. (b) bottom view of the subarray. ($sub_l = sub_w =$ 135 mm, $slot_l = 9.5$ mm, $slot_w = 1$ mm, $Ls = 4.5$ mm, and $a = b = 15$ mm).

5.6 Espar Subarray

Fig. 35 shows the basic geometry of the proposed DRA-ESPAR subarray which was previously studied in Chapter 4. We have used DRAs as the main radiator due to their

Table 4: Scanning Schemes Radiation Performance (All Values Given at 4 GHz)

Scanning Scheme	1	2	3
$\phi-$plane	0°	0°	90°
Scan Angle (θ)	0°	30°	$-25°$
Z_{L1} (pF)	3.5	4.5	0.7
Z_{L2} (pF)	4.5	1	1
Z_{L3} (pF)	4.5	1.5	3.5
Z_{L4} (pF)	4.5	1	1.5
S_{11} (dB)	-21	-15	-19
Peak Gain (dB)	7	6.7	6.7

exceptional features, such as high radiation efficiency and wide impedance bandwidth [97]. The DRAs are made of a dielectric with a thickness of 7.5 mm and relative permittivity of 10.2, placed above an aperture-coupled feed substrate of Rogers RT6002 (ϵ_r =2.94, tan δ = 0.0012) with a thickness of 0.508 mm. The aperture-coupled feeding technique is chosen because it provides ample space for antenna elements and feeding bias network. Moreover, in this technique, the tunable reactive loads and their biasing network are placed in a different layer than the radiating layer, which can minimize their effect on the antenna radiation characteristics [16, 98]. We have used the perforation technique to fabricate DRAs from a single dielectric sheet. By this means, we can eliminate the difficulties in aligning and bonding the individual elements of the DRAs [47, 99].

The center DRA is the driven antenna which is coupled to parasitic elements in its E- and H-plane. The parasitic elements are excited by the driven antenna through mutual coupling. The required phase shifts for beam scanning are obtained by changing the reactance of the varactors loading the parasitic elements. To determine the proper reactive loads for a desired beam scanning direction, a network circuit analysis described in [98] has been performed and the reactive load values for three different beam scanning schemes are presented in Table 4. These schemes are chosen to investigate the scanning performance in various $\phi-$planes with positive and negative scan angle (θ) directions ($-25°$ to $30°$).

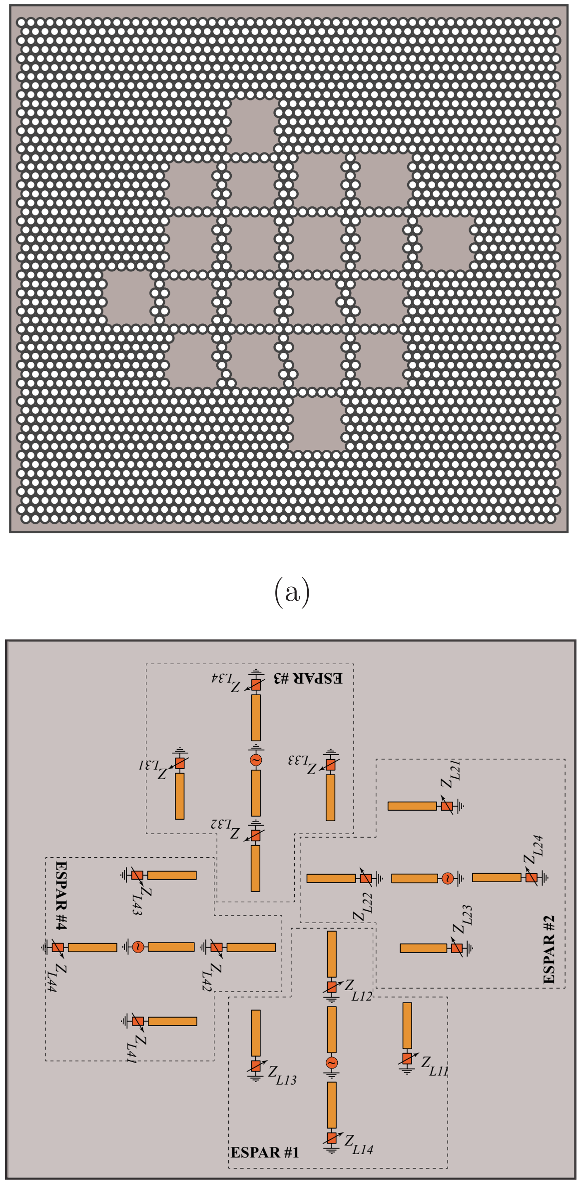

(a)

(b)

Figure 36: The proposed MIMO structure. It consists of four perforated subarrays which are rotated 90 degrees with respect to their adjacent subarrays. (a) Top layer. (b) Bottom layer. The reactive load for each element is shown with Zl_{ij}, where i and j are the number of passive elements and ports, respectively.

The simulated results of different beam scanning schemes are also presented in Table 4. As expected, the beam scanning is obtained by changing the reactive loads. It is observed that for all scanning beams the reflection coefficient is maintained below –15 dB at the

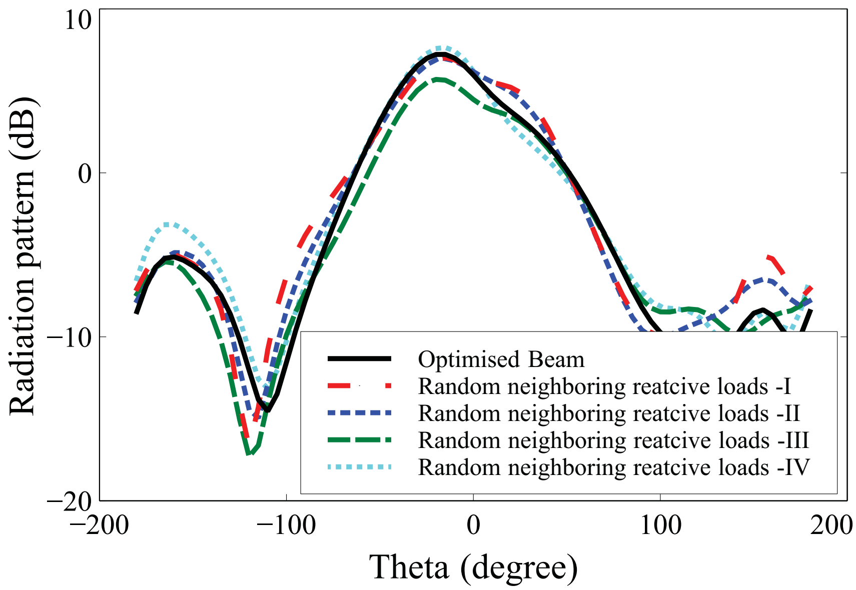

Figure 37: Simulated radiation pattern of the proposed MIMO configuration, showing the undesirable effect of neighboring parasitic elements. In the simulation setup Port #1 is excited for the direction of $\theta = -20°$ in $\phi = 0°$ plane while the remained ports are terminated with 50 Ω load and their reactive load are changed randomly.

operating frequency. Moreover, the gain variation is 0.3 dB across the scanning range, and the scanning is achieved without degrading the antenna performance.

5.7 MIMO Structure

5.7.1 Design and Theory

As discussed above, ESPAR is a good candidate for MIMO applications due to its beam reconfigurable capability which results in increasing the transmission capacity and reliability of the system. To investigate the potentials of the proposed DRA-ESPAR for MIMO applications, the arrangement shown in Fig. 36 is proposed. This structure consists of four perforated DRA-ESPAR which are rotated 90 degrees with respect to their adjacent subarrays. This makes the neighboring ports have orthogonal polarizations which can significantly increase their isolation. Moreover, with this arrangement, the antenna is able to simultaneously exploit polarization and pattern diversity. The ESPAR subarrays are

Table 5: Scanning Schemes Radiation Performances (Reactive loads are in pico Farad and the frequency is 4 GHz)

	ESPAR No.1				ESPAR No.2				ESPAR No.3				ESPAR No.4			
Scanning Schemes	Z_{L1}	Z_{L2}	Z_{L3}	Z_{L4}	Z_{L1}	Z_{L2}	Z_{L3}	Z_{L4}	Z_{L1}	Z_{L2}	Z_{L3}	Z_{L4}	Z_{L1}	Z_{L2}	Z_{L3}	Z_{L4}
Case I	3	4.2	4.5	4.5	4	4.5	3.5	4	1.5	1	1.5	4.5	3	4	4.5	4.5
Case II	3	4.5	4.2	4.2	3.5	1	0.7	1.5	1.5	1.5	1	4.5	3	3.5	4	4
Case III	4.5	1	1.5	1	4	4	3.5	3.5	1	1.5	1	4.5	3.5	3	4.5	4
Case IV	1.5	1	1	4.5	3.5	4	4	3	1.5	1	1	4.5	4	3.5	4	3.5

numbered from 1 to 4 as shown in Fig. 36. The reactive loads are numbered as Zl_{ij}, where i and j are the number of passive elements and ports, respectively.

It should be noted that the mutual coupling still exists between ports and should be considered in finding the proper reactive loads for a desired direction.

To clarify the mutual coupling effect, simulations have been performed and the results are shown in Figure 44. In the simulation setup, ESPAR no. 1 is excited by a 50 Ω lumped port and its reactive loads are fixed for the direction of $\theta = -20°$ in the $\phi = 0°$ plane. The remaining ESPARs are terminated with 50 Ω loads and their reactive loads are randomly changed accordingly. The simulated radiation patterns for four random cases are depicted in Fig. 37. It is observed that in certain situations the parasitic elements of the neighboring antenna may cause undesirable interference in the radiation pattern. For instance, the gain of Case I, has dropped 0.5 dB and the beam is slightly tilted. The worst one is Case IV which the gain has dropped 1.5 dB. Therefore the reactive loads should be optimized precisely by considering the mutual coupling effect of the neighboring elements for each beam scanning direction.

Each subarray can independently steer the beam toward different directions. Thus, there are many possible directions that can be achieved. In order to investigate the performance of the antenna for a MIMO system, 4 different beam scanning combinations have been introduced in Table 5 and their simulated radiation patterns are shown in Fig. 38.

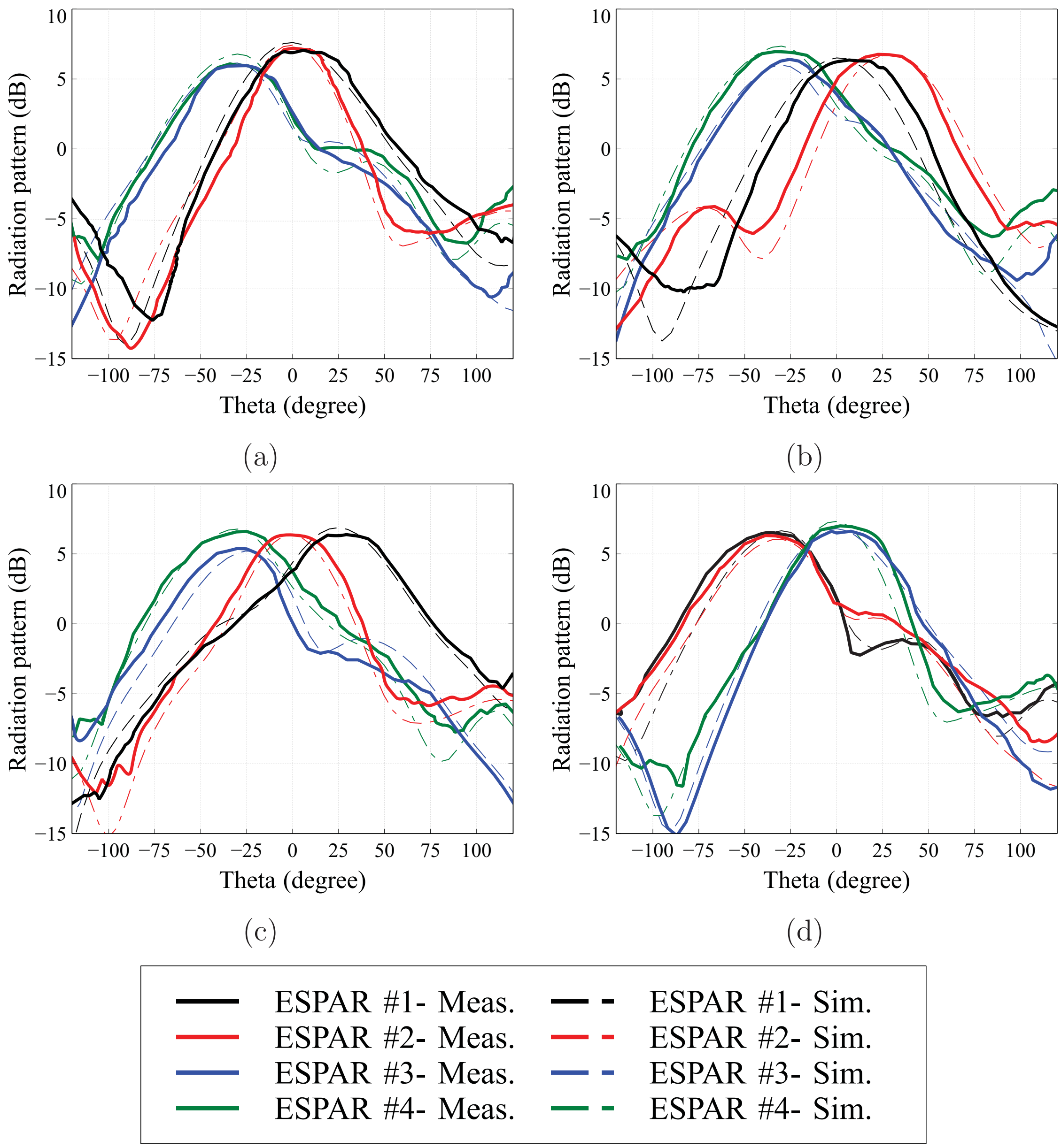

Figure 38: Simulated and measured radiation pattern of different beam scanning schemes of the proposed MIMO structure. (a) Case I. (b) Case II. (c) Case III. (d) Case IV.

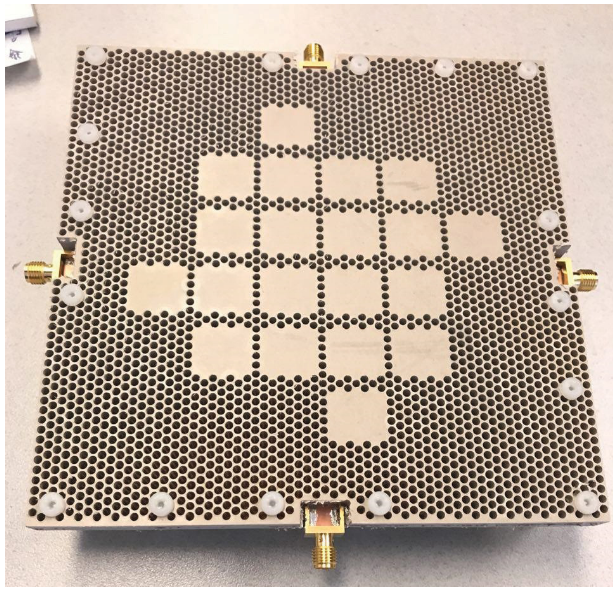

(a)

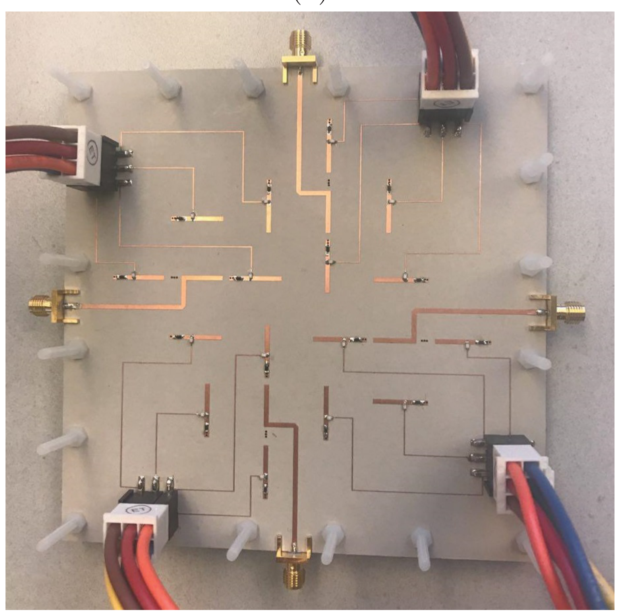

(b)

Figure 39: Photograph of the proposed ESPAR for MIMO application along with the associated tuning devices and biasing assemblies. (a) Front view. (b) Back view.

5.7.2 Fabrication Technique

To demonstrate the potential of the proposed structure and to confirm the results obtained from simulations, a prototype is fabricated as shown in Fig. 39. The DRAs are made from three perforated dielectric of Rogers Duroid 6010 with thickness of 2.5 mm. These sheets

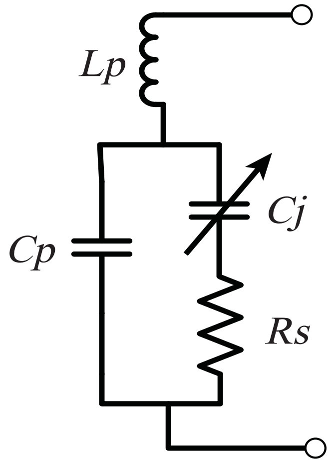

(a)

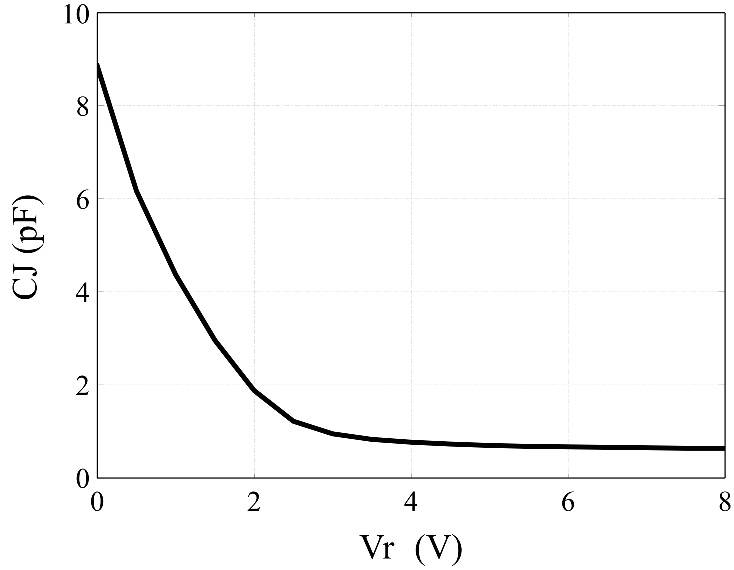

(b)

Figure 40: Non-ideal model of a packaged varactor diode. (a) Equivalent circuit model of the Skyworks SMV 1247 varactor diode ($Rs = 4.9\ \Omega$, $Cp = 0.54\ pF$, and $Lp = 0.7\ nH$). (b) Capacitance values versus the reverse biasing voltage of the Skyworks SMV 1408 varactor generated from the data provided by the manufacturer.

are stacked and placed above the feed substrate of Rogers R6002 substrate with $\epsilon_r = 2.94$, $\tan\delta = 0.0012$, and thickness of 0.508 mm. Each parasitic element is loaded by a varactor diode, which provides the required phase shift for the beam scanning. Here, a Skywork SMV1247-079LF varactor diode is selected which can be precisely modeled in HFSS by using a non-ideal parallel equivalent circuit, as shown in Fig. 40 (a). The variable junction capacitance of the varactor diode is modeled with Cj (V), and the losses are modeled with a series resistance of R_s =4.5. Furthermore, the effects of the package installation, package material, and the bonding wires or ribbons are modeled with a parasitic capacitance and inductance of $C_p = 0.54$ pF and $L_p = 0.7$ nH, respectively. The varactor develops a variable junction capacitance of 0.64–8.86 pF between 0 and 8 V of reverse bias voltage as shown in Fig. 40 (b).

A USB based analog output device (USB-3106) is used to supply the analog control voltages to the varactors by using a dc biasing network that is connected to the feed stubs of parasitic radiators. Each DC biasing branch of the network, as shown in Fig. 41 (a),

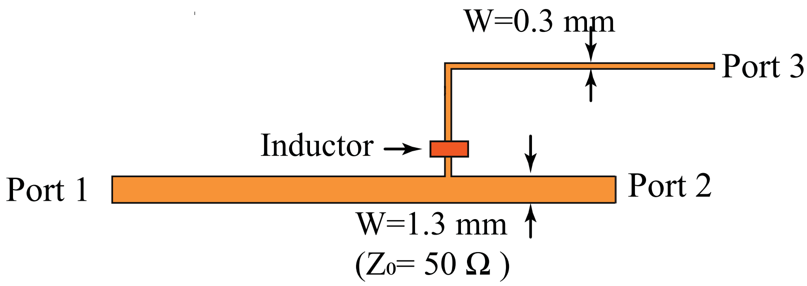

(a)

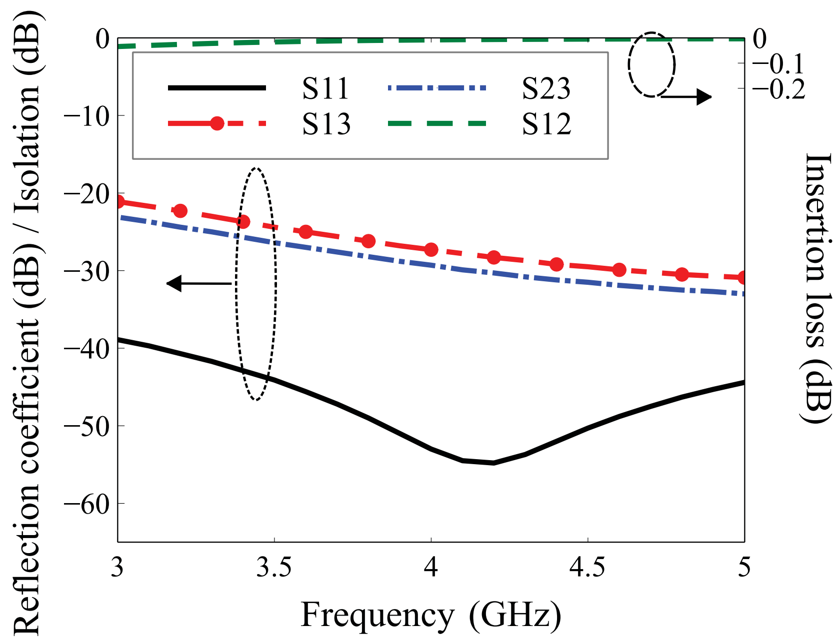

(b)

Figure 41: Biasing line design: (a) Layout of the printed biasing line connected to a 50 Ω microstrip line, and (b) Simulated scattering parameters.

consists of a high-impedance line with one inductor acting as a RF choke to isolate the microwave signals from the DC circuit. The dimensions of the dc transmission line and value of the RF inductor are carefully optimized using ADS, and the simulated results are depicted in Fig. 41(b). It is worth mentioning that the self-resonant frequency (SRF) of the choke is an important parameter in the biasing design since the inductor does not function as an inductor beyond the self-resonant frequency. The complete setup used to measure the radiation characteristics of the antenna is depicted in Fig. 42 [30]. As it can be seen, the antenna under test connects with the measuring devices and the analog

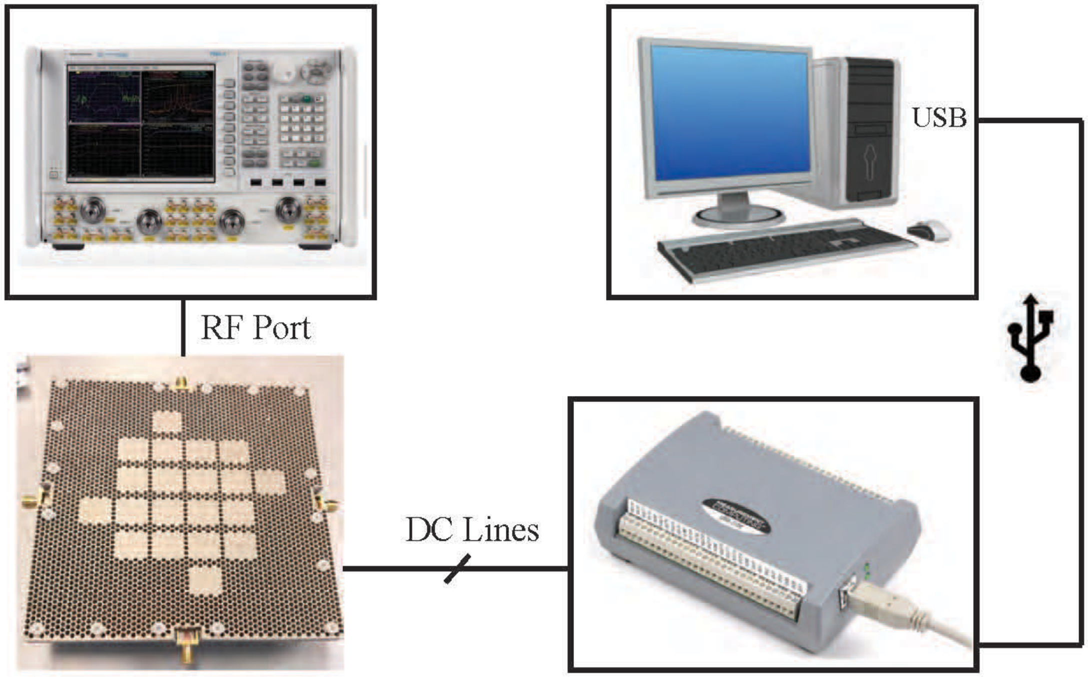

(a)

Figure 42: Setup to characterize the radiation properties of the proposed MIMO antenna.

voltage board, which are controlled by a central PC.

5.7.3 MIMO Performance

The scattering parameters of the antenna is measured using an Agilent N5227A PNA network analyzer. The scattering matrix is an important figure of merits which provides the bandwidth of an antenna. However, the scattering matrix for a 4 port antenna has 4×4 elements and tracking all these curves for a multi-port antenna is difficult. To effectively study the bandwidth of a multi-port antenna system like MIMO, a parameter referred to as the total active reflection coefficient (TARC) need to be considered.

For an N-port antenna system, the TARC can be calculated as [73]:

$$\Gamma_a^t = \frac{\sum_{i=1}^{N} |b_i^2|}{\sum_{i=1}^{N} |a_i^2|} \tag{36}$$

where b_i and a_i are the incident and reflected signal vectors with randomly phased elements, respectively. Based on the calculations in [100], TARC of a 4×1 antenna arrays is defined as:

$$\Gamma_a^t = \sqrt{\frac{|(S_1)| + |(S_2)| + |(S_3)| + |(S_4)|}{2}} \tag{37}$$

where

$$S_1 = s_{11} + s_{12}e^{i\theta} + s_{13}e^{i\theta'} + s_{14}e^{i\theta''} \tag{38}$$

$$S_2 = s_{21} + s_{22}e^{i\theta} + s_{23}e^{i\theta'} + s_{24}e^{i\theta''} \tag{39}$$

$$S_3 = s_{31} + s_{32}e^{i\theta} + s_{33}e^{i\theta'} + s_{34}e^{i\theta''} \tag{40}$$

$$S_4 = s_{41} + s_{42}e^{i\theta} + s_{43}e^{i\theta'} + s_{44}e^{i\theta''} \tag{41}$$

and, θ, θ', and θ'' are the phase of feeding ports. Therefore, TARC contains the effect of mutual coupling and the feeding phases and it can be defined as the return loss of the whole MIMO antenna array [73]. Once the S-parameters of the antenna ports have been found, the random phases are swept between 0 and 180 degrees to investigate the effect of the phase variation between ports, creating the corresponding TARC curves [73]. For each case given in Table 5, this procedure is repeated and the average TARC are presented in Fig. 43. As is observed, the worst calculated TARC is lower than -10 dB. These results shows that the array has a good efficiency across a range of possible MIMO signals. It should be noted that due to the squared magnitude of the resulting power signals, TARC may increase rapidly as the number of array elements increases [101].

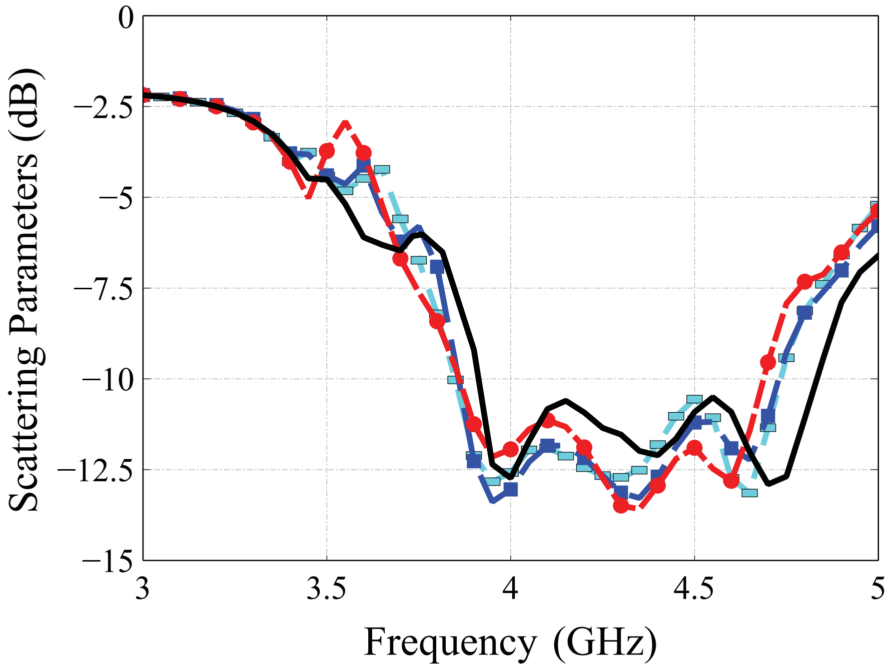

Figure 43: Measured and calculated TARC when one port is excited and the other ports are loaded to 50 .

Measured and simulated values of the isolation for given cases of Table 5, are plotted in Fig. 44. Good isolation results were observed with a worst case isolation of -19 dB in the entire frequency band. Note that isolation only represents the coupling through the antenna structure and the coupling of the antennas radiation patterns is measured by another metric known as envelope correlation coefficient (ECC) ρ_e. This metric describes how much the communication channels are isolated or correlated with each other [73].

For the given MIMO antenna system, ECC can be calculated using the radiation patterns of the antennas which is given by:

$$\rho_e = \left|\frac{\oint_V A_{ij}(\Omega)d\Omega}{\oint_V A_{ii}(\Omega)d\Omega \ \oint_V A_{jj}(\Omega)d\Omega}\right|^2 \tag{42}$$

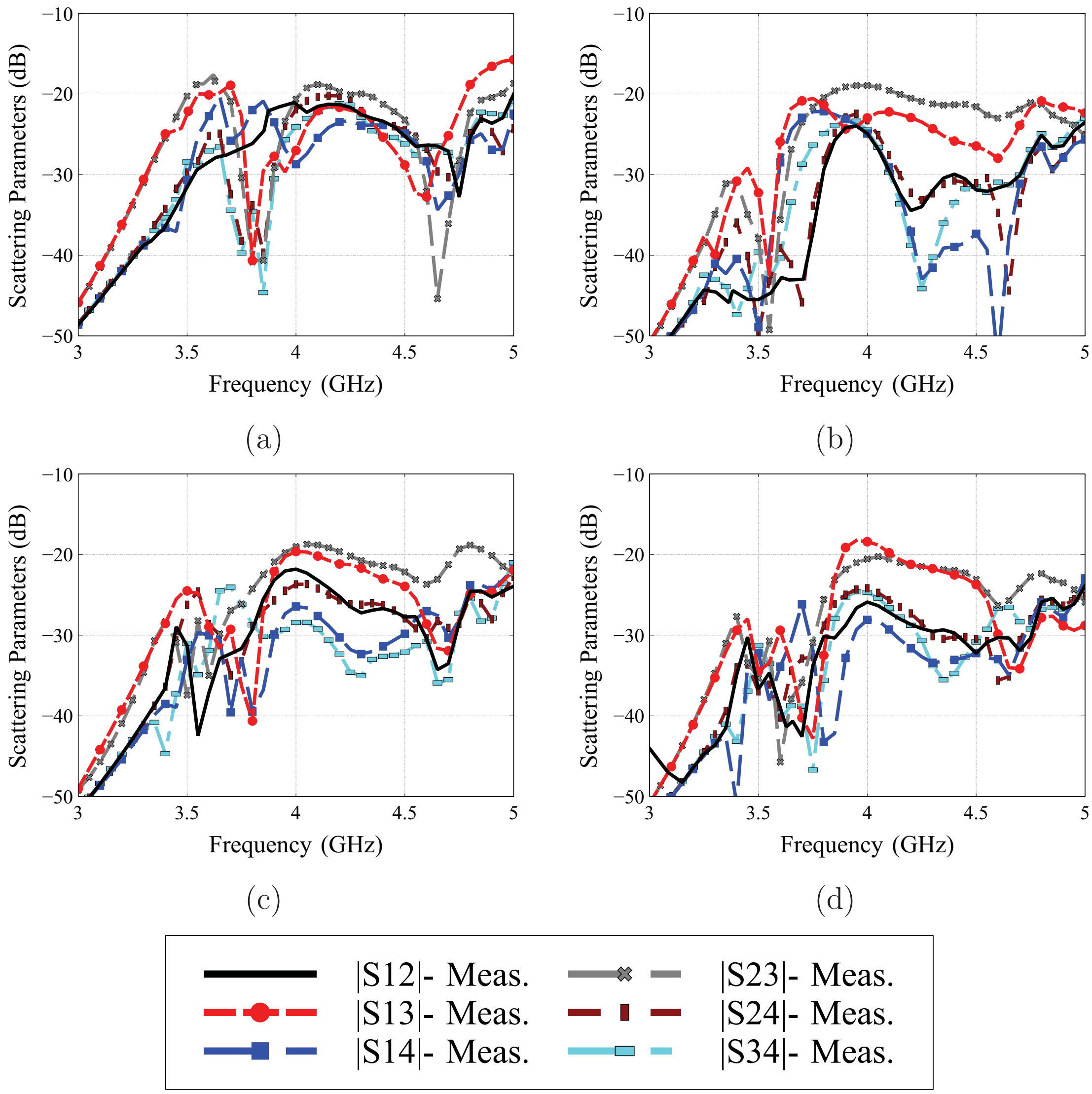

Figure 44: Measured mutual coupling between the MIMO ports for four beam scanning schemes of of Table 5

where

$$A_{ij} = \Gamma.E_{\theta i}(d\Omega).E^{*}_{\theta i}(d\Omega).P_{\theta}(\Omega) + \Gamma.E_{\varphi i}(d\Omega).E^{*}_{\varphi j}(d\Omega).P_{\varphi}(\Omega) \tag{43}$$

in which

$$E_{\theta,\varphi} = E_{\theta,m}(\theta,\varphi)\hat{\theta} + E_{\varphi,m}(\theta,\varphi)\hat{\varphi} \tag{44}$$

Table 6: Simulated and measured MEG, ECC, and BPR (K) Results for the Proposed Antenna.

Scanning Scheme	ECC (max) (Sim | meas.)	MEG (min) (Sim | meas.)	BPR (max) (Sim | meas.)
Case I	0.15 | 0.2	-3.7 | -4	0.2 | 0.3
Case II	0.07 | 0.1	-3.1 | -3.6	0.2 | 0.2
Case III	0.1 | 0.2	-3.6 | -3.3	0.3 | 0.2
Case IV	0.23 | 0.2	-4.2 | -4.3	0.3 | 0.3

where i and j span all the antenna port numbers, $E_{\theta,\varphi}$ is the electric field pattern of the antenna and $P_\theta(\Omega)$ and $P_\varphi(\Omega)$ are the angular density function of the vertical and horizontal plane, respectively. Γ is the ratio of time-averaged vertical power to time average horizontal power. To model the indoor and outdoor fading environment, Γ is set to 1 and 5 dB, receptively, and the angular density functions are assumed as Gaussian in elevation and uniform in azimuth [102].

The ECC of the antennas in different scanning schemes are calculated from the simulated and measured far-field results and are presented in Table 6. Good diversity performance is observed as the ECC values do not exceed 0.248 across the scanning schemes. It should be noted that, to have a good diversity performance, the other parameters such as branch power ratio (BPR) and mean effective gain (MEG) should be studied. BPR is a measure that shows the differences of MIMO system power levels by comparing the power level of the antenna with lowest power (P_{min}) to the one with highest power (P_{max}):

$$BPR = \frac{P_{min}}{P_{max}} \tag{45}$$

BPR can also be found from MEG of the antennas as follows [103]:

$$BPR_{i,j} = \min(\frac{MEG_i}{MEG_j}, \frac{MEG_j}{MEG_j}) \tag{46}$$

MEG considers the performance of antennas in a stochastic channel and can be calculated by finding the ratio of the mean received power to the mean incident power of the antenna. A method for calculating the MEG is proposed in [104] which is based on the measured radiation pattern of the antenna:

$$G_e = \int_0^{2\pi} [\frac{XPR}{1+XPR} G_\theta(\Omega) P_\theta(\Omega) + \frac{1+XPR}{XPR} G_\varphi(\Omega) P_\varphi(\Omega)] d\Omega \qquad (47)$$

where $G_\theta(\Omega)$ and $G_\varphi(\Omega)$ are the θ and ϕ components of the antenna power gain pattern, respectively. The other parameters are the same as (44) By following the same modeling of the indoor and outdoor fading environment, the calculated MEG from simulated and measured far-field results are presented in Table 6. It is evident that the proposed antenna satisfies the criteria of low correlation ($\rho_e < 0.5$). Furthermore, the average received power $|MEGi - MEGj|$ is less than 3 dB at the operating frequency bands which is acceptable for MIMO systems [103]. Therefore, it can be concluded that the proposed antenna exhibits good diversity performance.

5.8 Proposed Massive MIMO Structure

A larger array of ESPAR can be realized by adding similar polarized subarrays to each port of the MIMO antenna structure. These subarrays are placed in an interleaved arrangement which can suppress the grating lobes with better scanning capabilities in all azimuthal directions [98]. In order to efficiently analyze the massive MIMO structure, a simple 4×4 array as shown in Fig. 34, is modeled and simulated in HFSS. The simulated mutual couplings of this planar array are given in Fig. 45. It is observed that the isolation between ports does not exceed -18 dB in the entire frequency band. The mutual coupling between different ports can be categorized into two classes based on the exciting polarization and antenna unit arrangement [87]:

1) Class-I which is the highest mutual coupling occurs between the adjacent ports exciting

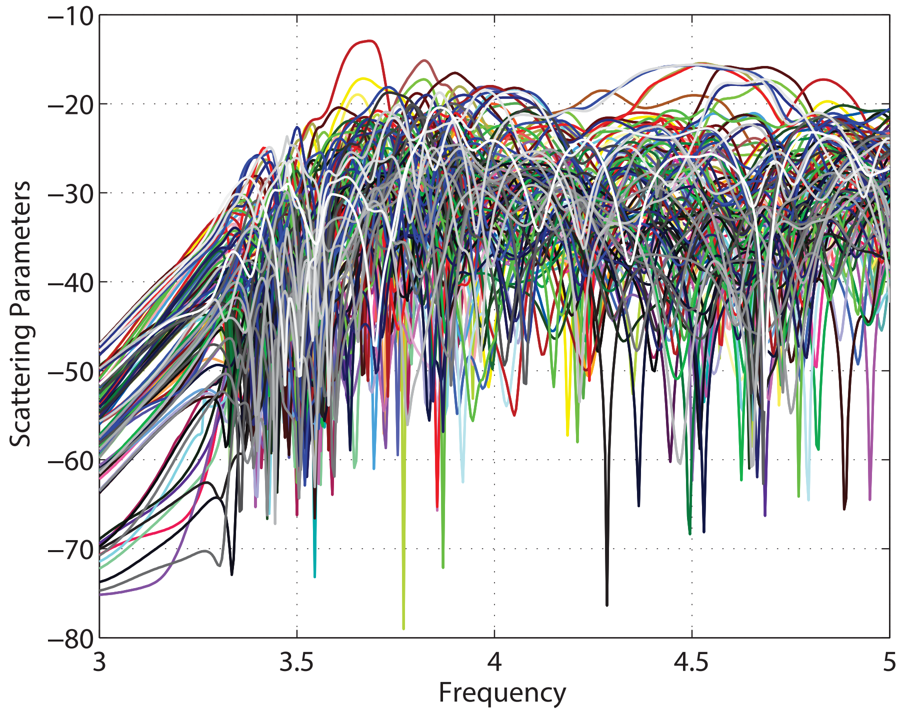

Figure 45: Simulated mutual coupling between ports in the proposed massive MIMO subarray.

same polarizations. The mutual coupling level is ranging from -18 dB to -25dB.

2) Class-II which is the lowest mutual coupling occurs between the ports exciting different polarization. The mutual coupling level is ranging from -25 dB to -50 dB.

The simultaneous multiple beams capability of the proposed 4×4 massive MIMO array panel is also analyzed [105] using HFSS. Fig. 45 presents the four beams that could be independently steered in different directions. Each beam is constructed by simultaneous excitation of four adjacent ports that have the same polarization with proper phase excitation. In addition the reactive loads of each parasitic radiators are optimized for the desired directions. The peak directivity for different scan positions is summarized in Table 7. The proposed massive MIMO antenna can be scaled to Larger size panel but at the cost of large data processing and increase in system complexity.

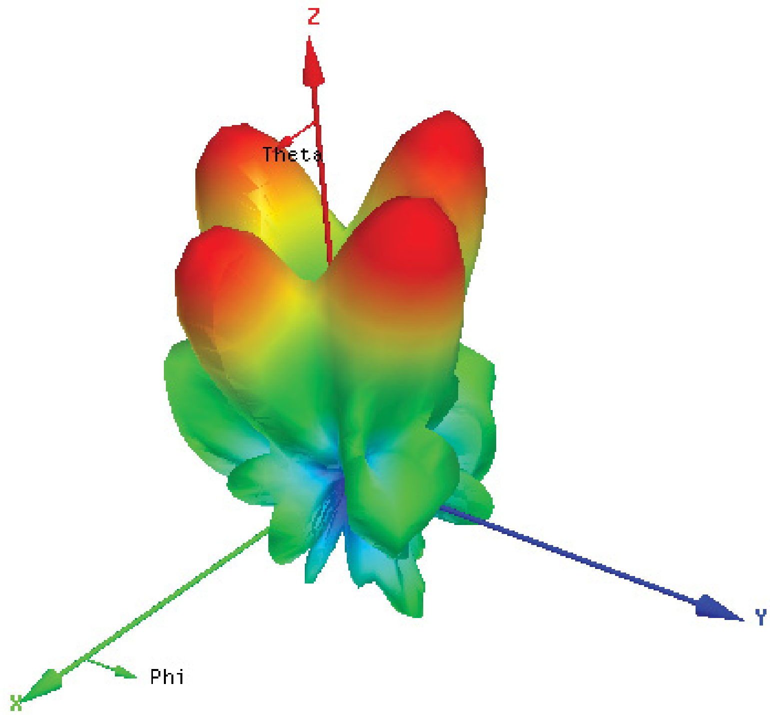

Figure 46: Simulated multi-beam capability for the proposed massive MIMO subarray generated in HFSS.

Table 7: Simulated multi-beams peak gains for four beams using the proposed massive MIMO subarray.

Scanning angle	Peak gain (dBi)
$\theta = 20°, \phi = 350°$	9.79
$\theta = 25°, \phi = 275°$	9.65
$\theta = 30°, \phi = 175°$	9.7
$\theta = 20°, \phi = 85°$	9.62

5.9 Conclusion

This chapter has investigated the performance of DRA-ESPAR in MIMO and massive MIMO systems. We have proposed a 4-port MIMO configuration that the strong mutual coupling between its elements is reduced by the orthogonal placement of the DRA-ESPAR subarrays. A thorough analysis has been completed for this structure through both simulated and physically measured results. It was observed that the proposed DRA-ESPAR can be a good candidate for MIMO applications since it can satisfy all the required criteria such as low correlations, high isolations and low branch power ratios. The proposed DRA-ESPAR has also been investigated in a massive MIMO configuration which is designed by adding similar polarized subarrays to each port of the MIMO antenna. These subarrays are placed in an interleaved arrangement which can suppress the grating lobes with better scanning capabilities in all azimuthal directions. The simulation results showed that the isolation between ports is less that -17 dB. In addition multiple beams capability of the proposed massive MIMO subarray were also explored for four simultaneous beams.

Chapter 6

Circularly Polarized ESPAR

6.1 Introduction

In the previously published works of ESPAR concept, the radiation beams were linearly polarized. Therefore, the antenna performance is extremely dependent on the proper orientation of the antenna, which is not suitable for some applications such as satellite navigation, telemetry and tracking systems. To alleviate the shortfalls related to the linear polarized beam scanning, the present chapter is focused on attaining an effective method to design an ESPAR with a circularly polarized (CP) beam-scanning feature. CP antennas with beam scanning are desired to cope with difficulties associated with mobility, inclement weather conditions, immunity to multipath distortion, and polarization rotation effects [106]. It is noted that designing a CP antenna with beam scanning is a challenging task, and there are few works in the literature that have investigated this type of the antenna [6, 106–108].

In this chapter, a simple and low-cost approach for the CP-ESPAR is proposed for the first time. The proposed antenna consists of one driven CP-DRA, which is coupled to four other parasitic CP-DRAs. The parasitic DRAs are placed in a sequential arrangement [109], and are terminated by varactors. The required phase shifts for the beam scanning are achieved by changing the reactances of the varactors, and the CP capability during the beam steering is maintained by the sequential arrangement and adjusted feeding stubs.

The chapter is organized as follows. A brief overview of polarization is first presented in Section 6.2, followed by design techniques to generate circular polarization for a DRA. The design principles of the proposed CP-ESAPR, as well as the simulation results, are described in Section 6.4. The fabrication method used to realize the proposed antenna and the experimental results are outlined in Section 6.5. Finally, Section 6.6 summarize the chapter.

6.2 Polarization Overview

Polarization is a fundamental property of an electromagnetic wave which refers to the motion of an electric field vector at a fixed location as time is changing [110]. There are three types of polarization which are shown in Fig. 47. It is noted that the most common forms of polarization utilized are linear polarization and circular polarization. The electromagnetic field in the form of a vertical or horizontal plane wave in space is said to be linearly polarized. If the electromagnetic field is composed of two plane waves of equal amplitude by 90° phase difference, then the field is referred to as circularly polarized.

The purity of a CP wave depends on the ratio between the magnitude and phase of the two linearly polarized components which is referred to as axial ratio (AR). The AR is defined as [37]:

$$AR = 10log\left(\frac{E_x^2 + E_y^2 + \sqrt{E_x^4 + E_y^4 + 2E_x^2E_y^2cos(\psi)}}{E_x^2 + E_y^2 - \sqrt{E_x^4 + E_y^4 + 2E_x^2E_y^2cos(\psi)}}\right) \tag{48}$$

where $\psi = 2(\phi_y - \phi_x)$. As it can observed in 48, if $E_x = E_y$ and $\phi_y - \phi_x) = \pm\pi/2$, the $AR = 0$ and the CP wave will be pure. It is noted that in practice, the AR of a CP antenna should be less than 3 dB.

Circular polarization is desirable for many antennas due to the following reasons:

Faraday rotation:

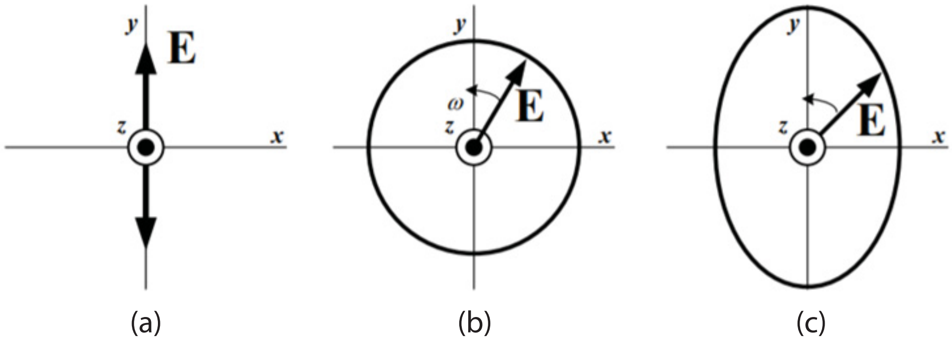

Figure 47: The motion of an electric field vector at a fixed location as a function of time, illustrating different electromagnetic field polarizations. (a) Linear Polarization. (b) Circular polarization. (c) Elliptical polarization.

Faraday rotation is an interaction between a light beam and magnetic field that can rotate the plane of polarization of aN LP wave. This effect results from the fact that the ionosphere is a magneto-ionic region and causes issues for satellite communications. However, the circular polarized wave is immune of this phenomenon and there is no need for exact signal alignment.

Signal-fading effects:

Another advantage of circular polarization is that by reflecting off a surface, the sense of polarization will be changed. Therefore, a CP antenna has some immunity to the signal-fading effects of reflected waves interfering with the desired wave.

Atmospheric conditions:

Atmospheric conditions such as rain or a cloud system can significantly degrade a signal. These conditions can change the rotation of the signal and LP is found to be more prone to these effects rather than CP.

Easier installation:

The alignment of the LP feed is time consuming since it needs more precision in terms of height and the plane of the polarization. However, the set up for CP feeds are quicker, since there is a minimal risk of misalignment and encountering interference.

6.3 Techniques to Generate Circular Polarization for a DRA

As was mentioned in Section 6.2, a CP wave can be synthesized from two spatially orthogonal linearly polarized waves that have $\pm\pi/2$ phase difference. Therefore, any antenna that can produce these two spatially orthogonal LP waves, which are referred to as orthogonal degenerate modes, can generate a CP signal. This concept can also be used in the design of a CP-DRA. The most challenging task in designing a CP antenna is to maintain the amplitude and phases of the orthogonal modes to within their maximum allowable errors for achieving the desired axial ratio over the required bandwidth of operation.

Generally, to generate circular polarization, three following common methods can be used:

- Double feeding system.
- Single feeding.
- Sequential rotation technique.

These methods will be briefly reviewed in the following sections.

6.3.1 Double Feeding system

This technique can be used in the DRAs that are symmetric along the x and y axes such as square, circular or annular DRAs. To generate circular polarization, two identical feeds can be placed on two orthogonal sides of the DRA named as V_x and V_y. To obtain circular polarization, these two feeds should have equal amplitude and $\pm\pi/2$ phase difference as will be discussed in Chapter 7. To this end, a power divider network is commonly used, such as a hybrid coupler, a Wilkinson splitter, or a T-junction, as shown in Fig. 48. It is noted that in these techniques, the mutual coupling between the feeds plays an important

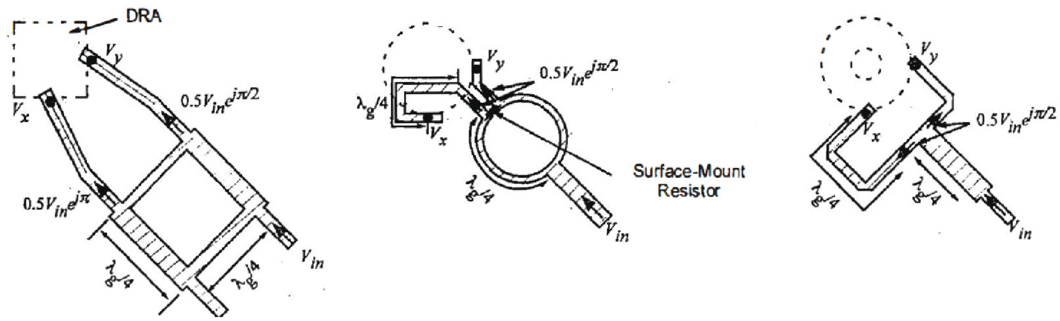

(a) (b) (c)

Figure 48: Examples of power divider networks for generating circular polarization. (a) Hybrid coupler. (b) Wilkinson splitter. (c) T-junction splitter. (Petosa [21], ©2007 ARTECH HOUSE, INC.)

rule on AR performance. For instance, it is shown in [21] that coupling levels of –10 dB would significantly degrade the axial ratio performance, and the antenna cannot achieve the minimum axial ratio of 3 dB. Therefore, it is important to design the feed network to maximize high isolation between the two feed ports.

6.3.2 Single Feed

Circular polarization can also be generated from a single feed point. Comparing to the double feeding systems, this technique has a narrower AR bandwidth. However, it has attracted many researchers' interest since it avoids the complex feeding networks of the double feeding system which is desired in an array environment.

The mechanism of single point feed is based on the perturbation of one shape of a DRA to create degenerate modes. Perturbation can change the Q factor and the resonance of the two orthogonal modes. Therefore, by a proper perturbation, the degenerate modes can have a 90° phase difference to generate a CP signal.

Chamfered rectangular, quasi-square cross-section, and cross-DRA are the most common perturbation methods that alter one dimension of DRA. These techniques are shown in Fig. 49. It should be noted that the perturbation can also be performed on the DRA

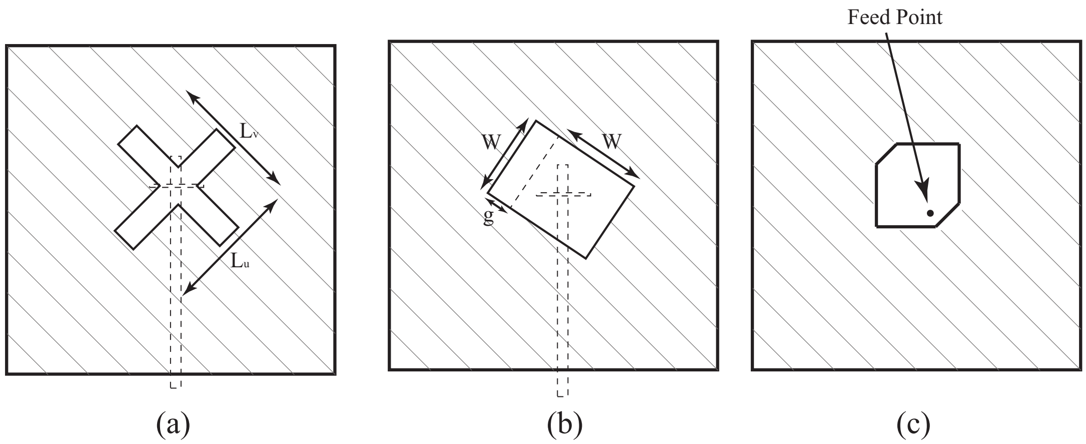

Figure 49: Perturbation techniques on DRA dimensions to generate CP signal. (a) cross DRA (Ittipiboon et al. [111], ©1994 IEEE). (b) quasi-square cross-section (Oliver et al. [112], ©1995 IEEE). (c) Chamfered DRA (Haneishi et al. [113], ©1985 IET).

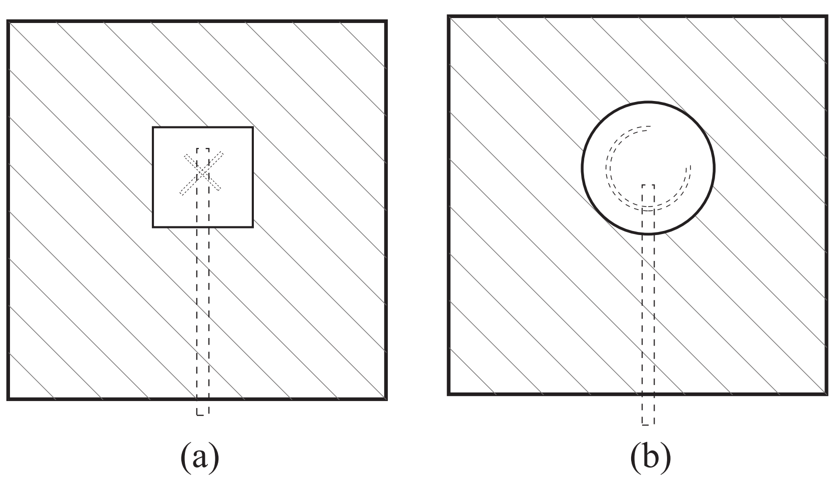

Figure 50: Perturbation techniques on DRA feeding to generate a CP signal. (a) Rectangular DRA fed with a cross-shaped (Huang et al. [114], ©1999 IEEE). (b) annular slots for generating circular polarization (Leung et al. [114], ©2001 IET).

excitation to excite the two spatially orthogonal degenerate modes. The common perturbed feedings for a CP DRA are cross-slot and annular-slot apertures that are shown in Fig 50.

6.3.3 Sequential rotation technique

The dual and single feeding techniques are simple in practice, but their achievable axial ratio bandwidth is limited to a few percent. Therefore, if these elements are used in a uniform array, the CP-bandwidth of the array will be the same as the CP-bandwidth of a single element [115]. Sequential rotation feeding is a method that can be used to extend the CP bandwidth [109, 116]. This technique is realized by placing N linearly polarized antennas along the circumference of a circle, as presented in Fig. 51(a). Each element is rotated by an angle of phi=360/N and fed by equal amplitudes and phase equal to the rotated angle. The adopting of a sequential rotation technique for two or four element subarrays is shown in Fig. 51(b).

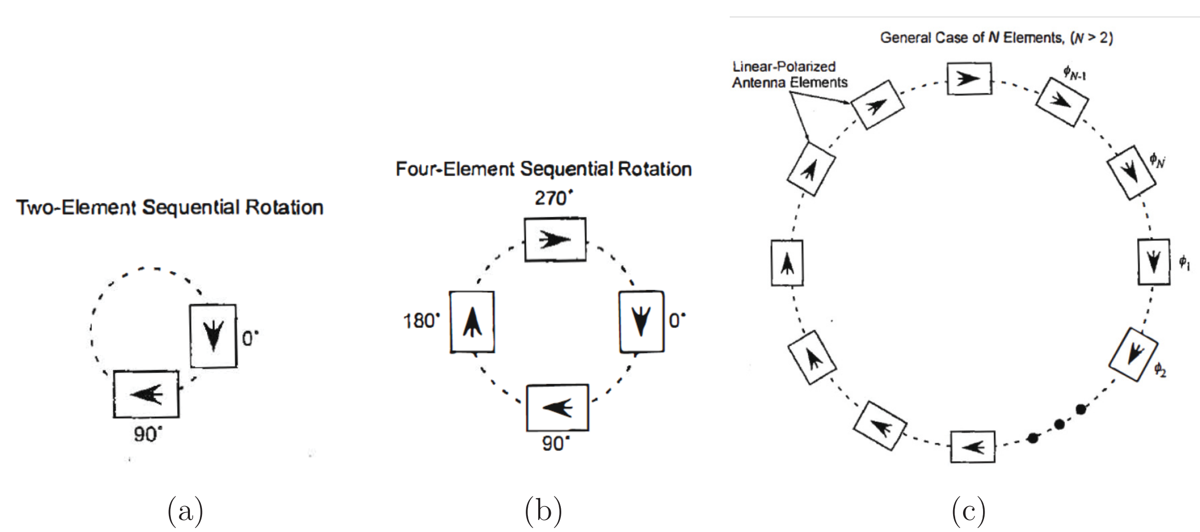

Figure 51: The sequential rotation array technique for circular polarization. (a) Two-element sequential rotation. (b) Four-element sequential rotation. (c) General case of N element. (Petosa [21], ©2007 ARTECH HOUSE, INC.)

6.4 Antenna Design and Theory

6.4.1 Antenna Structure

The geometry of the proposed CP-ESPAR is shown in Fig. 52. It consists of one driven DRA located at the center, which is coupled to four parasitic DRAs terminated by reactive loads. Note that the main difference between this configuration and the conventional LP-ESPAR [98], is that the parasitic radiators are placed in a sequential rotational arrangement [109], resulting in an improved circular polarization performance of the array with a wider CP-bandwidth. In this configuration, we have used DRAs for their exceptional features, such as high radiation efficiency, wide impedance bandwidth, and their low loss [97]. The DRAs are made of a dielectric with a thickness of 5 mm and relative permittivity of 10.2, and are placed above the aperture-coupled feed substrate of Rogers RT6002 (ϵ_r =2.94, tanδ = 0.0012) with a thickness of 0.508 mm. The aperture-coupled structure provides ample space for the biasing network by separating the radiating elements and feeding lines, which is extremely useful in expanding the subarray to larger arrays. Moreover, we have used the perforation technique to fabricate DRAs from a single dielectric sheet. By this means, we can eliminate the difficulties in aligning and bonding the individual element of the DRAs [99]. The utilized perforation technique can be clarified considering Fig. 53. In Fig. 53(a), we have shown the radiating layer of the proposed ESPAR and its perforated structure. It can be observed that the free space between the elements in the radiating layer is replaced with lattice of holes in the perforated structure. The diameter and spacing of the holes determine the effective dielectric constant of the material surrounding the DRAs, which is defined as [51]:

$$\epsilon_{eff} = \epsilon_r\big((1 - \frac{\pi}{2}(\frac{d}{d+g})^2\big) + \frac{\pi}{2}(\frac{d}{d+g})^2 \tag{49}$$

where d is the perforated hole diameter, and g is the edge to edge distance between the holes, as shown in the Fig. 53(b). The effective dielectric constant versus the diameter of the holes is also shown in Fig. 53(b). As can be observed, the dielectric constant of the surrounding areas of the DRAs is reduced from 10.2 to 3.1 by making lattices of holes with a diameter of 2.1 mm and a spacing of 0.25 mm.

6.4.2 Antenna Design

The first step in implementing the proposed CP-ESPAR is designing the driven element with a good CP performance. There are several techniques reported in [21] for achieving circular polarization. Here, we cut a narrow crossed-slot with unequal arms in the ground plane [114] to have circular polarization. It is worth noting that according to [45], the fundamental mode of the proposed DRA is TE_{11y} and the presence of the crossed slot on the ground splits this mode into two near-degenerate orthogonal modes to form CP polarization [114]. HFSS [117] is used to design the driven antenna and optimize the dimensions of the DRA, cross slot, and aperture feeding. It is noted that, the driven element should be well matched to obtain the best possible antenna efficiency and provide sufficient coupling to the surrounded parasitic elements [61]. The designed square DRA has a lengths of 7.3 mm, and the dimensions of the cross slots are 9.1 mm $\times$ 1 mm and 5 mm$\times$1 mm. The designed antenna operates at center frequency of 10.5 GHz with –10 dB reflection coefficient bandwidth of 14.17% (9.96-11.48 GHz). The antenna achieves a 3-dB axial ratio (AR) bandwidth of 3.97% and gain of 6$\pm$0.3 dBic over the operating band. For brevity, the simulated results are not presented here.

Once the driven DRA is designed, the second step is to place the parasitic DRAs close to the driven element. To this end, we propose to place the parasitic elements based on the sequential feeding technique which is capable of improving the CP performance in terms of bandwidth and cross-polarization [109]. In this technique, the antenna elements and their corresponding feeding phases are rotated by a particular angle as presented in [109]. For

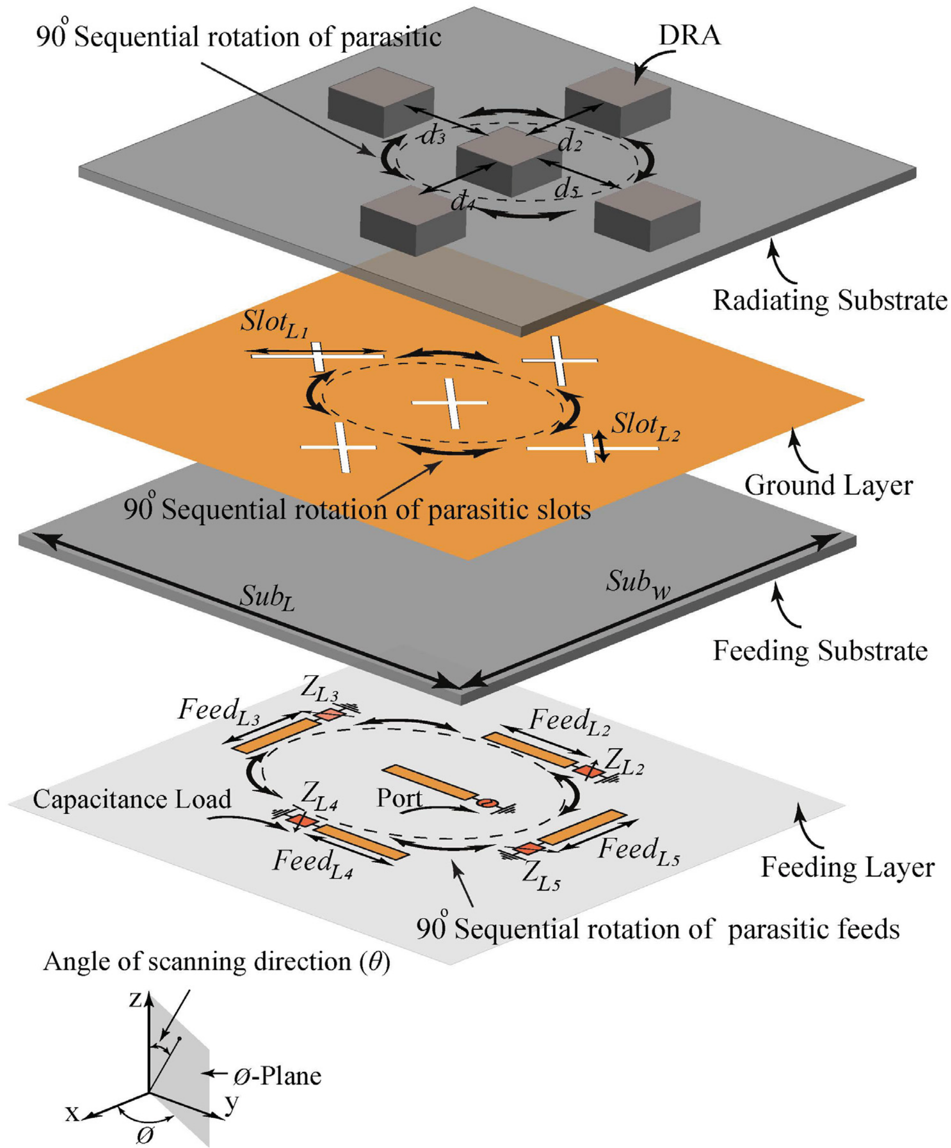

Figure 52: CP-ESPAR subarray structure in air fed by crossed-narrow slots that are coupled to microstrip lines from the back of the structure ($Sub_W = Sub_L = 45\ mm$, $d_2 = d_3 = d_4 = d_5 = 12\ mm$, $Slot_{L1} = 9.1\ mm$, $Slot_{L2} = 5\ mm$, $Feed_{L2} = 14\ mm$, $Feed_{L3} = 13.6\ mm$, $Feed_{L4} = 14.2\ mm$ and $Feed_{L5} = 13.4\ mm$). For illustration, but the built array was connected by lower dielectric materials provided by perforation.

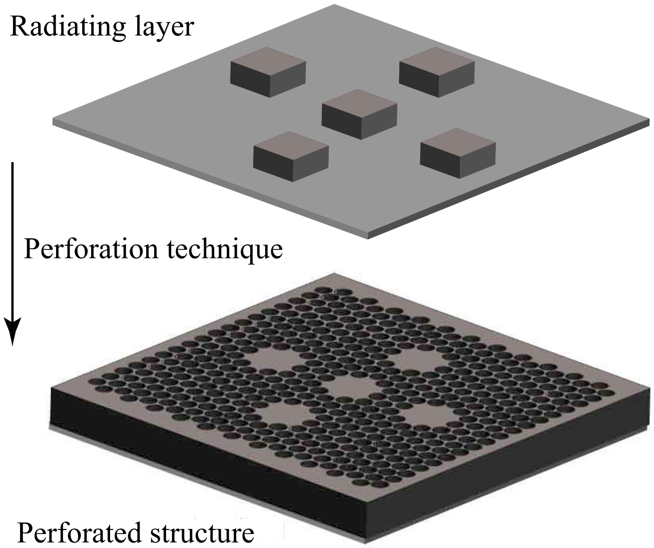

(a)

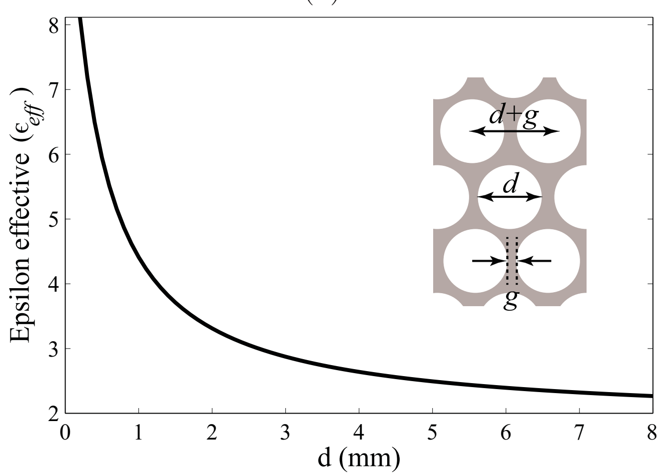

(b)

Figure 53: Using perforation technique to alleviate the problems associated with aligning and bonding the individual elements of the DRA. (a) Replacement of the free space between the elements in the radiating layer with lattice of holes in the perforated structure based on the perforation technique. (b) Variation of the effective dielectric constant with different diameters of perforated holes (d) for the fixed coupling gap (g) of 0.25 mm.

the rotation, we can adopt one of the approaches presented in [118, Fig. 2]. In this work, the proposed structure shown in Fig. 52 is used. The parasitic elements are arranged as a 2×2 square lattice with angular orientations of 0°, 90°, 180° and 270° to enhance the coupling between the excited and the parasitic elements.

To clarify the remaining steps of the design, a network circuit analysis is performed as

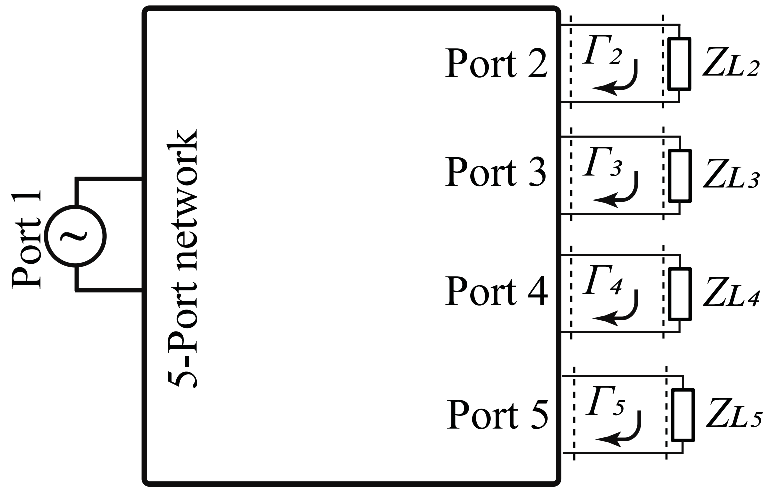

(a)

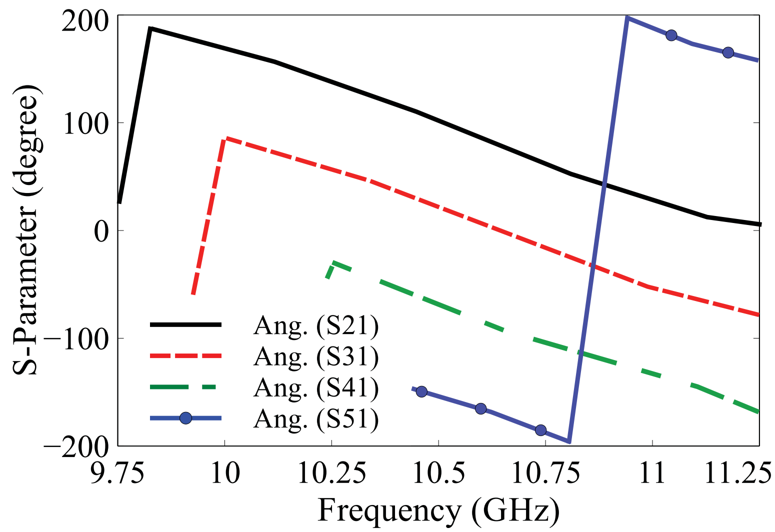

(b)

Figure 54: Equivalent circuit analysis of the proposed antenna: (a) Five-port network representing the basic antenna arrangement of Fig. 52. (b) Simulated S-parameters (phase) of the optimized five-port network.

shown in Fig. 54. According to Fig. 54(a), the CP-ESPAR can be modeled as a five-port network, where its center element (port 1) is connected to the source, and the parasitic antennas (ports 2, 3, 4, and 5) are terminated with reactive loads. The reactive loads can be represented by their reflection coefficient as:

$$\Gamma_{Li} = \frac{Z_{Li} - Z_{0i}^*}{Z_{Li} + Z_{0i}^*} \tag{50}$$

where Z_{Li} and Z_{0i} are the termination load impedance and the port impedance of the ith parasitic antenna port, respectively. According to the theory of vector superposition, the total radiated electric field of the proposed subarray is the vector sum of the far-zone electric fields of the driven and parasitic radiating elements. The radiated electric field of the parasitic elements is composed of the coupled radiated field of the driven element, which is reflected from the reactive load and re-radiated into free space. The total far-field ($\vec{E}_{V_{total}}$) in a direction angle of θ, $\phi-$plane can then be written as [61]:

$$\vec{E}_{V_{total}} = \vec{E}_{V_1}(\theta,\phi) + \sum_{i=2}^{5}\left(\vec{E}_{V_i}(\theta,\phi) \times |S_{i1}|\, e^{j(\phi_{coupling_i}+\phi_{radiation_i}+\phi_{reflection_i})}\right) \quad (51)$$

where,

$$\phi_{coupling_i} = \measuredangle S_{i1} \quad (52)$$

$$\phi_{radiation_i} = k_0 \times d_i \times \sin(\theta) \times \cos(\phi - \phi_i) \quad (53)$$

$$\phi_{reflection_i} = \measuredangle \Gamma_{Li}. \quad (54)$$

Here, $\vec{E}_{V_1}$ and $\vec{E}_{V_i}$ are the electric field vector of the driven antenna and the ith parasitic antenna, respectively. It is worth mentioning that the $\vec{E}_{V_i}$ differs from the driven antenna-radiated field, because each parasitic element is rotated around the z-axis. Multiplying the rotation matrix [119] with the radiated field of the driven antenna can be used to calculate the radiated field of the other parasitic antennas. The term S_{i1} represents the coupling from the driven DRA to each parasitic DRAs, whose magnitude and phase are regarded as the excitation amplitude and the excitation phase of the parasitic elements, respectively. $\phi_{radiation}$ is the radiation phase which denotes the differential distance by which the planar wavefront reaches the ith parasitic element of the array compared with

Table 8: Scanning Schemes and Simulated Antenna CP-Radiation Performances (All Values Given at 10.5 GHz)

Scanning Scheme	1	2	3	4	5	6
$\phi-$plane	0°	0°	0°	0°	45°	90°
Scan Angle (θ)	0°	5°	10°	18°	22°	−22°
Z_{L1} (pF)	1.6	1.4	1.2	1.0	3.3	1.2
Z_{L2} (pF)	3.5	3	2.7	2.3	2.6	1.4
Z_{L3} (pF)	1.4	1.3	1.5	1.2	1.8	4
Z_{L4} (pF)	1.3	1.3	1.2	1.6	1.2	3.7
S_{11} (dB)	-26	-21	-28	-32	-24	-23
Peak Gain (dBic)	6.6	6.2	6.15	6.55	5.95	6
AR (dB)	0.9	1.2	1.4	0.95	2.3	1.2

the origin. The terms d_i and ϕ_i are, respectively, the radial and azimuthal positions of the ith parasitic element in the x-y plane, and k_0 is the free space wave number. The phase of the reflection coefficient which is the phase delay introduced into the parasitic element for the beam-steering purposes is shown by $\phi_{coupling}$.

Using the network analysis, we now explain the third step in designing the proposed CP-ESPAR. This step aims at forming the progressive 90° phase difference between the parasitic DRA excitations, which is a necessity in sequential rotation technique to obtain a CP antenna. Note that since there is no direct feeding in the proposed configuration, the mutual coupling between DRA elements has been considered as the feeding mechanism. To satisfy the progressive 90° coupling phase difference, we should adjust two sets of parameters: the distances between the driven DRA and the parasitic DRAs (as shown by $d_2, \cdots, d_5$ in Fig. 52) and the lengths of the parasitic feed stubs (as shown by $Feed_{L2}, \cdots, Feed_{L5}$ in Fig. 52).

To find the optimal values of these parameters, we have simulated the driven and the parasitic antennas using HFSS. In order to obtain the required coupling phase information, the driven and the parasitic feed stubs are terminated with 50-ohm discrete ports in the simulation. Fig. 54(b) shows the coupling phase of the parasitic DRAs for the optimized

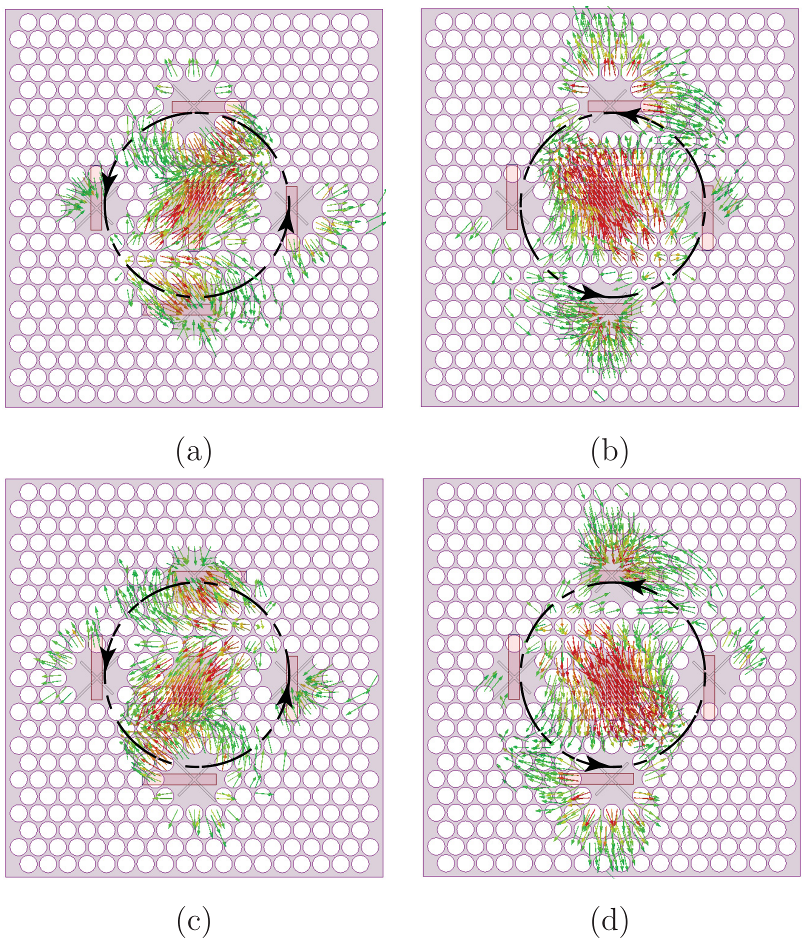

Figure 55: Simulated E-field distribution over the apertures for scanning scheme 1 at different phases: (a) 0°, (b) 90°, (c) 180°, and (d) 270° at the center frequency 10.5 GHz.

values of these parameters. It is observed that the progressive coupling phase difference between the parasitic elements is 90°. In adjusting the coupling distances in simulation, it is imperative to note that too close coupling distances can disrupt the impedance matching along with the CP performance, whereas too long distances can reduce the mutual coupling level necessary for exciting the parasitic DRAs.

In the last step of the CP-ESPAR design, we use the tunable reactive loads to enable the array scanning. The proper reactive loads for the desired beam scanning directions can be found using (50) to (54). By substituting (52), (53), and (54) into (51), the total electric field for a specific direction can be found. Now, solving (51) for the desired beam scanning direction provides all $\measuredangle\Gamma_{Li}$. Then, using (50), the reactive termination can be obtained.

The simulated CP characteristics of different beam scanning schemes are presented in Table I. These schemes are chosen to investigate the scanning performance in various $\phi-$planes with positive and negative scan directions. As expected, the beam scanning is obtained by changing the reactances of the loads terminating the stub of the parasitic elements. It is also observed that the impedance matching is maintained below –20 dB at the operating frequency for all scanning beams. Furthermore, the gain variation is 0.9 dB across the scanning range, and the scanning is achieved without degrading the CP performance.

To illustrate the operating mechanism of the proposed CP-ESPAR, the simulated electric field over the apertures for scanning scheme 1 is exhibited in Fig. 55. The E-field smoothly rotates anti-clockwise resulting in the right hand (RH) CP waves. According to the simulation results, the difference between the level of the co-polarization (RH) and the cross polarization (LH) is –22.6 dB.

6.5 Fabrication and Measurements

The proposed CP-ESPAR is fabricated and measured to validate the design approach. A photograph of the fabricated antenna is shown in Fig. 56. The DRAs are fabricated from dielectric Rogers Duroid 6010 sheet by perforating lattice of holes using a conventional computer controlled milling machine. Each parasitic element is loaded by a varactor diode, which provides the required phase shift for the beam scanning. Here, a Skyworks SMV 1408 varactor diode is selected due to its low loss at frequencies above 10 GHz. Note that the varactor diodes are precisely modeled in HFSS by using a non-ideal parallel equivalent circuit, as shown in Fig. 57(a). In this circuit, as provided by the manufacturer, the variable junction capacitance of the varactor diode is modeled with $C_j(V)$, and the effect of the varactor losses is modeled with a series resistance of $R_s = 0.8\ \Omega$. Furthermore, the effects of the package installation, package material, and the bonding wires or ribbons

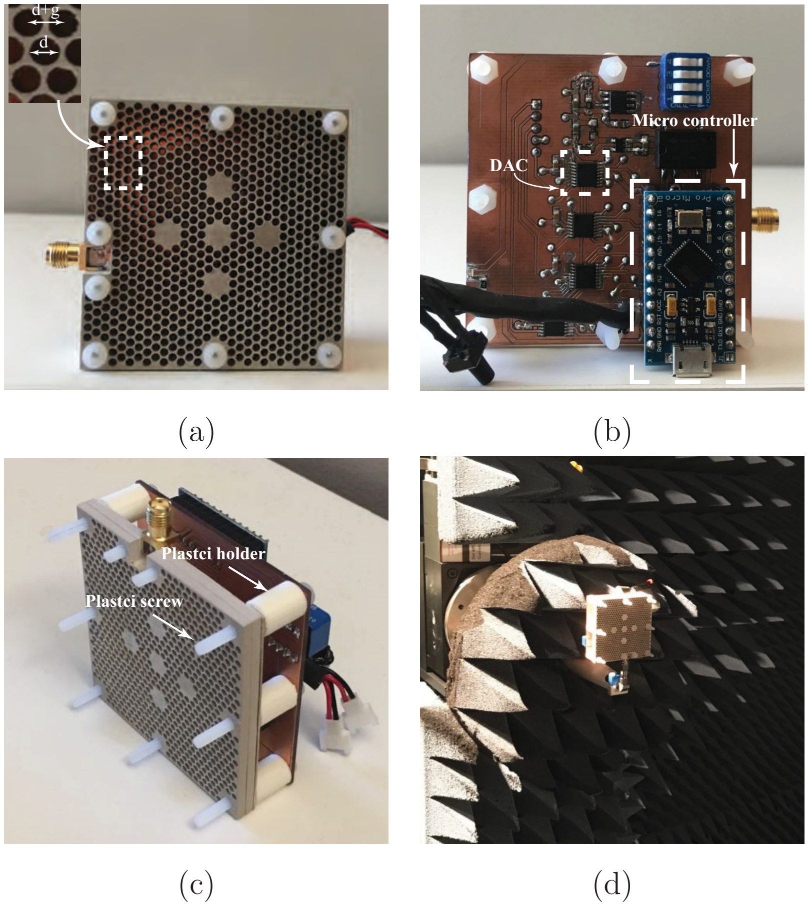

Figure 56: Photo of the proposed CP-ESPAR along with the associated tuning devices and biasing assemblies. (a) Front view. (b) Back view. (c) Side view. (d) Radiation pattern measurement setup.

are modeled with a parasitic capacitance of $C_p = 0.21$ pF and a parasitic inductance of $L_p = 0.45$ nH. The varactor develops a variable junction capacitance of 0.95 to 4.08 pF between 0 to 30 V of reverse bias voltage as shown in Fig. 57(b). A control board composed of an array of digital to analog converters (AD5761R, Analog Devices Inc.) and a microcontroller (ATmega32U4, Atmel Corp.) is placed behind the subarray to supply the control voltages. The schematic of the designed DC board is shown in Fig. 59. A DC biasing network is connected to the feed stubs of each parasitic radiator to provide the appropriate biasing voltage to each varactor. Each DC biasing branch of the network, as shown in Fig. 58(a), consists of a high impedance line with one radial stub, which provides an RF choke in the operating frequency band. The dimensions of the

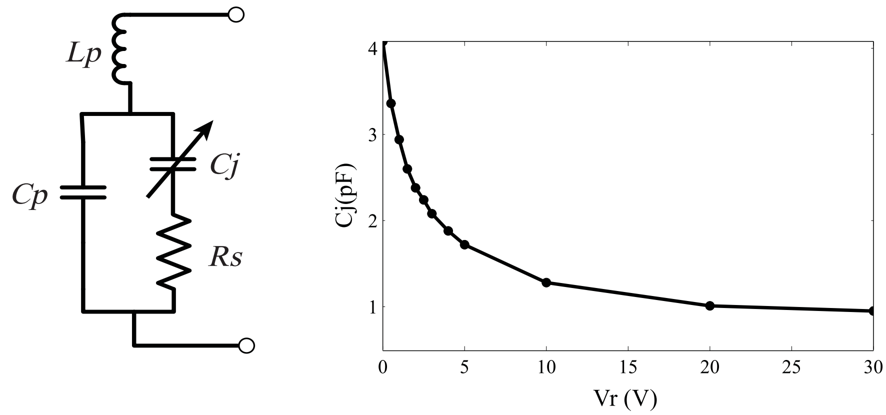

(a) (b)

Figure 57: Non-ideal model of a packaged varactor diode. (a) Equivalent circuit model of the Skyworks SMV 1408 varactor diode ($Rs = 0.8\ \Omega$, $Cp = 0.21\ pF$, and $Lp = 0.45\ nH$). (b) Capacitance values versus the reverse biasing voltage of the Skyworks SMV 1408 varactor generated from the data provided by the manufacturer.

DC transmission line and the radial stub are carefully optimized using HFSS, and the simulated results are depicted in Fig. 58(b).

Far-field characteristics of the fabricated antenna were measured using the anechoic chamber facilities at Concordia University. The simulated and measured results for three selected scanning schemes (1, 4, and 6) given in Table I, are shown in Fig. 60 and Fig. 61. Note that these selected schemes satisfactorily describe the performance of the antenna. In this respect, since the presentation of other schemes (2, 3, and 5) do not provide additional information and for the sake of conciseness, we have only demonstrated the results for the selected schemes. The simulated and measured co-polarized radiation patterns (RH) of the proposed antenna are shown in Fig. 60(a). It is observed that the main beam direction changes with the proper choice of the reactive loads. Fig. 60(b) shows the simulated and measured cross-polarized radiation patterns (LH) of the proposed antenna. Evidently, the cross-polarization level within the 3-dB bandwidth of the main beam is less than -15 dB, which ensures that the CP performance is maintained within the scanning beam. In addition, the AR performance of the proposed CP-ESPAR is shown in Fig. 60(c) which confirms that the axial ratio for all beams is below 3-dB within the main beam direction.

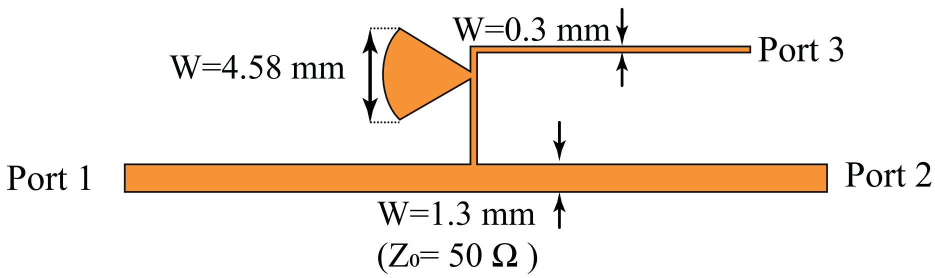

(a)

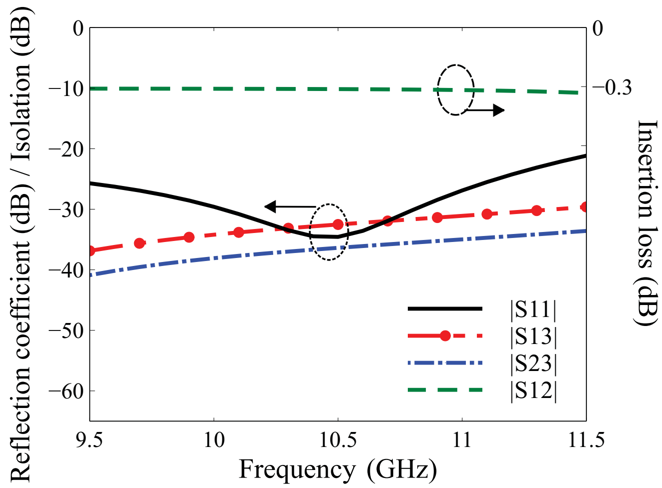

(b)

Figure 58: Biasing line design: (a) Layout of the printed biasing line connected to a 50 Ω microstrip line, and (b) Simulated scattering parameters.

An Agilent N5227A PNA network analyzer was used to perform the measurements of the reflection coefficients of the antenna, and the results are shown in Fig. 61(a). As it can be observed, the measured reflection coefficient is below –10 dB from 10.03 to 10.75 GHz. The measured realized gain is depicted in Fig. 61(b) which shows that the antenna has a 3-dB gain bandwidth of 9.7%. Fig. 61(c) illustrates the axial ratio versus frequency of the proposed antenna, which is observed at the peak gain direction of the scanned beams. It is noticed that the axial ratio level is below 3 dB in 10.3 to 10.7 GHz. The present CP antenna bandwidth is 3.8%, which is the overlap of 10-dB return loss, 3-dB axial ratio bandwidths, and 3-dB gain bandwidth.

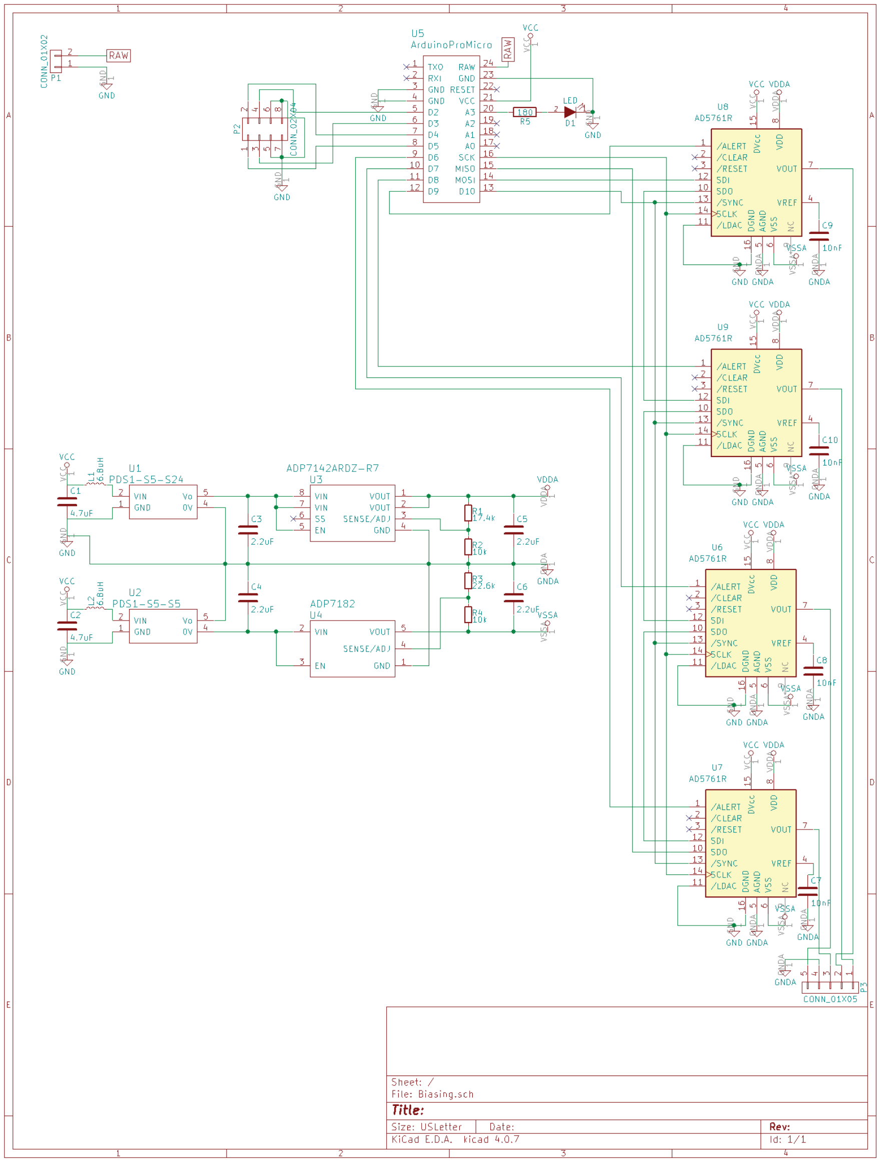

Figure 59: Schematic of the designed DC board.

The simulated results are also depicted in Figs. 60 and 61, which confirm the measurements. The slight discrepancy between the simulation and measurement might be due to the possible air gap between the dielectric layers as well as the possible misalignment between the radiating elements and the ground plane. To accurately describe these discrepancies, a parametric study has been performed using HFSS, and the results are depicted in Fig. 62. It is worth mentioning that the reference antenna characteristic,

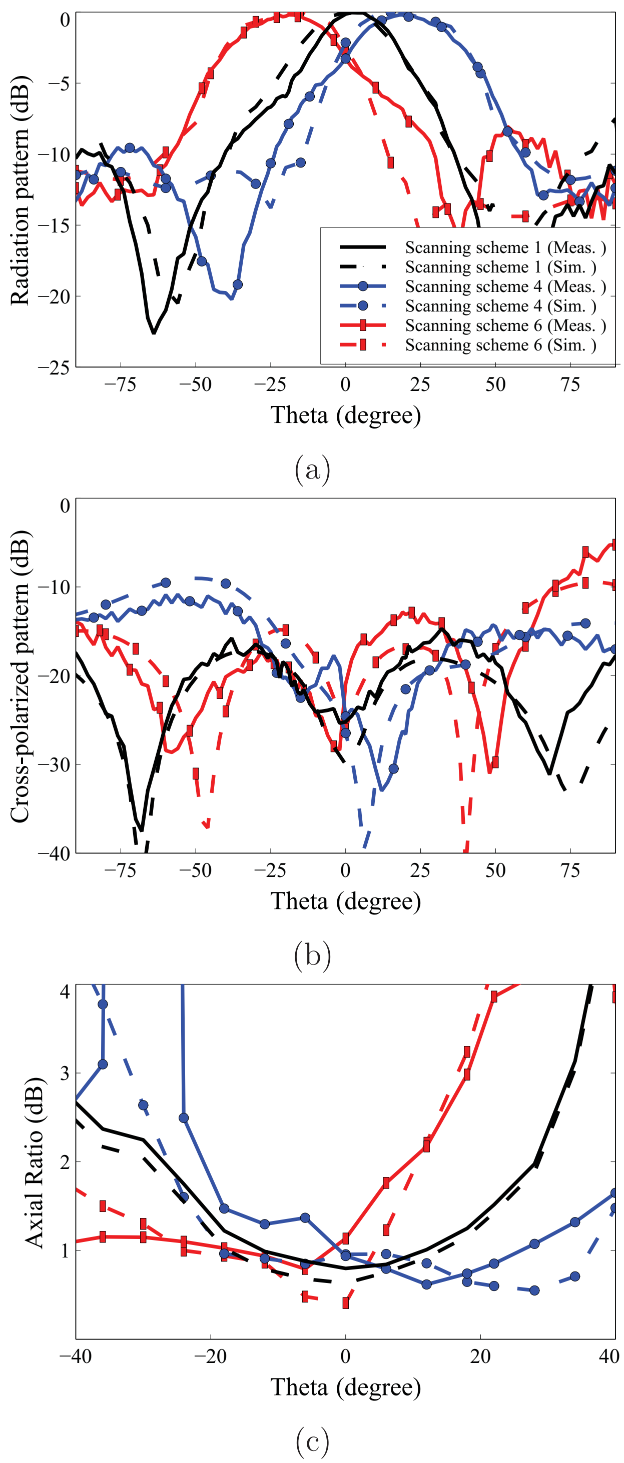

Figure 60: Simulated and measured characteristics of the antenna for the selected scanning scheme in Table I. (a) RH-gain pattern, (b) LH-gain pattern, and (c) Axial ratio.

shown in this figure, is for to the broadside direction (indicated by scanning scheme 1 in Table I). Fig. 62(a) displays the radiation patterns of the proposed antenna for different

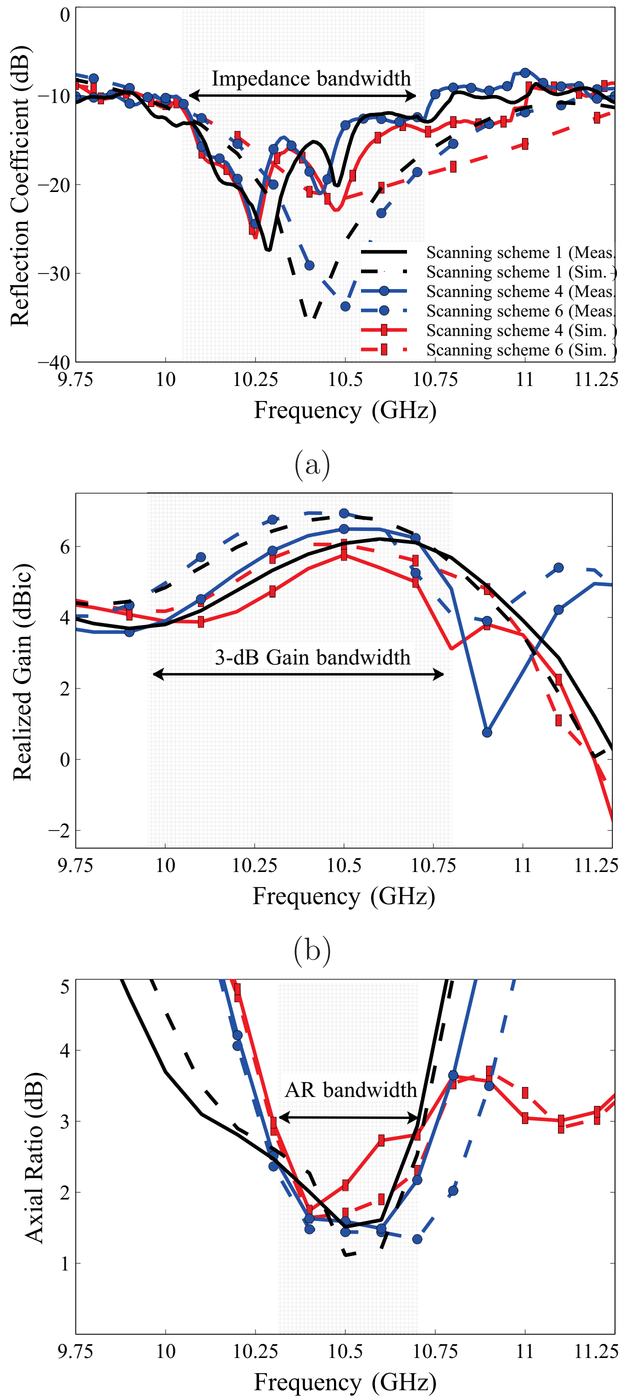

Figure 61: Simulated and measured gain pattern, axial ratio and reflection coefficient versus frequency for selected scanning schemes in Table I. (a) Reflection coefficient. (b) Gain pattern. (c) Axial ratio.

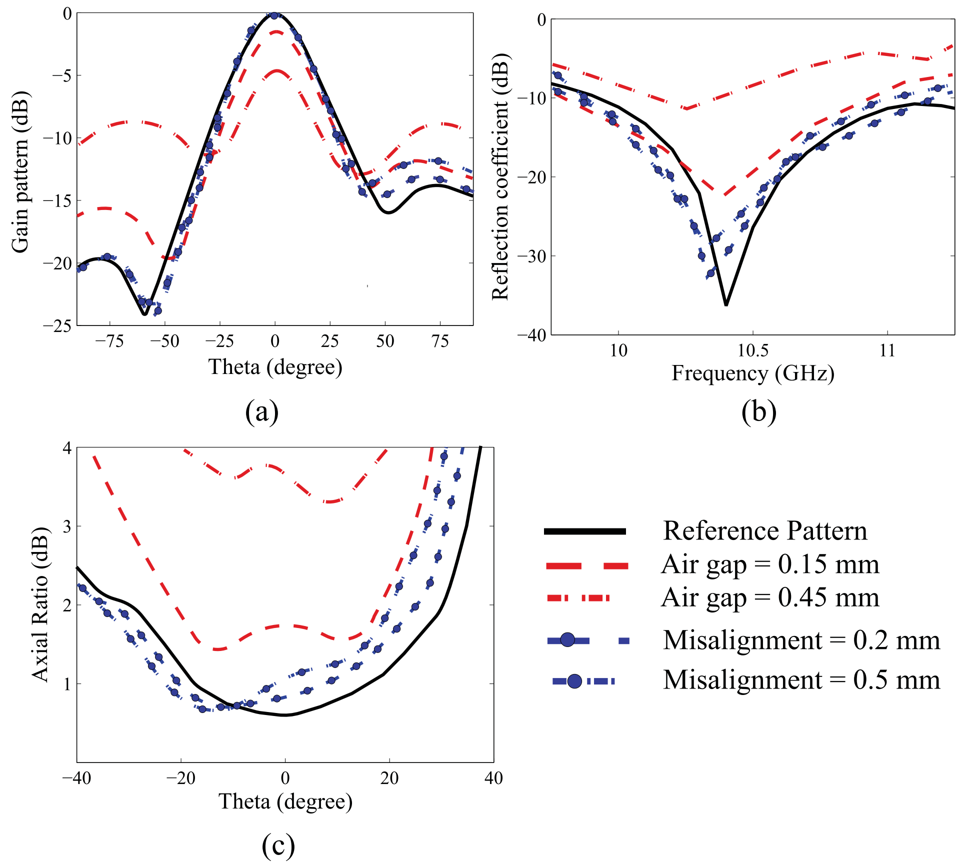

Figure 62: Simulated parametric studies of the fabrication practicalities effect on the antenna radiation characteristics. (a) Normalized radiation pattern. (b) Reflection coefficient. (c) Axial ratio.

air gaps between the radiating and feeding layers. It is evident that increasing the air gap can considerably reduce the antenna gain and increase the sidelobe levels. Furthermore, increasing the air gap up to about 0.5 mm can deteriorate the radiation pattern.

The effect of the misalignments of the radiating layer and feeding layer on the radiation pattern is also shown in Fig. 62(a). Note that the misalignments in this figure are in the directions of both x and y-axis. It can be observed that increasing the misalignment up to 0.8 mm can tilt the maximum beam direction, and increase the sidelobe levels. Fig. 62(b) shows the input impedance matching of the antenna. It is noticed that the mentioned practical errors can shift the resonant frequency and reduce the impedance matching level. The axial ratio performance of the antenna is depicted in Fig. 62(c). Again, it is seen that as the air gap and misalignment increase, the performance deteriorates. It is noted that to reduce these undesired effects, we have used the same locations on the top and the bottom layer, connecting them with plastic screws and plastic holders (shown in Fig. 62(c)) to tighten up the radiated layer with the feeding layer. It is worth noting that the fabrication tolerance, possible misalignment during measurements, and the possible inaccuracy of the varactor equivalent circuit model at higher frequencies can also be the other sources of discrepancies between the simulation and measurement results.

6.6 Conclusion

A new CP-ESPAR of dielectric resonator antennas was presented in this chapter, The CP beam steering was achieved by adopting a sequential rotation approach for placing the parasitic antennas that are loaded with tunable varactors. A control board composed of an array of digital to analog converters and a microcontroller is placed behind the antenna. This board is connected to the feed stubs of each parasitic radiators by a DC biasing network, providing the appropriate biasing voltage to each varactor. To facilitate the fabrication of the DRAs, a perforation technique was used, which eliminates the need for aligning and bonding of the individual DRAs. The fabricated prototype was measured, demonstrating a 3.8% bandwidth (the overlap of 10-dB return loss, 3-dB axial ratio bandwidths, and 3-dBic gain bandwidth) within the X-band. There are some discrepancies between the measured and the simulated results due to the possible air gap between the dielectric layers, possible misalignment between the radiating elements and the ground plane, fabrication tolerance, possible misalignment during the measurements, and the possible inaccuracy of the varactor equivalent circuit model at higher frequencies. To reduce the possible airgap and misalignment between the layers, the same locations on the layers have been specified and connected with plastic screws and plastic holders to tighten up the antenna layers.

Chapter 7

Conclusion and Future Work

7.1 Conclusion

In this thesis, the potentials of the ESPAR technology for today's advanced commu- nication systems have been investigated. The thesis presents several contributions related to the design and analysis of ESPAR technology using dielectric resonator antenna (DRA) as the main radiator element. First, we highlighted some practical issues that are critical in the implementation of a large ESPAR. These crucial issues include the design of a feeding network, difficulties in aligning and bonding the individual elements of the DRA and the grating lobe problem. The design of large array is useful in many applications since some required reconfigurable radiation characteristics may not be achievable with a single ESPAR element. The designed feeding network is of parallel-series combination, which minimizes the feeding insertion loss due to the reduction of the overall length of the transmission lines. In addition, the space usage of the given aperture is significantly improved in a parallel- series-fed architecture. The perforation technique is used to fabricate an array of DRAs from a single dielectric sheet to alleviate the problems associated with aligning and bonding the individual elements of the DRA. This technique showed good agreement between the perforated DRAs and their equivalent structures. To best explore the differences and advantages of our approach, the proposed ESPAR is compared with the conventional phased array antenna and steerable reflectarray antenna (RA). The proposed large ESPAR can incredibly reduce the number of phase shifter by 80 % in comparison with the conventional phased array, which reduce the cost significantly. We also propose a prototype of the large ESPAR antenna for broadside, proving the exceptional performance of the large ESPAR.

Second, we investigated potentials of ESPAR for MIMO and massive MIMO systems. MIMO technology has attracted tremendous interest due to its capabilities in enhancing the data transmission capacity, increasing the reliability, and reducing the multipath fading. However, in this technology for feeding each individual antenna, one radio frequency chain is required that can increase the power consumption and complexity of the structure. Moreover, to obtain decorrelated channels and to reduce mutual coupling, the antenna elements should be spaced sufficiently far from each other that imposes increased physical dimensions. In contrast to the conventional MIMO structures, in ESPAR only one RF chain is needed and the small size constraint turns to be an advantage as the mutual coupling is exploited to form the desired signals. Furthermore, by controlling the tunable loads at each parasitic antenna element, different radiation patterns can be formed which can significantly improve the performance of a MIMO antenna system operating in a changing environment. Thus, by using the advantages of ESPAR, a design approach to address the size and cost issues is proposed through this work. A 4-port MIMO configuration is proposed which the mutual coupling of its adjacent ports are reduced by orthogonal placement of subarrays. This structure is well examined in terms of the MIMO figure of merits such as isolation, correlation, mean effective gain and branch power ratio. We also studied the performance of the proposed DR-ESPAR in a massive MIMO configuration by studying the isolation between ports and the multiple beams capability. Finally, a prototype of the 4-port MIMO structure was designed, fabricated, and measured. It is observed that the proposed antenna satisfies the criteria of low correlation ($\rho_e < 0.5$) with comparable average received power |MEGi − MEGj| less than 3 dB at its operating frequency band. These results have demonstrated that the proposed ESPAR design can be successfully implemented for MIMO and massive MIMO structures.

Finally, an effective method to design an ESPAR with a circularly polarized (CP) beam-scanning feature has been proposed. Circular polarization is an ideal polarization due to its advantages in signal propagation properties, which can address the difficulties associated with mobility, inclement weather conditions, and immunity to multi path distortion. In this work, a new CP-ESPAR of dielectric resonator antennas was presented. The CP beam steering was achieved by adopting a sequential rotation approach for placing the parasitic antennas that are loaded with tunable varactors. A control board composed of an array of digital to analog converters and a microcontroller is placed behind the antenna. This board is connected to the feed stubs of each parasitic radiator by a DC biasing network, providing the appropriate biasing voltage to each varactor. To facilitate the fabrication of the DRAs, a perforation technique was used, which eliminates the need for aligning and bonding of the individual DRAs. The fabricated prototype was measured, demonstrating a 3.8% bandwidth (the overlap of 10-dB return loss, 3-dB axial ratio bandwidths, and 3-dBic gain bandwidth) within the X-band. The proposed CP-ESPAR technique eliminates the need for expensive phase shifters, which significantly reduces cost and fabrication complexity.

7.2 Suggestions for Future Work

There are a number of interesting topics related to ESPAR technology that can be subjects of further research. In particular, some of the recommendations for future work are as follows.

1) In ESPAR, the coupled radiation to the parasitic elements has a frequency dependent phase delay which can lead to a beam squint effect and a limited bandwidth. The dispersive phase delay has a negative slope with frequency that can cancel with an element that has

an equivalent positive phase dispersion slope such as non-Foster parasitic loads. Further, by tuning the non-Foster load, we can tune the total scattered phase to achieve steerable patterns. A detailed study on this technique could be useful in developing an electronically tunable, broadband, low cost parasitic array.

2) The design of ESPAR in the millimeter-wave band has not been done in the literature due to the problems related to the varactor availability and size constraints for the DC biasing lines. However, the fast pace of technology paves the way of millimeter-wave frequency band should be investigated such as cavity backed slot antenna that simultaneously provide excellent aperture efficiency and a high coupling level. Different feeding method can also be studied such as ridge gap or substrate integrated wave technologies.

3) In ESPAR the mutual coupling is an advantage and the methods that can increase this effect is desired. Higher coupling can be obtained by introducing parasitic slots or transmission lines that can couple more energy from the driven elements to the parasitic loads.

Bibliography

[1] J. S. Herd and M. D. Conway, “The evolution to modern phased array architectures,” *Proceedings of the IEEE*, vol. 104, no. 3, pp. 519–529, March 2016.

[2] S. Zhang, G. Huff, J. Feng, and J. Bernhard, “A pattern reconfigurable microstrip parasitic array,” *IEEE Transactions on Antennas and Propagation*, vol. 52, no. 10, pp. 2773–2776, 2004.

[3] S. Uda, “Wireless beam of short electric waves,” *J. IEE*, pp. 273–282, 1926.

[4] M. Gueguen, “Electronically step-by-step rotated directive radiation beam antenna,” Nov. 5 1974, uS Patent 3,846,799.

[5] R. Milne, “Adaptive array antenna,” Oct. 13 1987, uS Patent 4,700,197.

[6] D. Gray, J. W. Lu, and D. V. Thiel, “Electronically steerable yagi-uda microstrip patch antenna array,” *IEEE Transactions on antennas and propagation*, vol. 46, no. 5, pp. 605–608, 1998.

[7] D. V. Thiel, S. O’Keefe, and J. W. Lu, “Electronic beam steering in wire and patch antenna systems using switched parasitic elements,” in *Antennas and Propagation Society International Symposium, 1996. AP-S. Digest*, vol. 1. IEEE, 1996, pp. 534–537.

[8] A. Sibille, C. Roblin, and G. Poncelet, "Circular switched monopole arrays for beam steering wireless communications," *Electronics letters*, vol. 33, no. 7, pp. 551–552, 1997.

[9] S. Preston, D. Thiel, J. W. Lu, S. O'keefe, and T. Bird, "Electronic beam steering using switched parasitic patch elements," *Electronics Letters*, vol. 33, no. 1, pp. 7–8, 1997.

[10] S. Preston, D. Thiel, and J. Lu, "A multibeam antenna using switched parasitic and switched active elements for space-division multiple access applications," *IEICE transactions on electronics*, vol. 82, no. 7, pp. 1202–1210, 1999.

[11] R. Vaughan, "Switched parasitic elements for antenna diversity," *IEEE Transactions on Antennas and Propagation*, vol. 47, no. 2, pp. 399–405, 1999.

[12] R. Harrington, "Reactively controlled directive arrays," *IEEE Trans. Antennas Propag.*, vol. 26, no. 3, pp. 390–395, May. 1978.

[13] Y. Yusuf and X. Gong, "A low-cost patch antenna phased array with analog beam steering using mutual coupling and reactive loading," *IEEE Antennas and Wireless Propagation Letters*, vol. 7, pp. 81–84, 2008.

[14] K. Gyoda and T. Ohira, "Design of electronically steerable passive array radiator (es-par) antennas," *Antennas and Propagation Society International Symposium, 2000. IEEE*, vol. 2, pp. 922–925, 2000.

[15] J. Lu, D. Ireland, and R. Schlub, "Dielectric embedded espar (de-espar) antenna array for wireless communications," *IEEE transactions on antennas and propagation*, vol. 53, no. 8, pp. 2437–2443, 2005.

[16] J. J. Luther, S. Ebadi, and X. Gong, "A microstrip patch electronically steerable parasitic array radiator (ESPAR) antenna with reactance-tuned coupling and maintained resonance," *IEEE Transactions on Antennas and Propagation*, vol. 60, no. 4, pp. 1803–1813, April 2012.

[17] S. Jeong, D. Ha, and W. J. Chappell, "A planar parasitic array antenna for tunable radiation pattern," in *2009 IEEE Antennas and Propagation Society International Symposium*, June 2009, pp. 1–4.

[18] J. J. Luther, S. Ebadi, and X. Gong, "A low-cost 2 × 2 planar array of three-element microstrip electrically steerable parasitic array radiator (espar) subcells," *IEEE Transactions on Microwave Theory and Techniques*, vol. 62, no. 10, pp. 2325–2336, Oct 2014.

[19] M. R. Nikkhah, J. Rashed-Mohassel, and A. A. Kishk, "Compact low-cost phased array of dielectric resonator antenna using parasitic elements and capacitor loading," *IEEE Trans. Antennas Propag.*, vol. 61, no. 4, pp. 2318–2321, Apr. 2013.

[20] M. R. Nikkhah, P. Loghmannia, J. Rashed-Mohassel, and A. A. Kishk, "Theory of ESPAR design with their implementation in large arrays," *IEEE Trans. Antennas Propag.*, vol. 62, no. 6, pp. 3359–3364, Jun. 2014.

[21] A. Petosa, "Circular and dual-polarized DRA," in *Dielectric resonator antenna handbook*, Atlanta, GA: Artech House, 2006, ch. 7, pp. 178–192.

[22] L. N. Pringle, P. H. Harms, S. P. Blalock, G. N. Kiesel, E. J. Kuster, P. G. Friederich, R. J. Prado, J. M. Morris, and G. S. Smith, "A reconfigurable aperture antenna based on switched links between electrically small metallic patches," *IEEE Transactions on Antennas and Propagation*, vol. 52, no. 6, pp. 1434–1445, 2004.

[23] X. Yuan, Z. Li, D. Rodrigo, H. S. Mopidevi, O. Kaynar, L. Jofre, and B. A. Cetiner, "A parasitic layer-based reconfigurable antenna design by multi-objective optimization," *IEEE Transactions on Antennas and Propagation*, vol. 60, no. 6, pp. 2690–2701, 2012.

[24] Z. Li, E. Ahmed, A. M. Eltawil, and B. A. Cetiner, "A beam-steering reconfigurable antenna for wlan applications," *IEEE Transactions on Antennas and Propagation*, vol. 63, no. 1, pp. 24–32, 2015.

[25] Z. Li, D. Rodrigo, L. Jofre, and B. A. Cetiner, "A new class of antenna array with a reconfigurable element factor," *IEEE transactions on antennas and propagation*, vol. 61, no. 4, pp. 1947–1955, 2013.

[26] D. Rodrigo, B. A. Cetiner *et al.*, "Frequency, radiation pattern and polarization reconfigurable antenna using a parasitic pixel layer," *IEEE transactions on antennas and propagation*, vol. 62, no. 6, pp. 3422–3427, 2014.

[27] S. Song and R. D. Murch, "An efficient approach for optimizing frequency reconfigurable pixel antennas using genetic algorithms," *IEEE Transactions on Antennas and Propagation*, vol. 62, no. 2, pp. 609–620, 2014.

[28] P. Lotfi, S. Soltani, and R. D. Murch, "Broadside beam-steerable planar parasitic pixel patch antenna," *IEEE Transactions on Antennas and Propagation*, vol. 64, no. 10, pp. 4519–4524, 2016.

[29] A. G. Besoli and F. De Flaviis, "A multifunctional reconfigurable pixeled antenna using mems technology on printed circuit board," *IEEE Transactions on Antennas and Propagation*, vol. 59, no. 12, pp. 4413–4424, 2011.

[30] D. Rodrigo and L. Jofre, "Frequency and radiation pattern reconfigurability of a multi-size pixel antenna," *IEEE transactions on antennas and propagation*, vol. 60, no. 5, pp. 2219–2225, 2012.

[31] P. Lotfi, S. Soltani, and R. D. Murch, "Printed endfire beam-steerable pixel antenna," *IEEE Transactions on Antennas and Propagation*, vol. 65, no. 8, pp. 3913–3923, 2017.

[32] D. Rodrigo, Y. Damgaci, M. Unlu, B. A. Cetiner, J. Romeu, and L. Jofre, "Antenna reconfigurability based on a novel parasitic pixel layer," in *Antennas and Propagation (EUCAP), Proceedings of the 5th European Conference on.* IEEE, 2011, pp. 3497–3500.

[33] J. G. Maloney, M. P. Kesler, P. H. Harms, and G. S. Smith, "Fragmented aperture antennas and broadband antenna ground planes," Nov. 27 2001, uS Patent 6,323,809.

[34] J. C. Maloney, M. P. Kesler, L. M. Lust, L. N. Pringle, T. L. Fountain, P. H. Harms, and G. S. Smith, "Switched fragmented aperture antennas," in *Antennas and Propagation Society International Symposium, 2000. IEEE*, vol. 1. IEEE, 2000, pp. 310–313.

[35] L. Pringle, P. Friederich, L. Fountain, P. Harms, D. Denison, E. Kuster, S. Blalock, R. Prado, G. Kiesel, G. Smith *et al.*, "Architecture and performance of a reconfigurable aperture," in *Antennas Appl. Symposium*, 2001.

[36] L. N. Pringle, P. G. Friederich, S. P. Blalock, G. N. Kiesel, P. H. Harms, D. R. Denison, E. J. Kuster, T. Fountain, and G. S. Smith, "Gtri reconfigurable aperture design," in *Antennas and Propagation Society International Symposium, 2002. IEEE*, vol. 1. IEEE, 2002, pp. 473–476.

[37] C. A. Balanis, "Antenna theory: A review," *Proceedings of the IEEE*, vol. 80, no. 1, pp. 7–23, 1992.

[38] W. L. Stutzman and G. A. Thiele, *Antenna theory and design.* John Wiley & Sons, 2012.

[39] R. W. Schlub, “Practical realization of switched and adaptive parasitic monopole radiating structures,” Ph.D. dissertation, Griffith University, 2004.

[40] J. Mautz and R. Harrington, “Modal analysis of loaded n-port scatterers,” *IEEE Transactions on Antennas and Propagation*, vol. 21, no. 2, pp. 188–199, 1973.

[41] R. Richtmyer, “Dielectric resonators,” *Journal of Applied Physics*, vol. 10, no. 6, pp. 391–398, 1939.

[42] S. Long, M. McAllister, and L. Shen, “The resonant cylindrical dielectric cavity antenna,” *IEEE Transactions on Antennas and Propagation*, vol. 31, no. 3, pp. 406–412, 1983.

[43] M. McAllister, S. A. Long, and G. Conway, “Rectangular dielectric resonator antenna,” *Electronics Letters*, vol. 19, no. 6, pp. 218–219, 1983.

[44] M. McAllister and S. A. Long, “Resonant hemispherical dielectric antenna,” *Electronics Letters*, vol. 20, no. 16, pp. 657–659, 1984.

[45] R. K. Mongia and A. Ittipiboon, “Theoretical and experimental investigations on rectangular dielectric resonator antennas,” *IEEE Trans. Antennas Propag.*, vol. 45, no. 9, pp. 1348–1356, 1997.

[46] B.-T. Lim, “Dielectric resonator antennas: theory and design,” Ph.D. dissertation, Massachusetts Institute of Technology, 1999.

[47] A. Petosa, A. Ittipiboon, and S. Thirakoune, “Perforated dielectric resonator antennas,” *Electronics Letters*, vol. 38, no. 24, pp. 1493–1495, 2002.

[48] K. Luk and K. Leung, *Dielectric Resonator Antennas*, ser. Antennas S. Research Studies Press, 2003. [Online]. Available: https://books.google.ca/books?id=_nhbkgEACAAJ

[49] J. Huang, "A parallel-series-fed microstrip array with high efficiency and low cross-polarization," *Microwave and Optical Technology Letters*, vol. 5, no. 5, pp. 230–233, 1992.

[50] G. P. Junker, A. A. Kishk, D. Kejfez, A. W. Glisson, and J. Guo, "Input impedance of microstrip-slot-coupled dielectric resonator antennas mounted on thin dielectric layers," *International Journal of RF and Microwave Computer-Aided Engineering*, vol. 6, no. 3, pp. 174–182, 1996.

[51] J. B. Muldavin and G. M. Rebeiz, "Millimeter-wave tapered-slot antennas on synthesized low permittivity substrates," *IEEE Transactions on Antennas and Propagation*, vol. 47, no. 8, pp. 1276–1280, Aug 1999.

[52] M. R. Islam and M. Ali, "Elevation plane beam scanning of a novel parasitic array radiator antenna for 1900 mhz mobile handheld terminals," *IEEE Transactions on Antennas and Propagation*, vol. 58, no. 10, pp. 3344–3352, 2010.

[53] G. B. Gentili, M. Morini, and S. Selleri, "Array factor considerations for dielectric resonator antennas arrays," in *Antennas and Propagation Society International Symposium, 2000. IEEE*, vol. 3. IEEE, 2000, pp. 1318–1321.

[54] T. D. Dimousios, S. A. Mitilineos, S. C. Panagiotou, and C. N. Capsalis, "Design of a corner-reflector reactively controlled antenna for maximum directivity and multiple beam forming at 2.4 ghz," *IEEE Transactions on Antennas and Propagation*, vol. 59, no. 4, pp. 1132–1139, 2011.

[55] V. Srinivasan and V. Fusco, "Circularly polarised mechanically steerable reflectarray," *IEE Proceedings-Microwaves, Antennas and Propagation*, vol. 152, no. 6, pp. 511–514, 2005.

[56] E. Carrasco, M. Barba, and J. A. Encinar, "X-band reflectarray antenna with switching-beam using pin diodes and gathered elements," *IEEE Transactions on Antennas and Propagation*, vol. 60, no. 12, pp. 5700–5708, 2012.

[57] M. Riel and J.-J. Laurin, "Design of an electronically beam scanning reflectarray using aperture-coupled elements," *IEEE Transactions on Antennas and Propagation*, vol. 55, no. 5, pp. 1260–1266, 2007.

[58] O. Bayraktar, O. A. Civi, and T. Akin, "Beam switching reflectarray monolithically integrated with rf mems switches," *IEEE Transactions on Antennas and Propagation*, vol. 60, no. 2, pp. 854–862, 2012.

[59] S. V. Hum and J. Perruisseau-Carrier, "Reconfigurable reflectarrays and array lenses for dynamic antenna beam control: A review," *IEEE Transactions on Antennas and Propagation*, vol. 62, no. 1, pp. 183–198, 2014.

[60] M. Chaharmir, J. Shaker, and H. Legay, "Broadband design of a single layer large reflectarray using multi cross loop elements," *IEEE Transactions on Antennas and Propagation*, vol. 57, no. 10, pp. 3363–3366, 2009.

[61] M. M. Jacob, J. Long, and D. F. Sievenpiper, "Non-foster loaded parasitic array for broadband steerable patterns," *IEEE Transactions on Antennas and Propagation*, vol. 62, no. 12, pp. 6081–6090, 2014.

[62] F. Venneri, S. Costanzo, and G. D. Massa, "Design and validation of a reconfigurable single varactor-tuned reflectarray," *IEEE Transactions on Antennas and Propagation*, vol. 61, no. 2, pp. 635–645, Feb 2013.

[63] H. H. Yang and T. Q. Quek, *Massive MIMO Meets Small Cell: Backhaul and Cooperation*. Springer, 2016.

[64] E. G. Larsson, O. Edfors, F. Tufvesson, and T. L. Marzetta, "Massive mimo for next generation wireless systems," *IEEE Communications Magazine*, vol. 52, no. 2, pp. 186–195, 2014.

[65] J. Malik, A. Patnaik, and M. Kartikeyan, "Compact antennas for high data rate communication."

[66] M. A. Chernyavskiy, "Compact multifunctional dipole antenna array for mimo systems," 2012.

[67] Y. Zhou, "Performance evaluation of pattern reconfigurable antennas in mimo systems," Ph.D. dissertation, University of Toronto (Canada), 2012.

[68] E. Björnson, J. Hoydis, L. Sanguinetti *et al.*, "Massive mimo networks: Spectral, energy, and hardware efficiency," *Foundations and Trends® in Signal Processing*, vol. 11, no. 3-4, pp. 154–655, 2017.

[69] C. E. Shannon, "A mathematical theory of communication," *ACM SIGMOBILE Mobile Computing and Communications Review*, vol. 5, no. 1, pp. 3–55, 2001.

[70] M. Manteghi and Y. Rahmat-Samii, "Multiport characteristics of a wide-band cavity backed annular patch antenna for multipolarization operations," *IEEE Transactions on Antennas and Propagation*, vol. 53, no. 1, pp. 466–474, 2005.

[71] S. ho Chae, W. il Kawk, S.-O. Park, and K. Lee, "Analysis of mutual coupling in mimo antenna array by tarc calculation," *Microwave Conference, 2006. APMC 2006. Asia-Pacific*, pp. 2090–2093, 2006.

[72] M. S. Sharawi, *Printed MIMO antenna engineering.* Artech House, 2014.

[73] ——, "Printed multi-band mimo antenna systems and their performance metrics [wireless corner]," *IEEE Antennas and Propagation Magazine*, vol. 55, no. 5, pp. 218–232, 2013.

[74] P. Pathak and N. Wang, “Ray analysis of mutual coupling between antennas on a convex surface,” *IEEE transactions on antennas and propagation*, vol. 29, no. 6, pp. 911–922, 1981.

[75] S. Blanch, J. Romeu, and I. Corbella, “Exact representation of antenna system diversity performance from input parameter description,” *Electronics letters*, vol. 39, no. 9, pp. 705–707, 2003.

[76] M. S. Sharawi, M. A. Jan, and D. N. Aloi, “Four-shaped 2 3 2 multi-standard compact multiple-input-multiple-output antenna system for long-term evolution mobile handsets,” *IET Microwaves, Antennas Propagation*, vol. 6, no. 6, pp. 685–696, April 2012.

[77] T. Taga, “Analysis for mean effective gain of mobile antennas in land mobile radio environments,” *IEEE Transactions on Vehicular Technology*, vol. 39, no. 2, pp. 117–131, 1990.

[78] A. Ando, T. Taga, A. Kondo, K. Kagoshima, and S. Kubota, “Mean effective gain of mobile antennas in line-of-sight street microcells with low base station antennas,” *IEEE Transactions on Antennas and Propagation*, vol. 56, no. 11, pp. 3552–3565, 2008.

[79] T. Svantesson, “An antenna solution for mimo channels: The multimode antenna,” in *Signals, Systems and Computers, 2000. Conference Record of the Thirty-Fourth Asilomar Conference on*, vol. 2. IEEE, 2000, pp. 1617–1621.

[80] S. Zhang, Z. Ying, J. Xiong, and S. He, “Ultrawideband mimo/diversity antennas with a tree-like structure to enhance wideband isolation,” *IEEE Antennas and Wireless Propagation Letters*, vol. 8, pp. 1279–1282, 2009.

[81] J.-F. Li, Q.-X. Chu, Z.-H. Li, and X.-X. Xia, “Compact dual band-notched uwb mimo antenna with high isolation,” *IEEE transactions on antennas and propagation*, vol. 61, no. 9, pp. 4759–4766, 2013.

[82] X.-L. Liu, Z.-D. Wang, Y.-Z. Yin, J. Ren, and J.-J. Wu, “A compact ultrawide-band mimo antenna using qsca for high isolation,” *IEEE Antennas and Wireless Propagation Letters*, vol. 13, pp. 1497–1500, 2014.

[83] M. Koohestani, A. A. Moreira, and A. K. Skrivervik, “A novel compact cpw-fed polarization diversity ultrawideband antenna,” *IEEE Antennas and Wireless Propagation Letters*, vol. 13, pp. 563–566, 2014.

[84] C.-X. Mao and Q.-X. Chu, “Compact coradiator uwb-mimo antenna with dual polarization,” *IEEE transactions on antennas and propagation*, vol. 62, no. 9, pp. 4474–4480, 2014.

[85] Y. Li, Z. Zhang, W. Chen, Z. Feng, and M. F. Iskander, “A dual-polarization slot antenna using a compact cpw feeding structure,” *IEEE Antennas and Wireless Propagation Letters*, vol. 9, pp. 191–194, 2010.

[86] D. Manteuffel and R. Martens, “Compact multimode multielement antenna for indoor uwb massive mimo,” *IEEE Transactions on Antennas and Propagation*, vol. 64, no. 7, pp. 2689–2697, 2016.

[87] Y. Gao, R. Ma, Y. Wang, Q. Zhang, and C. Parini, “Stacked patch antenna with dual-polarization and low mutual coupling for massive mimo,” *IEEE Transactions on Antennas and Propagation*, vol. 64, no. 10, pp. 4544–4549, 2016.

[88] S. Sanayei and A. Nosratinia, “Antenna selection in mimo systems,” *IEEE Communications Magazine*, vol. 42, no. 10, pp. 68–73, 2004.

[89] I. Santamaria, V. Elvira, J. Vía, D. Ramirez, J. Pérez, J. Ibanez, R. Eickoff, and F. Ellinger, “Optimal mimo transmission schemes with adaptive antenna combining

in the rf path," in *Signal Processing Conference, 2008 16th European.* IEEE, 2008, pp. 1–5.

[90] M. Lari, S. A. Bassam, A. Mohammadi, and F. M. Ghannouchi, "Time-multiplexed single front-end multiple-input multiple-output receivers with preserved diversity gain," *IET communications*, vol. 5, no. 6, pp. 789–796, 2011.

[91] F. Tzeng, A. Jahanian, D. Pi, and P. Heydari, "A cmos code-modulated path-sharing multi-antenna receiver front-end," *IEEE Journal of Solid-State Circuits*, vol. 44, no. 5, pp. 1321–1335, 2009.

[92] A. Jahanian, F. Tzeng, and P. Heydari, "Code-modulated path-sharing multi-antenna receivers: theory and analysis," *IEEE Transactions on Wireless Communications*, vol. 8, no. 5, 2009.

[93] O. N. Alrabadi, J. Perruisseau-Carrier, and A. Kalis, "Mimo transmission using a single rf source: Theory and antenna design," *IEEE Transactions on Antennas and Propagation*, vol. 60, no. 2, pp. 654–664, Feb 2012.

[94] A. Kalis, A. G. Kanatas, and C. B. Papadias, *Parasitic Antenna Arrays for Wireless MIMO Systems.* Springer, 2016.

[95] ——, "A novel approach to mimo transmission using a single rf front end," *IEEE Journal on Selected Areas in Communications*, vol. 26, no. 6, pp. 972–980, August 2008.

[96] A. Li, C. Masouros, and C. B. Papadias, "Mimo transmission for single-fed espar with quantized loads," *IEEE Transactions on Communications*, vol. 65, no. 7, pp. 2863–2876, 2017.

[97] A. A. Kishk, "Dielectric resonator antenna, a candidate for radar applications," *IEEE Proc. Radar Conference*, pp. 258–264, 2003.

[98] R. Movahedinia, M. R. Chaharmir, A. R. Sebak, M. R. Nikkhah, and A. A. Kishk, "Realization of large dielectric resonator antenna espar," *IEEE Trans. Antennas Propag.*, vol. 65, no. 7, pp. 3744–3749, July 2017.

[99] S. H. Zainud-Deen, S. M. Gaber, A. M. Abd-Elhady, K. H. Awadalla, and A. A. Kishk, "Wideband perforated rectangular dielectric resonator antenna reflectarray," *Proc. IEEE Antennas Propaga. Soc. Int. Symp.*, pp. 113–116, July 2011.

[100] S. ho Chae, W. il Kawk, S.-O. Park, and K. Lee, "Analysis of mutual coupling in mimo antenna array by tarc calculation," in *Microwave Conference, 2006. APMC 2006. Asia-Pacific.* IEEE, 2006, pp. 2090–2093.

[101] D. W. Browne, M. Manteghi, M. P. Fitz, and Y. Rahmat-Samii, "Experiments with compact antenna arrays for mimo radio communications," *IEEE Transactions on Antennas and Propagation*, vol. 54, no. 11, pp. 3239–3250, 2006.

[102] C. C. Chiau, "Study of the diversity antenna array for the mimo wireless communication systems," Ph.D. dissertation, University of London, 2006.

[103] R. G. Vaughan and J. B. Andersen, "Antenna diversity in mobile communications," *IEEE Transactions on vehicular technology*, vol. 36, no. 4, pp. 149–172, 1987.

[104] A. Ando, T. Taga, A. Kondo, K. Kagoshima, and S. Kubota, "Mean effective gain of mobile antennas in line-of-sight street microcells with low base station antennas," *IEEE Transactions on Antennas and Propagation*, vol. 56, no. 11, pp. 3552–3565, 2008.

[105] M. V. Komandla, G. Mishra, and S. K. Sharma, "Investigations on dual slant polarized cavity-backed massive mimo antenna panel with beamforming," *IEEE Transactions on Antennas and Propagation*, vol. 65, no. 12, pp. 6794–6799, 2017.

[106] Y. Q. Wen, B. Z. Wang, and X. Ding, "Wide-beam circularly polarized microstrip magnetic-electric dipole antenna for wide-angle scanning phased array," *IEEE Antennas Wireless Propag. Lett.*, vol. 16, pp. 428–431, 2017.

[107] X. S. Yang, B. Z. Wang, S. H. Yeung, Q. Xue, and K. F. Man, "Circularly polarized reconfigurable crossed-yagi patch antenna," *IEEE Antennas Propag. Mag.*, vol. 53, no. 5, pp. 65–80, Oct. 2011.

[108] A. Khidre, F. Yang, and A. Z. Elsherbeni, "Circularly polarized beam-scanning microstrip antenna using a reconfigurable parasitic patch of tunable electrical size," *IEEE Trans. Antennas Propag.*, vol. 63, no. 7, pp. 2858–2866, Jul. 2015.

[109] P. Hall, "Application of sequential feeding to wide bandwidth, circularly polarised microstrip patch arrays," *IEE Proc. H Microw. Antennas Propag.*, vol. 136, no. 5, pp. 390–398, 1989.

[110] R. F. Harrington, "Time-harmonic electromagnetic fields," 1961.

[111] M. Haneishi and H. Takazawa, "Broadband circularly polarised planar array composed of a pair of dielectric resonator antennas," *Electronics Letters*, vol. 21, no. 10, pp. 437–438, 1985.

[112] M. Oliver, R. Mongia, and Y. Antar, "A new broadband circularly polarized dielectric resonator antenna," in *Antennas and Propagation Society International Symposium, 1995. AP-S. Digest*, vol. 1. IEEE, 1995, pp. 738–741.

[113] A. Ittipiboon, D. Roscoe, R. Mongia, and M. Cuhaci, "A circularly polarized dielectric guide antenna with a single slot feed," in *Antenna Technology and Applied Electromagnetics [ANTEM 1994] Symposium on.* IEEE, 1994, pp. 427–430.

[114] C.-Y. Huang, J.-Y. Wu, and K.-L. Wong, "Cross-slot-coupled microstrip antenna and dielectric resonator antenna for circular polarization," *IEEE Trans. Antennas Propag.*, vol. 47, no. 4, pp. 605–609, Apr. 1999.

[115] A. A. Kishk, “Application of rotated sequential feeding for circular polarization bandwidth enhancement of planar arrays with single-fed dra elements,” in *IEEE Antennas and Propagation Society International Symposium. Digest. Held in conjunction with: USNC/CNC/URSI North American Radio Sci. Meeting (Cat. No.03CH37450)*, vol. 4, June 2003, pp. 664–667 vol.4.

[116] J. Huang, “A technique for an array to generate circular polarization with linearly polarized elements,” *IEEE Transactions on Antennas and Propagation*, vol. 34, no. 9, pp. 1113–1124, Sep 1986.

[117] ANSYS, High Frequency Structure Simulation (HFSS), Ansoft Corp., Pittsburgh, PA, 2015.

[118] A. A. Kishk, “Performance of planar four-element array of single-fed circularly polarized dielectric resonator antenna,” *Microw. Opt. Technol. Lett.*, vol. 38, no. 5, pp. 381–384, 2003.

[119] D. L. Sengupta, J. E. Ferris, R. Larson, and T. Smith, “Azimuth and elevation direction finder study,” Uni. Mich. Radiation Lab., Ann Arbor, Tech. Rep., 7577-1-Q-RL-2159, Dec. 1965.

Appendix A

DR suppliers

In this appendix, some DR suppliers, along with the materials and dielectric constants of their DRs are shown [21]. This is useful to study the DRA datasheets before the design of a DRA since there are some limitations in terms of ϵ_r and size of DRs.

Table 9: Some DR suppliers, along with the materials and dielectric constants of their DRs (Luk et al. [48], ©Research Studies Press Ltd.).

Company	**Material**	**Dielectric Constant**
Countis Laboratories	CD-Series (solid state solutions of magnesium, calcium, silicon, and titanium oxides)	6.3 – 140.0
Emerson & Cuming (Materials not specified)	Eccostock	3 – 30
Hiltek Microwave Ltd.	Magnesium Manganese Aluminum Iron Ferrite	9.2 (+/- 0.46)
	Magnesium Titanate	16.0 (± 0.8)
	Lithium Ferrite	20.0 (± 1)
	Zirconium Tin Titanate	37.0 (± 1)
	Titania Ceramic	80 – 100
Morgan Electro Ceramics	Zr, Sn titanate	37
	Mg, Ca titanate	20
	Ba, Nd titanate	88
	Ba, Zn titanate	30
	Steatile	6
Murata (Materials not specified)	U series	36.6 – 38.9 (± 0.5)
	M series	37.7 – 39.2 (± 1)
	V series	33.5 – 35.1 (± 0.5)
	R series	29.7 – 31.5 (± 0.8)
	B series	27.9 ± 0.5
	E series	24.2 – 24.9 (± 0.4)
	F series	23.8 – 24.2 (± 0.5)
	Dielectric substrate	38 – 92 (± 1)
Pacific Ceramics, Inc. (Materials not specified)	PD-Series	6.5 – 270
Temex Components & Temex Telecom	(Zr, Sn, Ti) O_4	37.3 – 37.7
	Ba, Zn, Ta, O	29.5 – 32
	Ba, Sm, Ti	78 ± 0.5
Trans-Tech	Zirconium titanate based	44.7 – 46.2
	Ba, Zn, Ta-oxide	29.0 – 30.7
	Barium titanate	35.0 – 36.5
	Ba, Zn, Ta-oxide (perovskite)	29.5 – 31.0